

AN ABSTRACT OF THE DISSERTATION OF:

Cory G. Garms for the degree of Doctor of Philosophy in Sustainable Forest Management  
presented on June 8, 2020.

Title: Using Point Clouds for Single Tree Forest Inventory at the Beginning and End of the Rotation

Abstract approved:

---

Bogdan Strimbu

Abstract:

The portability and reduced price of unmanned aerial systems (UAS) in recent years has led to a broad range of new UAS-enabled scientific inquiries, including for forestry. Small, consumer-grade UAS are advantageous for forest measurements due to their portability, ease and safety of deployment, and notably, they are currently the only remote sensing technology capable of measuring both individual seedlings and individual mature trees from above. Light detection and ranging (lidar) sensors have been increasingly used in forestry research over the past few decades as well, and now models exist which can be integrated with UAS for tree mensuration. Computer vision software known as structure from motion (SfM) can be used to produce analogous data to those produced by lidar, known as point clouds, from still images taken from UAS. The goal of this dissertation is to examine how to use point cloud data to augment tree level estimates for forest inventory. To cover a broad range of dimensional values defining a forest, two different stages in the life cycle of the stand were investigated, the seedling stage, and the mature stage which precedes harvest. For analyzing seedlings, the first manuscript (second chapter) in this dissertation used UAS and multispectral sensors to produce point clouds of southwestern white pine

seedlings in common garden boxes. Here, a methodology is presented for estimating seedling sizes from SfM reconstructions and using them to improve the predictive power of seedling size models along with ground measurements from the previous year. Also, I make recommendations for how common garden designs can be designed so as to lengthen the duration of useful UAS surveys. Finally, I present a seedling size variable that performs well both as a predictor and as a response, the product of seedling height and diameter at root collar, or longitudinal area. To address the mature stage of the trees, the second manuscript (third chapter) compared the performance of three platforms that vary greatly in cost, ease of operation, and data processing requirements. One of the platforms was identical to the UAS used in the first manuscript, one was a lidar carried by a larger UAS (UALS), and one was a ground based mobile lidar scanner (MLS). The UAS produced SfM height estimates that were comparable to those by the UALS, though they tended to be underestimates due to smoothing of the SfM reconstruction. Both the UALS and MLS platforms produced sufficient stem returns to locate a majority of the tree stems in the scene, while none could be located from the UAS. Using data from the MLS and the UALS, I showed that using the stem near the base of the crown or the treetop to estimate lean will produce different lean estimates and contend that the MLS is the best platform for estimating the lean of the stems. In the third and final manuscript (fourth chapter), I compared two methods for estimating stem lean from the MLS data. The more conservative lean estimate, which involves using the horizontal distance between the top and bottom of the merchantable portion of the stem, was included as a predictor to improve the fit of existing nonlinear stem taper and volume equations. The results suggest that trees that lean as little as  $2^\circ$  should be modeled differently than those which are vertical. Also, substituting other diameters higher on the stems for DBH impacts the fit of the models for leaning trees differently than for vertical ones, such that leaning trees seem to have a narrower range of optimal diameter heights. As a whole, my dissertation supports the usage of UAS and MLS to improve the quality and efficiency of remotely measuring single seedlings or mature trees forest inventory, while also identifying major limitations of the technology and recommending strategies to contend with them.

©Copyright by Cory G. Garms

June 8, 2020

All Rights Reserved

Using Point Clouds for Single Tree Forest Inventory at the Beginning and End of the Rotation

by

Cory G. Garms

A DISSERTATION

submitted to

Oregon State University

in partial fulfillment of  
the requirements for the  
degree of

Doctor of Philosophy

Presented June 8, 2020

Commencement June 2021

Doctor of Philosophy dissertation of Cory G. Garms presented on June 8, 2020.

APPROVED:

---

Major Professor, representing Sustainable Forest Management

---

Head of the Department of Forest Engineering, Resources and Management

---

Dean of the Graduate School

I understand that my dissertation will become part of the permanent collection of Oregon State University libraries. My signature below authorizes release of my dissertation to any reader upon request.

---

Cory G. Garms, Author

## ACKNOWLEDGEMENTS

The path that led me to completing my doctorate started with my mother, Lori, and my Grandmother, Nancy, who insisted that I make education a priority from a young age. My father, Randy, and Grandfather, Joe, made academic research more intuitive for me because they taught me how to ask questions, listen to others, and ask for help. Over the years, there have been many individuals who encouraged me to challenge myself academically, and I owe them my thanks, including Donna Hilton, Jyotsna Sharma, Matt Spottswood, Janis Bush, Tom Dean, Richard Keim, and Shannon Kidombo. Here at Oregon State University, I have been lucky to have excellent mentorship from my graduate advisor, Bogdan Strimbu, my friend and colleague Jon Burnett, and Professor John Bailey. These three gentlemen exemplify many of the things that make the OSU College of Forestry truly a world-class institution, including the ability to push science forward and a willingness to help others in the process. Finally, to Amanda, my fiancé and the most important person in my life, thank you for being more compassionate than anyone I have known. Your support was vital to my success in completing this PhD, and you deserve to take pride in this accomplishment because, in my eyes, it belongs to both of us.

## CONTRIBUTION OF AUTHORS

The introduction and conclusion were written in their entirety by the PhD candidate, Mr. Garms. For Chapter Two, Dr. Rentería, provided domain knowledge about the target species, while Drs Waring, and Whipple contributed by creating and maintaining the common gardens and providing contextual expertise, Dr. Wing contributed remote sensing equipment, domain knowledge, and post-processing infrastructure, while Dr. Strimbu established the research direction. For Chapter Three, Mr. Simpson and Dr. Parrish assisted with field data collections and data processing, Dr. Wing contributed sensor hardware, processing resources, and remote sensing knowledge, and Dr. Strimbu, framed the research and provided the unmanned aerial vehicle. The final manuscript, Chapter Four, was authored by Mr. Garms and his graduate advisor, Dr. Strimbu, who had an administrative role in producing this dissertation and provided substantial conceptual and structural contributions throughout.

# TABLE OF CONTENTS

	<u>Page</u>
1. Introduction .....	1
2. Augmenting Size Models for <i>Pinus strobiformis</i> Seedlings Using Dimensional Estimates from Unmanned Aircraft Systems .....	6
2.1. Introduction .....	8
2.2. Methods .....	10
2.2.3. Point Cloud Processing .....	12
2.3. Results .....	22
2.4. Discussion .....	30
2.5. Conclusions .....	35
3. Assessing Lean and Positional Error of Individual Mature Douglas-Firs ( <i>P. menziesii</i> ) with Active and Passive Sensors .....	37
3.1. Introduction .....	39
3.2. Methods .....	41
3.3. Results .....	52
3.4. Discussion .....	63
3.5. Conclusions .....	70
4. Quantifying Lean for Stem Models of Mature Douglas Firs.....	73
4.1. Introduction .....	75
4.2. Methods .....	79
4.3. Results .....	89
4.4. Discussion .....	101
4.5. Conclusions .....	105
5. Conclusion.....	107
6. Bibliography.....	109

## LIST OF FIGURES

<u>Figure</u>	<u>Page</u>
Figure 2-1: Rendering of point clouds of seedlings growing in two common garden boxes created using structure from motion photogrammetry. The clouds are colored according to height value (z) from purple (low) to gold (high). Clouds on the top row are from 2017 imagery, and clouds on the bottom row are from 2018 imagery. ....	13
Figure 2-2 Point clouds of common garden boxes viewed from above showing classification of ground (orange) and non-ground (green). The clouds from 2018 (bottom) were several times less dense in terms of points/cm <sup>2</sup> than the clouds from 2017, which caused them to look less bright in the rendering. ....	15
Figure 2-3 Digital terrain models (DTM) for the two common garden boxes in the study created from UAV flights in 2017 (top) and 2018 (bottom). The scale bars show elevation above mean sea level (m). ....	15
Figure 2-4: Canopy height models (CHM) for the two common garden boxes in the study created from UAV flights in 2017 (top) and 2018 (bottom). The scale bars show height above ground (cm) .....	16
Figure 2-5: Vegetation mask vectors superimposed over NDVI from multispectral imagery of common garden boxes in 2017 (top) and 2018 (bottom). Circular plant crown vectors are shown in green. ....	17
Figure 2-6a: Variable importance plot for the dependent variable total height.....	23
Figure 2-7: Correlation matrices showing Pearson correlation coefficients (r) among height predictions from UAS ( <i>italics</i> ) and ground-based measurements ( <b>Bold</b> ) in 2017 (a.) and 2018 (b.). Cell are shaded according to the strength of significant relationships based on Pearson’s product moment correlation coefficient (p<0.001) and colored according to correlations being positive (blue) or negative (red). ....	26
Figure 2-8a: Correlation matrices showing Pearson correlation coefficients (R) among area, volume, and slenderness estimates from UAS ( <i>italics</i> ) and ground-based measurements ( <b>Bold</b> ) in 2017. Cell are shaded according to the strength of significant relationships based on Pearson’s product moment correlation coefficient (p<0.001) and colored according to correlations being positive (blue) or negative (red). ....	27
Figure 3-1: Alignment of point clouds following coregistration, where the ALS data (red) were used as the reference points to align both the MLS (a.) (green) and UAS (b.) (blue) data. The mean (standard deviation) cloud-to-cloud distances compared to the ALS data were 0.59 m (1.18m) and 0.64 m (1.04m) for UAS and MLS, respectively. ....	45
Figure 3-2: Digital terrain models from the UAS photogrammetric point cloud (UAS), the airborne lidar scanner (ALS), and the mobile lidar scanner (MLS). ....	47
Figure 3-3: Canopy height models from the UAS photogrammetric point cloud (UAS), the airborne lidar scanner (ALS), and the mobile lidar scanner (MLS). ....	48

Figure 3-4: Horizontal slices of point clouds from 1 to 2 meters (pink) and 18-19 meters (purple) above ground (purple) were created by subsampling the raw point cloud data parallel to the ground (left) and used to visually locate the stem center points (yellow) from above (right) for MLS (green) and ALS (red) platforms..... 49

Figure 3-5: Schematic showing how we used the location of each tree stem at 1m measured from the MLS platform (green) to estimate the tree lean angle ( $\theta$ ) using either the horizontal distance to the stem center at 18m ( $D_{\text{stem}}$ ) or the horizontal distance to the treetop ( $D_{\text{top}}$ ) and the estimated tree height ( $H_{\text{tree}}$ ). The tree has been trimmed and shifted slightly to the right in the image for clarity, and the lean angle is exaggerated..... 52

Figure 3-6a: Scatterplot and linear regression statistics for pairwise comparisons of tree height estimates between the three platforms we tested. Only trees which were detected by all three platforms ( $n=157$ ) were included in these models. Lines of best fit appear in red surrounded by shaded confidence interval (95%), while the line  $y=x$  appears in purple. Points are colored according to distance from the road, where blacker points are closer and orange points are farthest away..... 56

Figure 3-7: Tree lean estimates created using the locations of the stems at the base (1-2 m) as reference points and the horizontal distance to the stem location near the top (18-19m) ( $n=259$ ) (right) compared to the horizontal distance to the treetop location from the ALS data ( $n=245$ ) (center) and UAS data ( $n=246$ ) (left). The points are scaled according to the magnitude of the tree lean and colored according to the azimuth. A greyscale canopy height model (CHM) from the ALS dataset is used as the background..... 58

Figure 3-8: Distributions for tree lean angle ( $\theta$ ) estimated using stem location at 18m from the MLS ( $n=259$ ) (right), treetop locations from ALS ( $n=245$ ) (center), and treetop locations from UAS ( $n=246$ ) (left). Red dotted lines indicate the mean  $\theta$  for each platform ( $1.36^\circ$ ,  $1.55^\circ$ , and  $2.07^\circ$  for MLS, ALS, and UAS, respectively)..... 59

Figure 3-9: Distributions for tree lean azimuth for trees with lean angle  $\theta > 1^\circ$  estimated using stem locations at 18m from the MLS ( $n=259$ ) (right), treetop locations from ALS ( $n=245$ ) (center), and treetop locations from UAS ( $n=246$ ) (left). Red dotted lines indicate the mean  $\theta$  for each platform ( $177^\circ$ ,  $184^\circ$ , and  $175^\circ$  for MLS, ALS, and UAS, respectively)..... 59

Figure 3-10: Tree height estimates from UAS and ALS platforms using undecimated point clouds (blue), 10 pts/m<sup>2</sup> (purple), and 100 pts/m<sup>2</sup> (orange). Observations are sorted by mean height estimate from least to greatest. .... 60

Figure 3-11: Scatterplot showing lean magnitude (m) calculated as the horizontal displacement between the tree stem at 1m height measured from the from the MLS and the treetop locations for the same trees from the ALS (circles) and MLS (triangles) clouds at full resolution (blue), 10 pts/m<sup>2</sup> (purple), and 100 pts/m<sup>2</sup>(orange). Observations are sorted by mean distance from least to greatest. .... 61

Figure 3-12a: Scatterplots showing lean azimuth in degrees clockwise of north for tree lean estimates by using UAS to detect treetops and measuring the horizontal distance from the stem center location at 1m height measured from the MLS. Observations are sorted by the mean azimuth angle from smallest to largest. .... 62

Figure 3-13: Differences in elevation for the digital elevation model (DEM) layers created using point clouds from the three platforms we tested..... 65

Figure 3-14: Differences in height for canopy height model (CHM) layers created using point clouds from the three platforms we tested. .... 66

Figure 3-15: Confusion matrices comparing classification of trees into “leaning” and “not leaning” classes according to the lean angle based on the horizontal distance between the stem center at 1m measured from the MLS and the stem center at 18m (x-axis) versus the lean angle based on the horizontal distance between the stem center and the treetop measured from the ALS at full resolution (left), 100pts/m<sup>2</sup> (center), and 10pts/m<sup>2</sup> (right) (y-axis). We used the threshold 2 cm/m (1.15°) as the cutoff where trees having greater than 1.15° were classified as leaning..... 69

Figure 3-16: Confusion matrices comparing classification of trees into “leaning” and “not leaning” classes according to the lean angle based on the horizontal distance between the stem center at 1m measured from the MLS and the stem center at 18m (x-axis) versus the lean angle based on the horizontal distance between the stem center and the treetop measured from the UAS at full resolution (left), 100pts/m<sup>2</sup> (center), and 10pts/m<sup>2</sup> (right) (y-axis). We used the threshold 2 cm/m (1.15°) as the cutoff where trees having greater than 1.15° were classified as leaning..... 69

Figure 4-1 Location of the area of interest (AOI) within Oregon State University’s McDonald-Dunn Research Forest ..... 79

Figure 4-2: Orientation and scan angle of MLS from this study. The sensor has a vertical field of view of 27° and is tilted at 45° backwards. The beam angle ranges from 31.5° to 58.5° from vertical as it scans above and in front of the truck. .... 80

Figure 4-3 Graphic representation of the relationship between the two ways that tree lean was measured in this study. Circular vectors were fit to rasterized slices of point clouds at locations along the stems. The total lean of the tree, ( $\theta_{net}$ ) was calculated using the horizontal displacement of the stem centroid from 1 to 18 meters, while the average lean ( $\Theta$ ) was calculated as the mean of 7 sectional lean estimates ( $\theta_1$  to  $\theta_7$ ) between consecutive centroids. The values in the figure are real values from one of the sampled trees, but the lean angle of the tree is exaggerated for display..... 83

Figure 4-4: Example of two adjacent trees classified as leaning (right) or non-leaning (left) based on a 2° threshold. The rendered trees in the center of the image are shown from a profile perspective with the horizontal point cloud slices in color (1m (purple), 3m (pink), 5m (red), 7m (orange), 10m (yellow), 12m (green), 15m (cyan), and 18m (blue). Corresponding colored circular vectors from the same non-leaning (left) and leaning (right) trees from a nadir view shown on the outside of the image..... 88

Figure 4-5: Comparison of  $D_1$  estimates from MLS point cloud data collected in March 2018 versus manual DBH measurements from April 2020..... 91

Figure 4-6: Stem diameter estimates from MLS point cloud data sliced at 8 locations between 1 and 18 meters above ground. Point colors correspond with heights of point cloud slices, while polylines represent individual trees and the line type represents whether trees were calculated as leaning or non-leaning. .... 91

Figure 4-7: Scatterplot showing total tree lean ( $\Theta_{net}$ ) versus average tree lean ( $\Theta$ ) for 159 mature Douglas firs. .... 92

Figure 4-8: Correlation coefficients ( $R^2$ ) (a.) and RMSE (b.) for stem volume models of leaning and vertical trees after substituting diameters at different heights for DBH in the BR2 and POU equations. .... 101

## LIST OF TABLES

<u>Table</u>	<u>Page</u>
Table 2-1: Characteristics of the UAS used to image common garden boxes near Flagstaff, Arizona, USA in 2017 and 2018. ....	11
Table 2-2: Point cloud statistics within common garden boxes created using structure from motion photogrammetry. ....	14
Table 2-3: Descriptive statistics for ground-based measurements (bold) and remotely sensed estimates	22
Table 2-4: Linear regression models predicting 2018 seedling size (n=129). The odd numbered columns display the final models for the seedling size variables, and the even numbered columns contain only the ground-based predictors. Predictor variables measured on the ground or derived from ground-based measurements are in bold. Values in parentheses represent standard error of the coefficients above them (* p≤0.05 **p≤0.01 ***p≤0.001).....	29
Table 2-5: Confusion matrix showing predicted versus observed mortality for SWWP seedlings based on remotely sensed vegetation filtering and visual inspections on the ground. Over 90% of dead seedlings and over 98% of the total sample were correctly classified based on mortality that occurred between the observations in 2017 and 2018. ....	30
Table 3-1: Characteristics of the three UAS platforms used to create overlapping point cloud reconstructions of a small Douglas-Fir shelterwood stand in the MacDonald Forest near Corvallis, Oregon. ....	42
Table 3-2: Point cloud summary statistics for each platform following our post processing procedures.	46
Table 3-3: Tree detection accuracy using the visually detected tree centers (n=263) as the reference points and the local vertical maxima within crowns segmented using each combination of the three platforms and four segmentation algorithms that we tested. ....	53
Table 3-4: Stem detection accuracy using the visually detected tree centers (n=263) as the reference points and the tree stem locations from the aerial platforms (ALS and MLS). No stems could be located from the UAS data. ....	54
Table 3-5: Tree positional accuracy results using the stem locations (n = 273) from the MLS data as control points and the treetop coordinates within the segmented crowns using raster-based (W) and point cloud-based (L) ITDE algorithms. We found that the treetop points fell within 3 meters of the stem locations most often using the ALS data (85-89%), followed by the UAS data (81-85%), then the MLS data (69-75%). The biases ( $\mu$ ) and errors for the three platforms follow a similar pattern. Both aerial platforms had less commission error (3-8% for ALS and 1-5% for UAS) than the MLS layer (8-16%).	55
Table 4-1: Stem diameter taper and total tree volume equations used in this study. The residuals are represented by e. ....	85
Table 4-2: Modified versions of existing nonlinear stem taper and volume equations modified to include lean and distance from scanner as predictors. ....	86
Table 4-3: Summary statistics for total height (H), diameter at 1 meter ( $D_1$ ), distance to tree (T), volume with paraboloid top ( $V_p$ ), volume with conoid top ( $V_c$ ), total lean ( $\theta_{net}$ ), and average lean ( $\theta$ ) for the entire sample (n=159), as well as for trees that were considered as leaning (n=40) or non-leaning (n=119) according to the total lean angle, $\theta_{net}$ , and a 2° cutoff. ....	90

Table 4-4 Results from non-linear models predicting stem taper. Probability values ( $P(>|t|)$ ) with † had a nonsignificant ( $\alpha = 0.01$ ) parameter from the original model (i.e.,  $a_1, a_2, \dots$ ) though the model was significant overall. Cells with “—” failed to converge. .... 94

Table 4-5: Results from nonlinear models predicting total stem volume where the portion of the stem above 18 meters was approximated as a paraboloid. .... 98

Table 4-6: Results from nonlinear models predicting total stem volume, where the portion of the stem above 18 meters was approximated as a cone. Probability values ( $P(>|t|)$ ) with † had a nonsignificant ( $\alpha = 0.01$ ) parameter from the original model (i.e.,  $a_1, a_2, \dots$ ) ..... 99

Table 4-7 Nonlinear modeling results for two equations predicting total stem volume after substituting diameters at different heights ( $H_D$ ) as inputs. Probability values ( $P(>|t|)$ ) with † had a nonsignificant ( $\alpha = 0.01$ ) parameter from the original model (i.e.,  $a_1$  or  $a_2$  or  $a_3$ ), while those with †† had nonsignificant probability value for the covariate of  $\Theta_{net}$  (i.e.,  $b_1$ ), and ..... 100

# 1. Introduction

Small unmanned aircraft systems (UAS) have now become quite prevalent in the commercial sector. As the technology has grown more sophisticated, the UASs have also become more portable and less expensive. The portability and reduced price have led to a broad range of new UAS-enabled scientific inquiries, including for forestry. As forestry evolved from stand level management to individual trees – multiple services approaches, so the measurements changed. In the case of single-tree measurements, UAS can achieve greater spatial resolution than manned aircraft flights, so more precise measurements of mature trees can be attained. Because UAS can fly more frequently and at lower altitude than manned aircraft, they are less sensitive to temporal and weather constraints. Most UAS are equipped with GNSS and autopilot computers that allow for pre-programmed flight missions. Furthermore, UAS imagery can be sufficiently resolute (sub-centimeter) for detection and measurement of small individual seedlings, making the UAS the only remote sensing platform economically feasible of conducting single tree measurements of trees of all sizes. Finally, the lack of a pilot onboard the aircraft lowers the risk of serious bodily harm to the operator collecting data with UAS compared to manned aircraft.

It has been a little over a decade since small, low cost (under \$5000) UAS platforms were identified as having wide ranging potential in forestry, including fire monitoring, site inspection, and research (Grenzdörffer et al., 2008). More recently, commercial UAS have become available with lightweight sensors capable of capturing visible, near-infrared, and thermal wavelengths (Wing et al., 2014). In addition to UAS and sensor technology, the development of structure from motion (SfM) digital photogrammetry software has led to the birth of high resolution remote sensing of vegetation (Dandois and Ellis, 2010). The products of SfM photogrammetry include digital elevation models (DEM), orthophotos, and photogrammetric point clouds. The extraction of dense point cloud data from

digital images acquired with UAS dates back to 2011, though the data were not sufficiently resolute to extract single tree measurements at the time (Tao et al., 2011). Since then, all of the major components of UAS have improved dramatically, including the aircraft, sensors, onboard computers, and postprocessing software. Currently, UASs are capable of producing impressively resolute products that are of great value to natural science research, including sub-centimeter DEM outputs (Verma and Bourke, 2019), and a wide range of single-tree applications with varying degrees of success (Iglhaut et al., 2019).

Decades before UAS were used in forestry, a soviet scientist and his colleagues pioneered the use of lasers to measure individual trees. They did so by first felling a tree, then compared tape measurements with laser profile estimates (Solodukhin et al., 1976). Subsequently, the same apparatus was mounted on an airplane and trees were profiled from above (Solodukhin et al., 1977). In the 1980's other studies used similar approaches to acquire laser profiles of trees in North American forests (Aldred and Bonner, 1985; Nelson et al., 1984), including some which estimated forest measurements from the profile data (Maclean and Krabill, 1986; Maclean and Martin, 1984). It wasn't until the 1990's that modern lidar systems were created, which include a GNSS receiver and an inertial measurement unit (IMU) in conjunction with a laser rangefinder. The term inertial navigation system (INS) is used to describe the combination of IMU and an integrated computer. When INS and GNSS are used together, they enhance one another and can provide accurate estimates of the position (i.e., easting, northing, and altitude) and orientation (i.e., roll, pitch, and yaw) of the sensor using Kalman filtering (Leondes, 1970). Manned aircraft equipped with downward facing lidar scanners are commonly known also as airborne laser scanners (ALS). The first studies to utilize this technology in forestry mainly approached tree size estimates at the stand level, including mean tree height (Means et al., 2000; Naesset, 1997a; Nilsson, 1996), total basal area (Means et al., 2000), and total volume (Means et al., 2000; Naesset, 1997b). Single tree measurements, as opposed to stand or plot level estimates, from lidar point clouds were first

described by Hyypää (Hyypää, 1999; Hyypää et al., 2001), and others (Brandtberg, 1999; Ziegler et al., 2000) around the turn of the millennium.

The introduction of UAS equipped with lidar, henceforth referred to as unmanned airborne laser scanners (UALS), by Jaakkola et al. (2010) marks the convergence of UAS and lidar technologies from a forestry research standpoint. Soon after, Wallace et al., (2012a) demonstrated a system intended for obtaining single tree estimates for forest inventory; namely, tree location, height, and crown width. In the same year, Wallace et al. (2012b) showed that UALS can also be effective for detecting changes in forests over time. More recently, studies have compared point clouds from UALS with photogrammetric point clouds from UAS imagery, and there has been a general consensus that while UALS is capable of providing more accurate estimates, UAS used in conjunction with SfM are a useful, less expensive alternative (Guerra-Hernández et al., 2018; Moe et al., 2020; Wallace et al., 2016).

The life of a commercially grown coniferous tree begins with the seedling stage, where prior to planting the seedlings are kept in controlled environments, and are most susceptible to frost (O'Neill et al., 2000) and disease (Bloomberg, 1971). At this stage, while this dissertation was in progress, publications emerged showing that UAS are capable of detecting seedlings in a regeneration setting, (Feduck et al., 2018), and accurately counting them in plantations (Green and Burkhart, 2020; Quiros et al., 2018). However, prior to this work, no other studies have produced single seedling measurements from UAS. For research, seedlings are often grown in common gardens, which are plantings of individual trees in a common environment that allow economically feasible factorial comparisons of the phenotypic traits (e.g. growth rates, phenology, and drought tolerance) across or within source populations. Common garden experiments are useful tools for identifying populations which are genetically adept at coping with the major threats that a species faces. Comparisons may contain a suite of variables, not excluding hypotheses relating to how altered or changing environments affects the performance of populations (White et al., 2007). Scientific interest in common gardens experiments has increased among researchers focused on adaptation to climate change (Goodrich et al., 2018; Oleksyn et

al., 1998; Shaw and Eттerson, 2012). When common garden designs are used in forest investigations, dimensional variables, such as height, stem diameter, and crown diameter, are typically measured by hand, which is physically demanding and time consuming. Due to rapid growth of seedlings, their measurement should be conducted more frequently than with mature trees, which is not feasible in some cases due to the expense of obtaining the data. However, UAS can be deployed as often as necessary to capture the development of the seedlings accurately.

The goal of my dissertation is to examine how to use point cloud data to augment tree level estimates for forest inventory. Therefore, I have investigated two different stages in the life of a stand, before planting and before the regeneration harvests. In the second chapter, I focused on the initial stage of a stand by surveying a common garden experiment, whereas in the third and fourth chapters, a thinned stand represented a forest ecosystem ready to be replaced through harvesting. To investigate the initial stage of a stand, a small UAS was used to describe 150 seedlings grown together in a common garden, then I developed a procedure for estimating seedling sizes using a combination of digital photogrammetry and image processing, which is described in Chapter 2. For the maturity stage component of my research, a similar UAS was used to reconstruct a mature Douglas Fir stand located in the OSU- McDonald Dunn research forest. The UAS information was complemented with data acquired with two lidar platforms. One platform consisted of a larger UAS (UALS) equipped with a light lidar sensor, Velodyne Puck LITE, and one was a pickup truck equipped with heavier lidar sensor, Velodyne VLP 64E (MLS). In Chapter 3, I compared the overlapping digital 3D reconstructions produced from the three platforms in terms of locating the positions of treetops and tree stems. Furthermore, using the estimated positions I assessed the magnitude and direction of lean. I found that, due to its vantage point and sensor orientation, the MLS was better suited to assess the mature stems in detail compared to the other two platforms. In Chapter 4, I compared two methods for estimating stem lean from the MLS data. The more conservative lean estimate, which involves using the horizontal distance between the top and bottom of the merchantable portion of the stem, was included as a predictor to improve the fit of existing

nonlinear stem taper and volume equations. As a whole, my dissertation supports the usage of UAS and MLS to improve the quality and efficiency of remotely measuring single seedlings or mature trees forest inventory, while also identifying major limitations of the technology and recommending strategies to contend with them.

## 2. Augmenting Size Models for *Pinus strobiformis* Seedlings Using Dimensional Estimates from Unmanned Aircraft Systems

Cory Garms, Lluvia Flores-Rentería, Kristen Waring, Amy Whipple, Michael G. Wing, Bogdan Strimbu

Published in Canadian Journal of Forest Research - April 2020

DOI: [10.1139/cjfr-2019-0325](https://doi.org/10.1139/cjfr-2019-0325)

## Abstract:

In forestry, common garden experiments traditionally require manual measurements and visual inspections. Unmanned aircraft systems (UAS) are a newer method of monitoring plants that are potentially more efficient than traditional techniques. This study had two objectives: to assess the size and mortality of *Pinus strobiformis* seedlings using UAS, and to predict the second-year seedling size using manual measurements from the first year and from UAS size estimates. Raised boxes containing 150 seedlings were surveyed twice, one year apart, using multispectral UAS. Seedling heights and diameters at root collar (DRC) were measured manually both years. We found that size estimates made using a vegetation mask were suitable predictors for size, while spectral indices were not. Furthermore, we provided evidence that inclusion of UAS size estimates as predictors improves the fit of the models. Our study suggests that common variables used in forest monitoring are not necessarily best suited for seedlings. Therefore, we created a new variable, called the longitudinal area (height x DRC), which proved to be a significant predictor for both height and DRC. Finally, we demonstrate that seedling mortality can be effectively measured from remotely sensed data, which is useful for common gardens as well as regeneration studies.

Keywords: UAS, Common Garden, Multispectral, Pinus, SfM

## 2.1. Introduction

Southwestern white pine (*Pinus strobiformis*, SWWP) is a five-needle pine indigenous to the southwestern U.S. and Mexico. Climate change is predicted to cause SWWP populations to contract and shift northwards (Sáenz-Romero et al., 2010; Seager et al., 2007; Shirk et al., 2018; Williams et al., 2013). The predicted alteration of its geographic extent suggests that SWWP could be used as an indicator species to monitor climate change impacts. Additionally, SWWP is threatened by the non-native tree disease called white pine blister rust, caused by the fungal pathogen, *Cronartium ribicola* (Fairweather and Geils, 2011), which could also reduce its range. Forest management such as natural regeneration stimulation or augmentation by artificial regeneration may be necessary to ensure the future of SWWP given the combined peril of climate change and disease (Goodrich and Waring, 2017; Schoettle et al., 2018).

Common gardens are plantings of individual trees in a common environment that allow economically feasible factorial comparisons of the phenotypic traits (e.g. growth rates, phenology, and drought tolerance) from single or multiple source populations (Goodrich et al. 2018; Patterson et al. 2019). Common garden experiments are useful tools for identifying populations which are genetically adept at coping with the major threats that a species faces. Comparisons may contain a suite of variables, not excluding hypotheses relating to how altered or changing environments affects the performance of populations (White et al., 2007). Scientific interest in common garden experiments has increased among researchers focused on adaptation to climate change (Goodrich et al., 2018; Oleksyn et al., 1998; Shaw and Etterson, 2012). When common garden designs are used in forest investigations, dimensional variables, such as height, stem diameter, and crown diameter, are typically measured by hand, which is physically demanding and time consuming (Oleksyn et al., 1998; Valladares and Sánchez-Gómez, 2006). Directly monitoring physiological processes of individual plants (e.g., leaf water potential or stomatal conductance) requires sophisticated equipment in addition to the extensive time required for

measurements. Therefore, it is impractical to measure many individual trees at once (Van de Peer et al., 2018).

Existing models to predict conifer seedling growth are often based on physical variables, namely seedling height, diameter, and slenderness (seedling height divided by diameter at a preset height, usually at root collar). For mature trees, stem height growth is directly related to aboveground tree production, and stem diameter growth relates well to overall annual tree growth (Ryan and Yoder, 1997). Diameter measured at root collar (DRC) was shown to be positively correlated with root growth potential in *Pinus palustris* seedlings grown in different types of containers (South et al., 2005). Seedling slenderness calculated using height divided by DRC was shown to be correlated with light intensity and maternal tree characteristics for *Pinus thunbergii* (Mao et al., 2014).

Low-cost unmanned aircraft systems (UAS) are now available and can carry a variety of sensors capable of capturing visible (red, green, and blue), near-infrared, and thermal wavelengths (Wing et al., 2014). The use of UAS to estimate various tree attributes has many advantages compared to the use of manned aircraft, including high resolution and accuracy, reduced costs, temporal flexibility, and pilot safety (Banu et al., 2016). In fact, the lower resolution that is commonly supplied by manned aircraft are prohibitive for remotely detecting seedlings, whereas UAS have been shown effective for detecting conifer seedlings (Feduck et al., 2018). For instance, point clouds created using structure from motion (SfM) to digitally estimate 3D structures from 2D imagery can be used to accurately measure trees for a variety of forestry analyses, including research (Tang and Shao, 2015), inventory (Puliti et al., 2015), and post-harvest inspection (Puliti et al., 2018). A good summary of current forestry applications of UAS in Europe, including forest mensuration, species classification, fire monitoring, and disease mapping was written by Torresan et al., (2017). Orthophotos from UAS imagery have been proven effective for detecting the locations of small conifer seedlings using only spectral information (Feduck et al., 2018). Also, seedling mortality has been accurately detected using UAS in a reforestation plantation setting (i.e., spaced farther apart than in common gardens) (Gil-Docampo et al., 2020). With sufficient coverage and resolution, these photogrammetric remote sensing techniques are presumably also suitable for

estimating size and mortality of individual seedlings in common gardens. If proven effective in common gardens, UAS-based seedling survey techniques could also be applied to silvicultural operations such as natural regeneration surveys (Goodbody et al., 2018).

Data collection with UAS can be more rapid and less expensive than traditional common garden measurement methods. Because common garden measurement needs are often related to tree size, UAS could be used to provide valuable supplementary data to these studies. Therefore, this study had two objectives: first, to assess the size and mortality of *Pinus strobiformis* seedlings using UAS, and second, to predict the second-year seedling size using manual measurements from the first year and UAS size estimates from both years.

## 2.2. Methods

### 2.2.1. Background and Data Collection

A common garden experiment was planted in October 2015 at The Arboretum at Flagstaff, Arizona, USA, located about 15 km southwest of the City of Flagstaff. One-year-old SWWP seedlings were planted in a nine by nine grid arrangement in wooden raised bed boxes, measuring 0.61 m tall  $\times$  1.22 m  $\times$  1.22 m wide. The planting media was 50% basic Cornell soil mix, consisting of 1-part sphagnum peat moss, 1-part horticultural perlite and 1-part coarse vermiculite, and 50% cinders, for aeration.

Seedling DRC and seedling height to base of terminal bud (height) were measured by hand, along with other seedling traits. For this study, two bed boxes were used, and two sets of ground-based measurements taken approximately one year apart: May 18, 2017 and June 2, 2018. The DRC was measured with 0.01 mm precision and the seedling height with 1 mm precision. Visual observations of seedling mortality revealed that 15 of the 150 seedlings (10%) planted in 2017 had died by 2018. Additionally, six seedlings, all located on the north edges of the boxes, were undistinguishable from adjacent weeds in the imagery. Both, the dead and the undistinguishable seedlings were omitted from growth prediction models, which left a total of 129 seedlings for modeling.

To acquire the remotely sensed data, we used a UAS consisting from a DJI Phantom 4 retrofitted to carry a Micasense Rededge© multispectral sensor (Table 1). The common garden boxes were imaged by manually piloting the UAS twice (June 30, 2017, and June 25, 2018) in a grid pattern 15 meters above the ground with sensors programmed to capture images once per second. Nearby obstructions, such as trees and tall fence, made automated grid missions infeasible for this scene. The small size of the area that included both boxes ( $\sim 10\text{m}^2$ ) meant that we could obtain the necessary imagery at low altitude with minimal variation between flight missions across years. Weather conditions were favorable for data collection: clear skies (clouds less than 10%), light variable winds (speed less than 5 m/s), and satisfactory temperatures (28.2 and 28.6°C for 2017 and 2018, respectively). Flights were approximately 5 minutes long per platform and were conducted within 30 minutes of solar noon (i.e., around 12:30 pm both years).

Table 2-1: Characteristics of the UAS used to image common garden boxes near Flagstaff, Arizona, USA in 2017 and 2018.

<b>Quadcopter Airframe</b>	DJI Phantom 4
<b>Sensor Model</b>	Micasense Rededge
<b>Wavelength center/bandwidth (nm)</b>	475/20 560/20 668/10 717/10 840/40
<b>Focal Length (mm)</b>	5.5
<b>Imager Size (mm)</b>	4.8 x 3.6
<b>Sensor Resolution (pixels)</b>	1280 x 960
<b>Pixel Size (<math>\mu\text{m}</math>)</b>	3.75
<b>Altitude AGL (m)</b>	15
<b>GSD @ nadir (cm/pixel)</b>	1.02

### 2.2.2. Image Preprocessing

To ensure compatibility among repeated flights, the UAS imagery was radiometrically corrected, converting from raw 16-bit digital number values to reflectance (%). This was performed using pre- and post-flight images of the Micasense calibrated reflectance panel based on an empirical line method (Tu et al., 2018; Whiteside and Bartolo, 2016). Radiometrically corrected multispectral images were used to create digital 3D reconstructions via Agisoft Photoscan© (Agisoft, 2017). Agisoft Photoscan© uses structure from motion (Westoby et al., 2012) and the geolocation data registered during image

acquisition to create photogrammetric point clouds, orthophotos, and digital elevation models. The workflow we used followed the recommendations of Rossi et al. (2012) and Turner et al. (2014), tailored to our research, namely photo alignment was executed using at most 100,000 and 40,000 key and tie points, respectively, and the box corners were used as Ground Control Points (GCPs). The resulting mosaic was scaled using the known dimensions of the boxes (x, y, z). Final geo-referencing root-mean-square errors (RMSE) of the 2017 and 2018 dataset GCPs were 1.1 cm and 1.8 cm, respectively for horizontal plane, whereas for the vertical plane the scaling RMSEs were 5.1 cm and 4.7 cm for 2017 and 2018, respectively. The 5-band orthophoto and photogrammetric DEM were exported from Photoscan as geotiff files (Ritter and Ruth 1997) at the highest possible resolutions, which were 0.88 x 0.88 cm and 0.92 x 0.92 cm for 2017 and 2018, respectively. Using the reflectance values from the red (663-673 nm) ( $R_{Red}$ ) and near infrared (820-860 nm) ( $R_{Near IR}$ ) bands from the orthophoto, the normalized difference vegetation index (NDVI) (Rouse Jr et al., 1974) was calculated as follows:

$$NDVI = \frac{R_{Near IR} - R_{Red}}{R_{Near IR} + R_{Red}} \quad (1)$$

Using the reflectance from the red edge band ( $R_{Red Edge}$ ) the red edge chlorophyll index (RECI) (Gitelson, 2005) was calculated as follows:

$$RECI = \frac{R_{Near IR}}{R_{Red Edge}} - 1 \quad (2)$$

All data were referenced to NAD83 (2011) 2010.00, with coordinates in the UTM zone 12N projection (EPSG:26912). Due to positional errors in the GPS locations stored in the image metadata, the reconstructions of the boxes from 2017 and 2018 were not initially aligned with one another. However, we coregistered the orthophoto from 2018 to the one from 2017 using the corners of the boxes (8 in total) as reference points and an affine transformation, which led to a final registration error of 0.8 cm. Image coregistration was performed using QGIS (QGIS Development Team, 2015).

### 2.2.3. Point Cloud Processing

The photogrammetric point clouds were exported from Photoscan and stored in ASPRS LAS format (Board, 2008). To coregister the point cloud data, we segmented the points within the boxes, then

aligned the boxes individually across years. To do this, we first aligned the box centers visually, then used points on the underside of the cloud near the box corners to perform an affine transformation. The final RMSE for the point cloud coregistrations were 1.8 cm and 2.3 cm for box 1 and box 2, respectively. However, some of the error is due to changes in the seedlings, so it is not necessarily a good indication of the true spatial alignment of the point clouds. Visually, the seedling locations within the boxes appeared to be well aligned following this procedure, which we accomplished using Cloudcompare (Girardeau-Montaut, 2015). Despite the data collection and preprocessing being identical, the raw point clouds from the 2017 imagery were nearly 4 times as dense as those from 2018. Though there was a large difference in point density, there was not a discernable difference in the detail of the seedling crown shapes across the years (Figure 2-1), which is unsurprising considering that even the lowest resolution cloud had in excess of 22 points/cm<sup>2</sup> (Table 2).

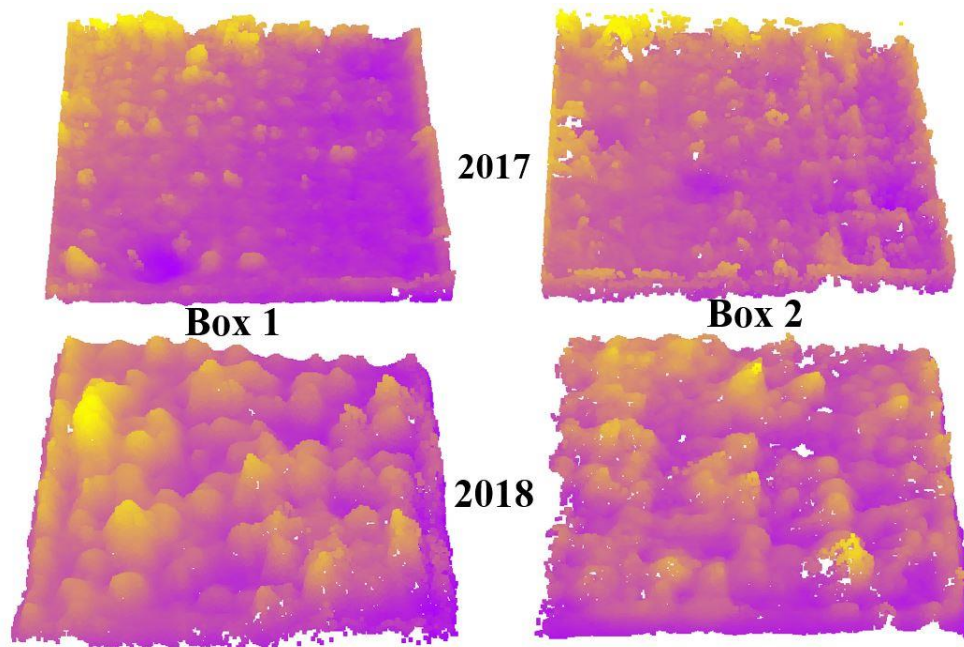


Figure 2-1: Rendering of point clouds of seedlings growing in two common garden boxes created using structure from motion photogrammetry. The clouds are colored according to height value ( $z$ ) from purple (low) to gold (high). Clouds on the top row are from 2017 imagery, and clouds on the bottom row are from 2018 imagery.

Table 2-2: Point cloud statistics within common garden boxes created using structure from motion photogrammetry.

<b>Year</b>	<b>Box</b>	<b>Points</b>	<b>Points/cm<sup>2</sup></b>	<b>Ground Points /cm<sup>2</sup></b>
2017	1	166,804	93.87	74.02
2017	2	172,664	98.85	46.42
2018	1	54,426	28.83	18.96
2018	2	39,069	22.84	13.62

To detect the ground within the boxes, we used a progressive morphological filter with a window size of 8 cm x 8 cm and a threshold of 0.5 cm (Zhang et al., 2003). The values we chose to parameterize the ground filter were derived by trial-and-error but resulted in ground points being relatively uniformly distributed across the boxes for all point clouds (Figure 2-2).

Ground points were used to create a digital terrain model (DTM) (Figure 2-3), which subsequently provided point cloud normalization (i.e., subtracting the ground elevation from all points). From the normalized clouds we created a canopy height model (CHM) (Figure 2-4). The DTMs and CHMs were created with 1cm<sup>2</sup> spatial resolution, which was selected for being the closest integer to the DEM resolution (0.88 cm and 0.92 cm for 2017 and 2018, respectively). Point cloud processing tasks were carried out using the R packages “raster” and “lidR” (Hijmans and Van Etten, 2014; Roussel, 2017). Because the seedlings were larger in the second year, ground visibility was decreased. A lack of ground returns results in holes in the DTM, therefore, we used a depression filling algorithm (Planchon and Darboux, 2002) to remove the holes left by the seedlings.

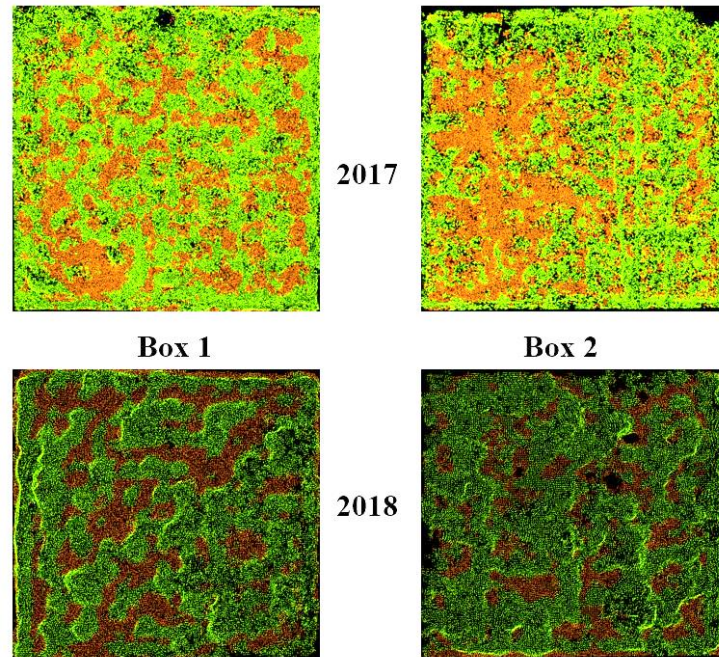


Figure 2-2 Point clouds of common garden boxes viewed from above showing classification of ground (orange) and non-ground (green). The clouds from 2018 (bottom) were several times less dense in terms of points/cm<sup>2</sup> than the clouds from 2017, which caused them to look less bright in the rendering.

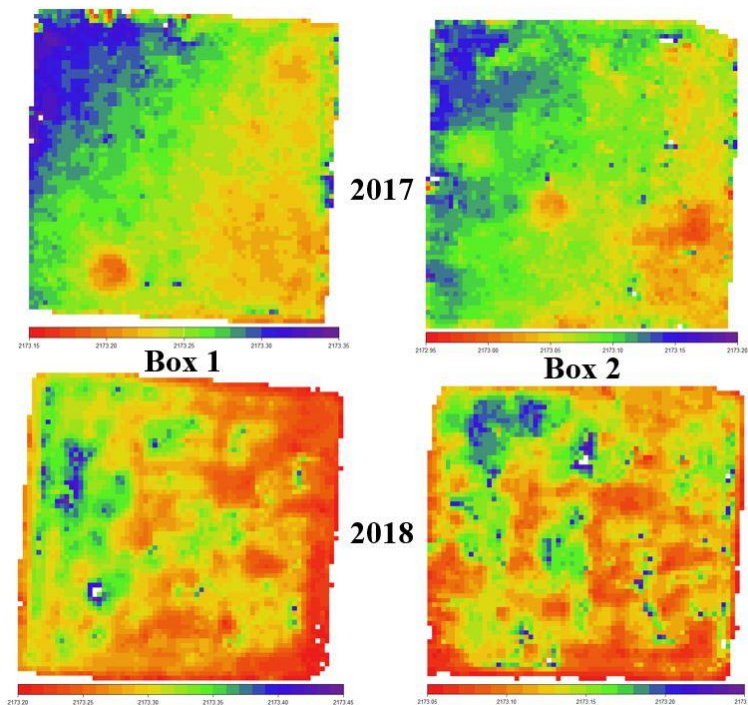


Figure 2-3 Digital terrain models (DTM) for the two common garden boxes in the study created from UAV flights in 2017 (top) and 2018 (bottom). The scale bars show elevation above mean sea level (m).

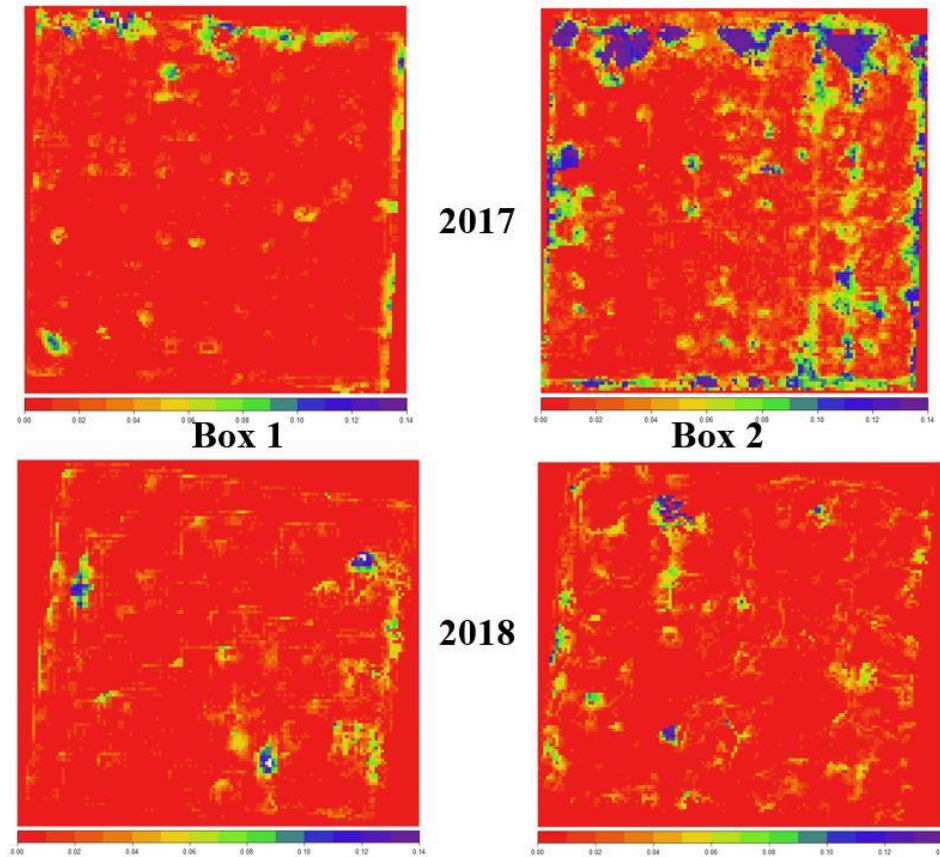


Figure 2-4: Canopy height models (CHM) for the two common garden boxes in the study created from UAV flights in 2017 (top) and 2018 (bottom). The scale bars show height above ground (cm)

#### 2.2.4. Seedling Size Estimation

To measure the seedlings, first we delineated the vegetation from the ground, which was achieved by creating vegetation masks for the 2017 and 2018 orthophotos. To create the masks, maximum likelihood supervised classifications with no added threshold (Jia and Richards, 1994) were performed separately for each year, using the NDVI and RECI layers as inputs. The training data for the classifiers consisted of ten polygons, each 12 pixels or larger, for three cover classes: seedlings, ground, and artificial material. Following the classification, we extracted the pixels that were classified as seedling, then vectorized them such that the contiguous seedling pixels formed polygons. At this stage, the plants had been effectively segmented from the background, but several crowns overlapped. In the cases where the crowns overlapped, we separated them visually. The masking process was accomplished using QGIS (QGIS Development Team, 2015), the QGIS semi-automatic classification plugin (SCP)

(Congedo, 2016), and the system for automated geoscientific analyses (SAGA) software (Conrad et al., 2015).

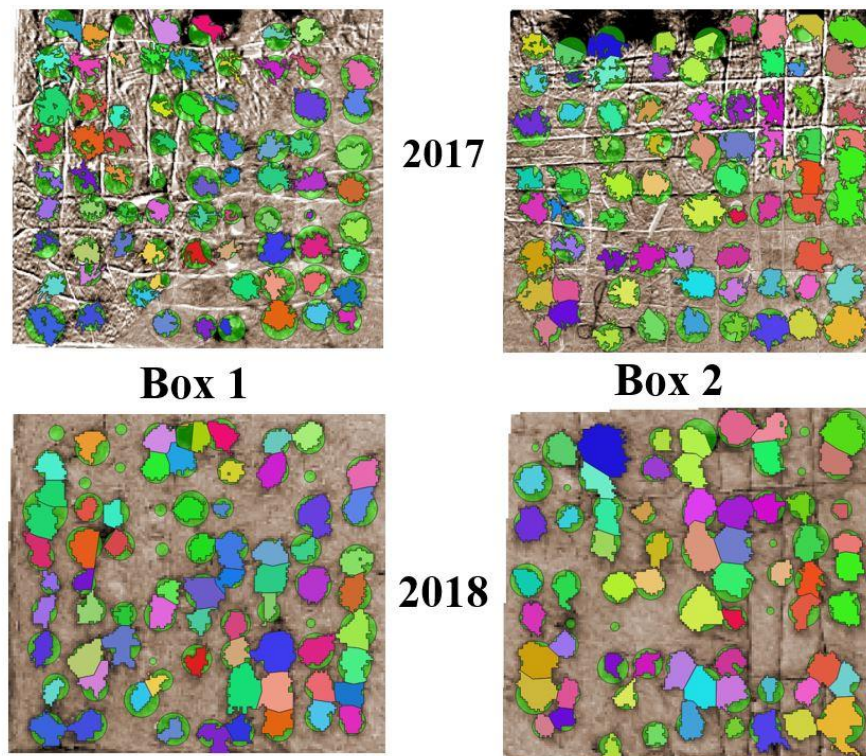


Figure 2-5: Vegetation mask vectors superimposed over NDVI from multispectral imagery of common garden boxes in 2017 (top) and 2018 (bottom). Circular plant crown vectors are shown in green.

Once the mask was created, we used it along with the orthophoto, NDVI layer, and ground measurements to represent the generalized seedling crown areas. Visual delineations are often used as controls for segmentation of trees from remotely sensed images (Koch et al., 2014; Ozdemir, 2008; Wang et al., 2004). Because common garden experiments can have large samples, detailed manual delineation of seedlings is impractical, so we identified the crown visually with circles. The crown circles were created by fitting a circle to three points which were placed around the margins of the plant, constrained that the circles do not overlap (Figure 2-5). After the crown circles were created, their identities were verified according to their positions within the boxes (i.e., row and column), which allowed for manual measurements and remotely sensed estimates to be merged.

The maximum height of each seedling was estimated from the remotely sensed data in three ways. First, we calculated the heights of the seedlings using the DEM and the vegetation mask. This was accomplished by finding the difference between the maximum and minimum  $z$  values for pixels that fell into each circular seedling crown vector. The maxima were selected using only pixels which were classified as vegetation according to the mask, and the minima were selected using only non-vegetation pixels. This height estimate is termed  $Height_{Mask}$ . Second, we calculated the heights by finding the local maxima with respect to  $z$  where the plant crowns intersected the CHM layer, referred to as  $Height_{CHM}$ . The vegetation mask was not used in this calculation, to account for small discrepancies in the alignment of the data and for geometric simplification that occurs during the SfM point cloud generation process. Third, we calculated the local ground elevation for each seedling by finding the minimum ( $z$ ) within the crown from the DTM raster, then subtracted it from the local crown maxima from the DEM. These estimates are referred to as  $Height_{DTM}$ , and they also did not involve any vegetation masking.

We computed the crown area in two ways. First, we estimated it by computing the area of the circular vectors that we fit around the seedlings for both years, which are referred to as  $Area_{Circle}$ . Second, we multiplied the number of pixels classified as vegetation according to the mask layer within each circle by the ground footprint area of one pixel in the image. These are referred to as  $Area_{Mask}$ . Estimated seedling crown area and height were used to produce two different seedling volumes. First, we fit cylinders around the seedlings using the height estimated from the DTM and the crown vectors as follows:

$$Volume_{Cylinder} = Height_{DTM} * Area_{Circle} \quad (3)$$

Second, we calculated the volume of the space that would be occupied by extending the mask layer vertically from the ground to the height of the seedling estimated from the DEM and vegetation mask as follows:

$$Volume_{Mask} = Height_{Mask} * Area_{Mask} \quad (4)$$

Two slenderness estimates were also produced from the remotely sensed data similarly to the way volume was estimated. First, we computed the diameter of the crown as  $Diameter = 2 * \sqrt{\frac{Area}{\pi}}$ , then computed two values for slenderness:

$$Slenderness_{Circle} = \frac{Height_{DTM}}{Diameter_{Circle}} \quad (5)$$

and as follows:

$$Slenderness_{Mask} = \frac{Height_{Mask}}{Diameter_{Mask}} \quad (6)$$

### 2.2.5. Variable Selection

This study was focused on variables commonly used to describe the size of a seedling, namely the height and DRC (Collet et al., 2001; South et al., 2005). However, other variables can describe the size and shape of a seedling. We therefore also considered the slenderness (i.e., height /DRC) (cm/mm) as well as a proxy for longitudinal area (height x DRC) (cm × mm). We conducted an initial assessment of the relationships between the variables based on scatterplots and correlation coefficients, which suggested that the most suited response variables for size were height, DRC, and longitudinal area (LA). Nevertheless, considering the ubiquity of slenderness (height-to-diameter ratio) in forest analyses, we also included it.

After we established the most appropriate variables to describe the size of the seedlings, we investigated the ability of the mean spectral responses (i.e., mean NDVI, mean RSVI, etc.) to predict their dimensions. In addition to the NDVI and RSVI, we also tested four other remote sensing indices: triangular greenness index (Hunt Jr et al., 2013), green red vegetation index (Barnes et al., 2000), green NDVI (Gitelson et al., 1996), and green chlorophyll index (Gitelson, 2005). Nevertheless, correlation coefficients suggested that none of the spectral variables were suitable for modeling the size of the seedlings. Therefore, we considered 24 predictor variables, including four seedling dimensions measured on the ground in 2017 or derived from those measurements: height, DRC, slenderness, and longitudinal

area. From the remotely sensed data, we included 10 variables for each year: three height estimates (i.e.,  $Height_{CHM}$ ,  $Height_{DTM}$ , and  $Height_{Mask}$ ), two area estimates, two volume estimates, two slenderness estimates, and the distance to nearest surviving neighbor,

To narrow the number of predictors we used a nonparametric approach which is based on classification and regression trees (Breiman et al., 1984; Gutiérrez et al., 2009), namely the Boruta algorithm (Kursa and Rudnicki, 2010). The classification and regression trees can supply superior results over parametric selection procedures, but they can be difficult to interpret and have limited generalization power (Niuniu and Yuxun, 2010). Nevertheless, when used to supply the possible inputs for a subsequent model building, the complex non-parametric approaches are appropriate and provide a ranking of explanatory variables (Genuer et al., 2010).

The Random Forests (RF) algorithm is a nonparametric classification technique that combines classification and regression trees with bagging algorithms. When RF is implemented, a large number of regression trees are created whose votes are used to compute the classification likelihood (Breiman, 2001). The Boruta procedure is a wrapper (i.e., a function used to call a set of functions and display the results in a user friendly format) that was built around the R package ‘randomForest’ (Liaw and Wiener, 2002). Boruta makes permutations of all the variables in the data, known as shadow attributes, shuffles them into the data, then runs the RF algorithm on the resulting dataset. The Z-scores of the original variables are iteratively compared with the Z-scores of the shadow attributes, and the predictors are ranked based on their measured importance. The variables that are significantly more important than shadow variables are deemed ‘important’, while those that are significantly less important are deemed ‘unimportant’, and any variables left without a decision after all trees are labeled ‘tentative’. To run the procedure and create variable importance plots for each response variable, we used the R package “Boruta” with the default confidence level ( $p \leq 0.01$ ) and found that 10,000 runs reduced the number of ‘tentative’ predictor variables to one or fewer per response (Kursa et al., 2018). To examine the relationships between pairwise combinations of response variables and those predictors which were

deemed ‘important’ according to the Boruta procedure, we constructed correlation matrices (Wei and Simko, 2015).

### 2.2.6. Linear Regression Models

To model the relationship between the four response variables and the set of predictors chosen via Boruta we used linear regression, considering that two measurements are used (2017 and 2018). To assess the importance of the remotely sensed variables in predicting the size and mortality of the seedlings, we also modeled each response variable using only the ground-based measurements as predictors. To identify only the significant variables, we started by including all the candidate variables in the linear regression model, then removed the least significant variables (the threshold removal p-value was 0.1).

To ensure the validity of the models we tested the linear regression assumptions of normality, homoscedasticity, and independence. The Shapiro-Wilks test was used to test normality of the residuals, the Breusch-Pagan test assessed the homogeneity of the variance, whereas the Durbin-Watson test evaluated the lack of autocorrelation. In addition to the regression assumptions, we checked the fulfillment of the computational requirements, namely absence of outliers, with studentized deleted residuals and hat matrix leverage, presence of influential observations, using Cook’s distance, and absence of collinearity, using variance inflation factor (Neter et al., 1996). To compare the models, we calculated the coefficient of determination ( $R^2$ ) (Miles, 2014), root mean squared error (RMSE) (Levinson, 1946), Akaike information criterion (AIC) (Akaike, 1987), and residual standard error (RSE).

### 2.2.7. Mortality Prediction

The size of the crown circles delineating seedlings was selected according to the crown dimensions from the vegetation mask. Therefore, some dead seedlings had no pixels classified as vegetation, as the mask fell within the circular vector for 2018. The absence of seedlings in 2018 enabled us to estimate mortality from the remotely sensed data. Seedlings that did appear in 2017 and were undetectable in

2018 were considered ‘dead’, while seedlings which had non-zero crown area according to the vegetation mask in both years were considered ‘living’.

## 2.3. Results

### 2.3.1. Variable Selection

For the dependent variable height, Boruta deemed 17 variables as important, with longitudinal area and height from the previous year being the most relevant predictors (Figure 2-6a). For DRC, there were 11 variables deemed important and one tentative, with DRC and longitudinal area from the previous year leading in importance (Figure 2-6b). For slenderness, 12 variables were deemed important and one deemed tentative; with slenderness and height from the previous year having the largest impact (Figure 2-6c). For longitudinal area, there were 16 variables found important, and longitudinal area and height from the previous year were ranked as the most influential (Figure 2-6d). Summary statistics for all predictor and response variables included in the models are listed in Table 2-3.

Table 2-3: Descriptive statistics for ground-based measurements (bold) and remotely sensed estimates

<b>Variable</b>	<b>Mean</b>	<b>St. Dev.</b>	<b>Min</b>	<b>Max</b>
<b>Height 2017</b>	9.69	1.753	5.40	14.20
<b>Height 2018</b>	14.34	3.224	7.60	26.30
<b>Diameter at Root Collar 2017</b>	4.182	0.499	2.870	5.63
<b>Diameter at Root Collar 2018</b>	5.70	0.811	3.58	8.01
<b>Slenderness 2017</b>	2.34	0.458	1.329	4.089
<b>Slenderness 2018</b>	2.523	0.467	1.561	4.083
<b>Longitudinal Area 2017</b>	40.79	10.099	19.53	76.00
<b>Longitudinal Area 2018</b>	83.25	27.699	34.17	210.66
Height (CHM) 2017	6.092	4.293	0.70	21.5
Height (DTM) 2017	7.79	4.415	1.27	23.95
Height (Mask) 2017	10.246	4.425	3.613	38.159
Area (Circle) 2017	80.60	26.85	17.64	148.75

Area (Mask) 2017	55.897	23.89	3.685	138.796
Volume (Circle) 2017	656.14	481.21	22.39	2344.49
Volume (Mask) 2017	611.46	457.25	36.44	3020.26
Slenderness (Cylinder) 2017	1.177	0.4119	0.445	3.3868
Slenderness (Mask) 2017	1.2775	0.5773	0.5012	4.5648
Height (CHM) 2018	5.719	3.01	1.30	18.8
Height (DTM) 2018	8.38	3.15	3.17	21.75
Height (Mask) 2018	5.847	2.42	1.416	16.04
Area (Circle) 2018	82.19	30.685	32.28	180.45
Area (Mask) 2018	73.68	31.95	18.22	212.21
Volume (Circle) 2018	723.0	476.88	161.4	2787.1
Volume (Mask) 2018	464.71	358.44	44.22	2849.5
Slenderness (Cylinder) 2018	0.61	0.252	0.1825	1.8688
Slenderness (Mask) 2018	0.6214	0.237	0.2246	1.5907

Figure 6: Variable importance plots for the four dependent variables selected as representative for seedling size: total height (a.), diameter at root collar (DRC) (b.), slenderness (c.), and longitudinal area (d.). The y-axes of the figures represent importance measured by the Boruta algorithm. The boxes contain the values within the max and min importance values for 10k iterations with whiskers equal to 1.5 times the interquartile range. Green boxes indicate variables deemed important according to Boruta ( $p(z) < 0.01$ ), while red boxes were deemed unimportant, and yellow boxes were deemed tentative.

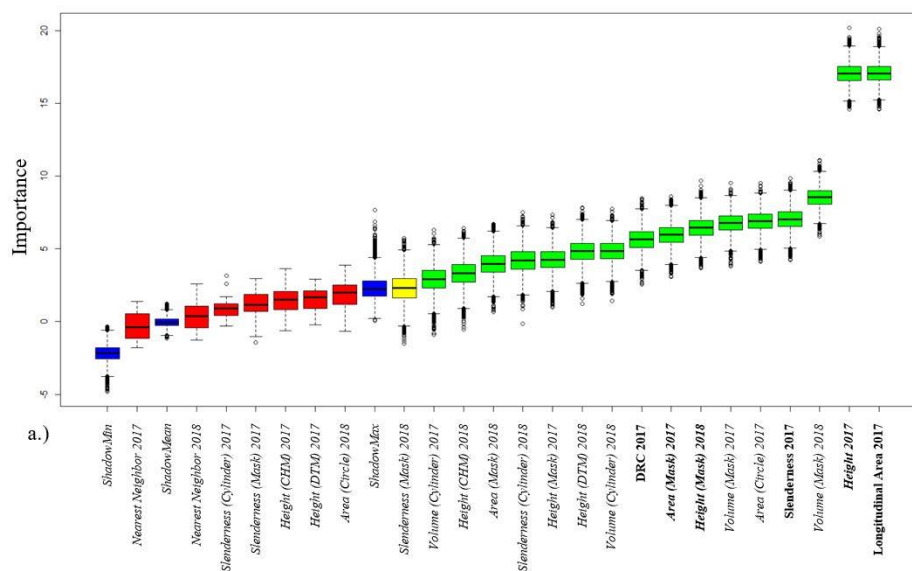


Figure 2-6a: Variable importance plot for the dependent variable total height.

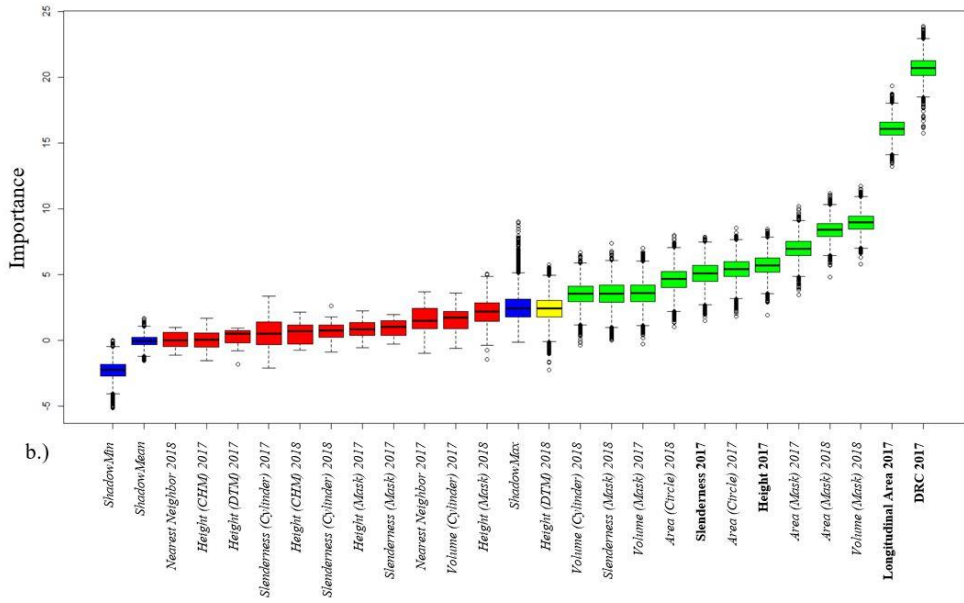


Figure 2-6b: Variable importance plot for the four dependent variable diameter at root collar (DRC).

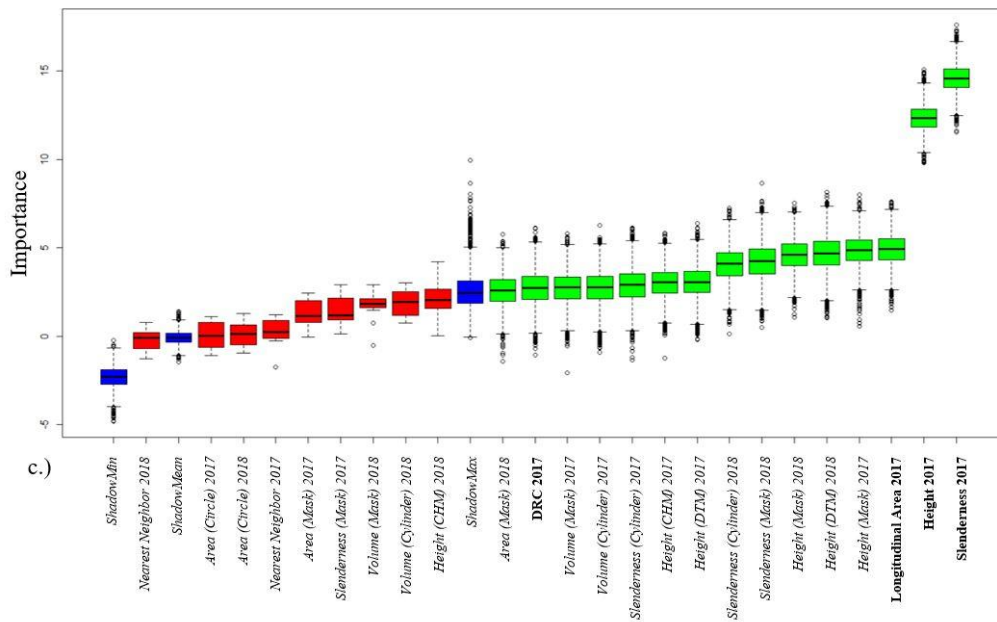


Figure 2-6c: Variable importance plot for the four dependent variable seedling slenderness.

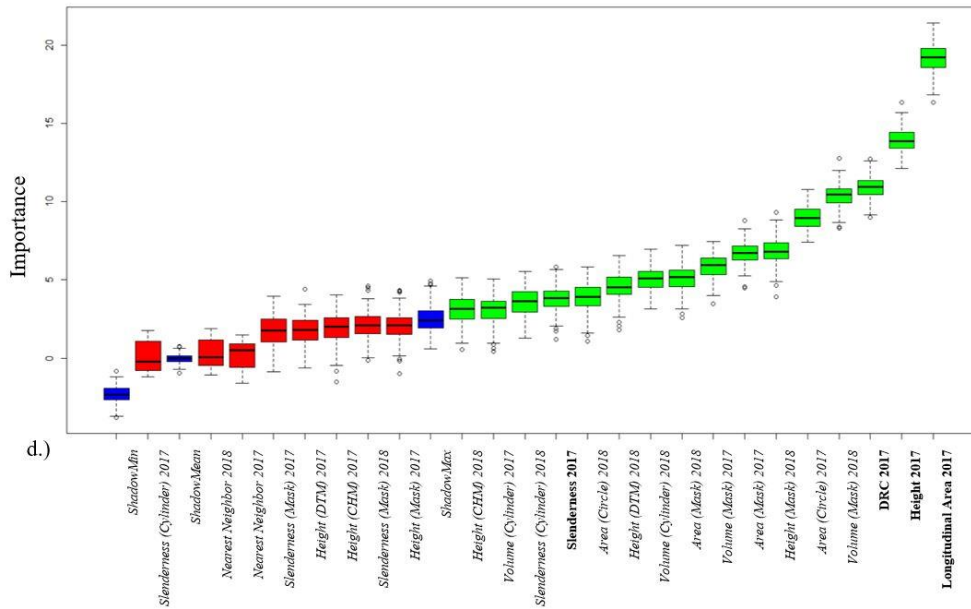


Figure 2-6d: Variable importance plot for the four dependent variable longitudinal area.

We found that the Pearson's product moment correlation coefficients ( $r$ ) between the three height estimates from the remotely sensed data were larger in 2017 than in 2018 (Figure 2-7), ranging from 0.6 to 0.98 and from 0.21 to 0.91, respectively. For both 2017 and 2018, the point cloud based height estimates  $Height_{CHM}$  and  $Height_{DTM}$  were showed larger correlation with one another ( $0.91 < r < 0.98$ ) than with  $Height_{Mask}$  ( $0.21 < r < 0.58$ ). However, compared to the ground-based measurements, height, DRC, slenderness and LA, the raster-based height estimates  $Height_{Mask}$  had the strongest correlations. The  $Height_{Mask}$  was the only height estimate that had a significant ( $p < 0.001$ ) correlation with the response variables height and DRC. None of the height estimated variables were significantly correlated with slenderness, while all of them were significantly correlated with LA. For the response variable LA, the  $Height_{Mask}$  had the strongest correlation ( $0.46 < r < 0.52$ ). followed by  $Height_{DTM}$  ( $0.3 < r < 0.42$ ), then  $Height_{CHM}$  ( $0.29 < r < 0.39$ ).

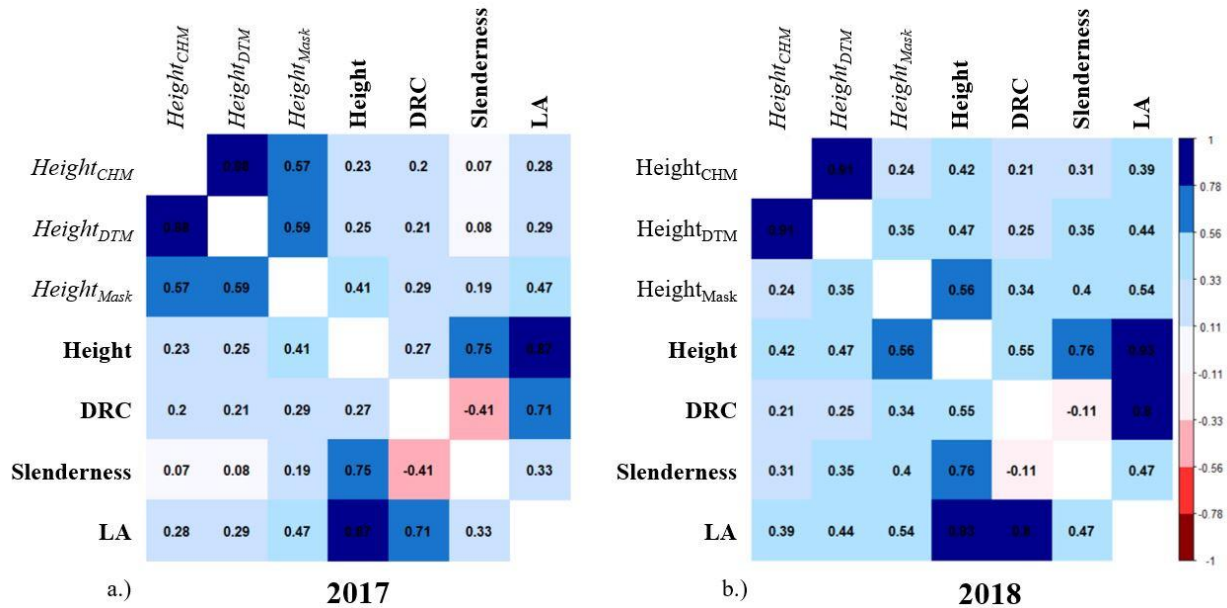


Figure 2-7: Correlation matrices showing Pearson correlation coefficients ( $r$ ) among height predictions from UAS (italics) and ground-based measurements (Bold) in 2017 (a.) and 2018 (b.). Cell are shaded according to the strength of significant relationships based on Pearson's product moment correlation coefficient ( $p < 0.001$ ) and colored according to correlations being positive (blue) or negative (red).

Projected crown area, volume, and slenderness show a large correlation ( $0.77 < r < 0.93$ ) with the slenderness estimates, namely  $Slenderness_{Cylinder}$  and  $Slenderness_{Mask}$ . The crown area and volume estimates had similar correlation coefficients, between  $r = 0.47$  and  $r = 0.68$ . Unlike the height estimates the crown area and volume estimates mostly seems to be correlated with the response variables from 2018 rather than the ones from 2017. The correlations between the  $Area_{Mask}$  and  $Volume_{Mask}$  and the response variables ( $0.3 < r < 0.51$ , excluding slenderness) are smaller than between the  $Area_{Circle}$  and  $Volume_{Cylinder}$  and the responses ( $0.37 < r < 0.7$ , excluding slenderness). The largest correlations between predictor variables and one of the responses were between the 2018  $Area_{Mask}$  and  $Volume_{Mask}$  and the LA (Figure 2-8), which were  $r = 0.68$  and  $0.7$ , respectively.

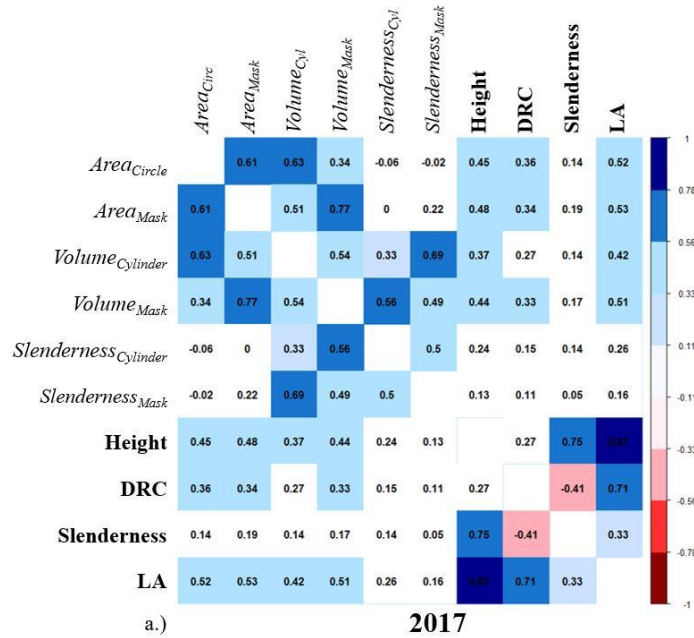


Figure 2-8a: Correlation matrices showing Pearson correlation coefficients (R) among area, volume, and slenderness estimates from UAS (italics) and ground-based measurements (Bold) in 2017. Cell are shaded according to the strength of significant relationships based on Pearson's product moment correlation coefficient ( $p < 0.001$ ) and colored according to correlations being positive (blue) or negative (red).

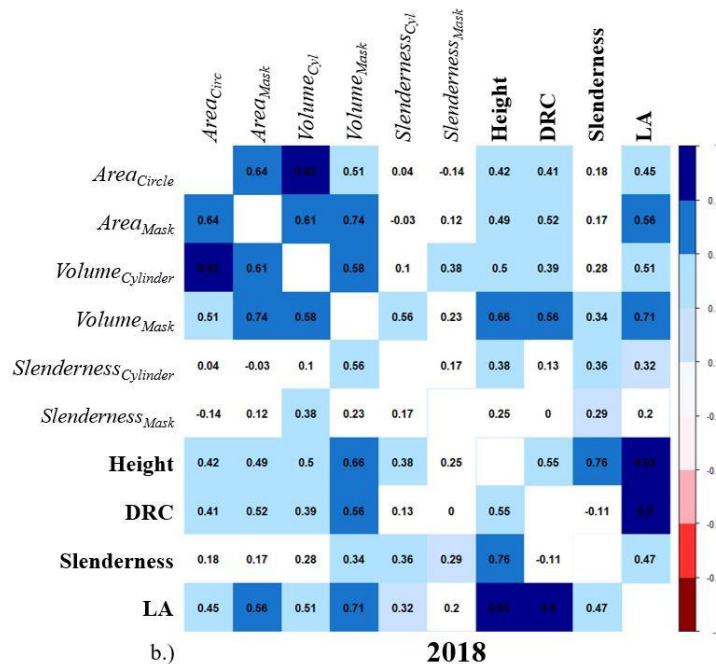


Figure 2-8b: Correlation matrices showing Pearson correlation coefficients (R) among area, volume, and slenderness estimates from UAS (italics) and ground-based measurements (Bold) in 2018. Cell are shaded according to the strength of significant relationships based on Pearson's product moment correlation coefficient ( $p < 0.001$ ) and colored according to correlations being positive (blue) or negative (red).

### 2.3.2. Linear Regression Models

The linear regression models for all four response variables included more than one predictor (Table 2.4). However, the models exhibited a large amount of variability, as the  $R^2$  was at most 0.84 (i.e., for longitudinal area). The precision of the models improved when remotely sensed variables were included, the root mean squared error (RMSE) decreasing by as much as 12% (i.e., 1.75 cm to 1.54 cm (12%) for height, 0.50 to 0.47 mm (6%) for DRC, 0.36 to 0.33 (8%)  $\text{cm}\times\text{mm}^{-1}$  for slenderness, and 12.63 to 11.11  $\text{cm}\times\text{mm}$  (12%) for LA). The models met all regression assumptions, as the residuals were normally distributed according to the Anderson-Darling test ( $p > 0.05$ ), homoscedastic according to the Breusch-Pagan test ( $p > 0.05$ ), and exhibited no autocorrelation according to the Durban-Watson test ( $p > 0.01$ ). According to  $R^2$ , the longitudinal area was identified as the most suitable variable to represent the size of seedlings (i.e., 0.84), followed by height (i.e., 0.77), RCD (i.e., 0.65), and slenderness (i.e., 0.47).

Table 2-4: Linear regression models predicting 2018 seedling size (n=129). The odd numbered columns display the final models for the seedling size variables, and the even numbered columns contain only the ground-based predictors. Predictor variables measured on the ground or derived from ground-based measurements are in bold. Values in parentheses represent standard error of the coefficients above them (\*  $p \leq 0.05$  \*\* $p \leq 0.01$  \*\*\* $p \leq 0.001$ ).

Predictor Variable:	Response Variable:							
	Height <sub>2018</sub>		Diameter <sub>2018</sub>		Slenderness <sub>2018</sub>		Longitudinal Area <sub>2018</sub>	
	(1)	(2)	(3)	(4)	(5)	(6)	(7)	(8)
<b>Height 2017</b>	0.458**	0.447***				0.110***	-2.232*	-15.845**
	(0.163)	(0.031)				(0.029)	(0.-226)	(4.832)
<b>Diameter at Root Collar 2017</b>			0.940***	0.833***				-34.345**
			(0.098)	(0.129)				(11.889)
<b>Slenderness 2017</b>					0.495***	0.254*		
					(0.067)	(0.096)		
<b>Longitudinal Area 2017</b>	0.144***	0.197***		0.026***			2.223***	6.016***
	(0.031)	(0.032)		(0.006)			(0.226)	(1.146)
Volume (Mask) 2018		0.004***					0.0264***	
		(0.001)					(0.005)	
Volume (Mask) 2017					0.003***			
					(0.000)			
Area (Circle) 2017			0.006**				0.143**	
			(0.002)				(0.045)	
Area (Mask) 2017	0.025**							
	(0.008)							
Area (Mask) 2018	-0.030**		0.005**				-0.118*	
	(0.009)		(0.002)				(0.063)	
Slenderness (Cylinder) 2018					0.459***			
					(0.121)			
Intercept	3.121***	1.966	0.892*	1.029**	0.897*	0.860***	-0.947	135.048**
	(0.849)	(0.915)	(0.369)	(0.357)	(0.170)	(0.188)	(6.249)	(49.428)
R <sup>2</sup>	0.77	0.70	0.65	0.61	0.47	0.38	0.84	0.79
RMSE	1.54	1.75	0.47	0.50	0.33	0.36	11.11	12.63
AIC	492.23	518.71	184.58	197.37	96.13	113.61	1001.40	1030.45
Residual Std. Error	1.58	1.77	0.48	0.51	0.34	0.37	11.38	11.38

### 2.3.3. Mortality Prediction

The predicted mortality values based on the remotely sensed data were aligned with the observed mortality, as among the 135 living seedlings and 15 dead seedlings, out of the 150 seedlings only two were misclassified (Table 2-5).

Table 2-5: Confusion matrix showing predicted versus observed mortality for SWWP seedlings based on remotely sensed vegetation filtering and visual inspections on the ground. Over 90% of dead seedlings and over 98% of the total sample were correctly classified based on mortality that occurred between the observations in 2017 and 2018.

n=150	Predicted: Living	Predicted: Dead	
Actual: Living	134	1	135
Actual: Dead	1	14	15
	135	15	

## 2.4. Discussion

### 2.4.1. UAS Data Collection and Extraction

The initial spacing of the seedlings constrains the length of time that remote sensing techniques may be used to effectively estimate seedling size. Once the seedlings are not spatially distinguishable from one another from above, estimating seedling size using UAS becomes nonviable. In this study, the spacing between the seedlings was such that they had begun to encroach on one another in the second growing season after planting (2018), thus, reliable estimates of seedlings' sizes for a third year is very unlikely. As common garden studies of seedlings are often conducted for time periods that extend well beyond two years, we recommend that the spacing between seedlings be increased to extend the duration of useful UAS survey data. For example, in plantations where seedlings are spaced more than 0.5 meters apart and individuals are protected by planting containers (Gil-Docampo et al., 2020), we would expect that it would be possible to survey the seedling sizes using our methods for at least three years. To determine an adequate spacing, researchers should take into consideration the geometry of the plant as it matures (i.e., size and shape) to anticipate the space that the individuals will occupy. Alternatives to increased spacing include the installment of physical barriers between the plants, as well as thinning

treatments to create space between them, though the latter option has implications for the overall study design and sample sizes.

The sizes of the seedlings also affected our ability to detect them accurately. In particular, the seedlings were too small for reliable height estimates from the data in the first year, which is not only obvious by visually inspecting the point clouds (Figure 2-1), but is also reflected in the correlations between the remotely sensed height estimates and the ground height measurements across 2017 and 2018 (Figure 2-7). Unfortunately, larger seedlings also have larger crowns, which makes them more susceptible to wind. The 2018-point cloud had much lower point density than 2017, which resulted in lesser ground point density. This could be due to a combination of two factors, the first being the larger seedling crowns and complex geometry, and the second being that there was a gentle wind during the data collection which caused the seedlings to sway.

We found that the main limiting factor with regards to size estimates of seedlings from photogrammetric point cloud is the smoothing of the crown, which occurs during the SfM reconstruction process (i.e., texture is lost). Although the spacing of the points in the clouds was small, the seedlings rendered less details in 3D compared to the high resolution 2D orthophotos. The most obvious difference in the absence of important details is that no leaves are visible in the point cloud data (Figure 2-1), whereas some leaves are clearly detectable in the 2017 (Figure 2-5).

Also, we found that the presence of weeds and foreign objects in the boxes encumbered our methods. The weeds that were growing along the north edges of both boxes in 2017 (Figure 2-5) interfered with the vegetation masking process, which resulted in the omission of five seedlings, highlighting the importance of weed management in such studies. There was also twine in the boxes that was arranged in a grid pattern between the seedlings. For the vegetation masking procedure, we accounted for the twine by creating a separate training category (Figure 2-5). However, although the twine was near the ground level, it appeared above ground in the 3D reconstruction (Figures 2-1 and 2-2 and 2-4). Nevertheless, the twine was easily visible in the imagery and was helpful for confirming the seedling locations within the boxes so we could combine the remotely sensed estimates with the ground data. Overall, however, we

believe that it may be possible to automate seedling detection, and that the drawbacks of distortions in the 3D data outweigh the benefits of having the twine present in the boxes. As a result, we do not recommend including any foreign materials inside common garden boxes that will be surveyed with UAS.

In the field, it takes about 10 seconds to measure the height or diameter of a seedling on the ground and another 10 seconds to record the data. Though there were only 150 seedlings in this study, it would take about 75 minutes to measure them by hand, whereas the UAS flights took under 5 minutes to conduct. Nevertheless, the total time spent initializing and finalizing data collected with UAV was more than two hours, but in roughly the same amount of time it would have been feasible to survey dozens of additional boxes, had they been located alongside one another. However, the time it takes to measure additional boxes by hand increases linearly according to the number of seedlings, while the time to survey them with UAS increases according to the number of boxes. As a result, the methods we present here have the potential to reduce the number of hours and monetary costs of common garden experiments containing conifer seedlings. The most time-consuming part of our procedure was the manual identification of seedling crowns, which was necessary for comparison in this study, but much more easily accomplished via the masking procedure. Assuming that the creation of circular vectors is unnecessary, we estimate the extraction of seedling size estimates for our sample took about 2 hours each year and that the time requirements would increase by 15 minutes per additional box of seedlings (~75 individuals). As a result, we estimate it would take approximately the same amount of time (~4 hours) to record 750 seedling sizes manually (10 boxes) or to estimate their sizes using our methods. For 1800 seedlings (24 boxes), we estimate it would take 25% less time (i.e., 7.5 hours versus 10 hours) to estimate the seedlings sizes from the UAS compared to manually measure them.

Using the point clouds to identify the top of the seedlings with efficient segmentation algorithms would not only automate the process of drawing plant centers, but can also be used to estimate heights and crown diameters (Karttinen et al., 2012b; Panagiotidis et al., 2017). Future studies may focus on the automatic detection of seedlings in tightly spaced arrangements such as common gardens as others have

with open grown seedlings (Feduck et al., 2018; Fromm et al., 2019). In the case of common garden studies, though, it is necessary to link the seedlings in the imagery to other data besides the remotely sensed estimates, which requires a validation step that would be difficult to automate. The time spent to describe the seedlings with point clouds and orthophotos is valuable, as they capture an image of the seedling at a point in time, which can be used for subsequent studies, whereas manual measurements are confined to their origination study. Therefore, the future utility of the remotely sensed products is an aspect that should be considered when UAS are used in seedling monitoring.

The extraction of zonal statistics (i.e., the maxima and minima within the plant crowns) was the most computationally demanding part of our procedure and represents a potential processing bottleneck if the procedure is to be scaled up. A possible solution consists in transcription of the procedure from R into Python, which can interface with both QGIS and Agisoft SfM software, further automating the process. Given the opportunities that exist to improve the presented workflow, we believe that UAS structural measurements have a logistical advantage when compared to ground-based measurements of tree seedlings in common gardens.

## 2.4.2. Modeling

The nonparametric Boruta procedure does not produce estimates of fit, but it does rank the predictors in terms of importance relative to the shadow variables, rather than omitting those deemed as unimportant. As a result, it gives the user an idea of which variables were least important or marginal. We found it to be a useful tool for prioritizing the variables before modeling them. We found that the most suitable variable for predicting seedling size is LA, followed by height, DRC, and slenderness. If the models are ordered according to the  $R^2$ , there are no overlapping values between the four response variables we tested (Table 4), which suggests that the choice of response variable influences the predictability of seedling size. Including the remotely sensed variables increased the predictive power of the models compared to using only the measurements from the previous year for all four response variables we tested, as  $R^2$  values increased at least 0.04 (i.e., 0.07 for height, 0.04 for RCD, 0.09 for slenderness, and 0.05 for LA). Also, the model precision improved at least 6% in terms of RMSE (i.e., 12% for height,

6% for DRC, 8% for slenderness, and 12% for LA) when remote sensed derived variables are included. Finally, the method used to compute the seedling height seems to play an important role, as the size estimates using the vegetation mask, namely  $Height_{Mask}$ ,  $Area_{Mask}$ , and  $Volume_{Mask}$ , exhibited larger correlations with the ground based estimates than with the estimates from the DTM. The influence of methodology can partly be attributed to the conical shape of the seedling crown, especially in the second year, and the decrease in crown spacing with time. This distortion results in the location of the ground points between the plants in the cloud being located above the true position of the ground in the box, which causes anomalies in the DTM where the plants are located. As a result, the elevations around the plants in the DTM are raised, which causes the seedling height to be underestimated. When the distorted DTM elevations are used to produce a normalized cloud such as our CHM, the underestimates are worsened due to the lowering of the tops of the plants during the normalization process. Thus, by forgoing the ground detection process and using a detailed vegetation mask to differentiate the locations of plants from their surroundings, we were able to extract more reliable size estimates directly from the DEM.

Despite the UAS size estimates having low predictive power on their own, we presented evidence that remote sensed estimates of size can improve size prediction when combined with ground measurements. Incorporation of UAS surveys in small scale common garden experiments result in extending the number of seasons that a project can afford to collect data or used to develop a two-phase sampling procedure (i.e., double sampling) to reduce the number of ground measurements.

The only seedling that was misclassified as living (i.e., was actually dead) had only 3 pixels classified as vegetation, which may have been a small weed rather than the seedling itself. Therefore, we provided evidence that UAS can be used successfully to identify seedling mortality, or, more specifically, to record the absence of seedlings in the vegetation mask from the second year compared to the first. In some common gardens, plant success is measured on a living or dead basis, which we show can be accomplished by monitoring the seedlings using UAS.

The effort placed in development of spectral variables to be use as predictors was not rewarded, as we could not justify including any spectral variables (i.e., vegetation indices) when modeling seedling size. Therefore, we infer that in absence of multiple repeated measurements dimensionless variables, such as spectral variables, are less effective predictors of seedling size than the remotely sensed dimensional measurements. However, the near-infrared and red-edge bands of the sensor we used, which differentiate it from most consumer-grade cameras, were needed to create the indices needed to create the vegetation mask, which was important for improving the quality of size estimates made from the UAS imagery.

## 2.5. Conclusions

We found that there are several challenges that emerge when using UAS to produce photogrammetric point clouds to estimate seedling size in common gardens. First, the scaling error in the vertical plane was several times greater than in the horizontal plane (1.1 - 1.8 cm versus 4.7 - 5.1 cm), which results in systematic errors across the point cloud in terms of measuring heights. In addition, the lack of ground points makes the generation of DTM inaccurate such that the interpolated ground elevation is positioned above the actual ground elevation. The classification of non-ground points as ground underestimates the seedlings height irrespective of the method of computing the height. Therefore, we found evidence that the height of seedlings estimated from DTM is unreliable. Finally, the lack of spacing between seedlings results in crown overlap, which makes delineation of individual seedlings from the multispectral orthophotos difficult with time. As seedlings grow, the increased crown size reduces the ability to capture the ground with passive sensors, which decreases the accuracy of ground estimation and, consequently, directly alters the estimation of the seedling height. Based on this study, we can recommend that seedlings be spaced at least 15 cm apart at planting to extend time that UAS can be used to survey the seedlings from two years in this study to at least four years.

We also found that seedling size estimates from UAS can be improve the size models based on previously measured dimensions. The inclusion of remotely sensed estimates not only that increases the precision but also presents a series of operational benefits. For example, using UAS reduces the number

of manual measurements needed in the study, which will reduce the time and diminish the costs needed to acquire the data. An advantage of acquiring data with UAS is consistency, as human error (e.g. the expertise or fatigue of the human taking the measurements) does not play a significant role in the quality of measurements. Importantly, automation of the seedling identification process would ensure the transferability of the method across regions (i.e., space) and likely to plantations (i.e., scale). One of the major advantages of using UAS in the context of common gardens is that they have the potential to be much faster than traditional, manual measurements. While our methods were not perfect, we estimate that if the number of seedlings were about one order of magnitude higher, (i.e.,  $n=1800$ ) the total combined time of UAS field surveys, post-processing, and data extraction would be 25% less than the time required to record seedling sizes on the ground.

The size metrics we used as response variables in this study (i.e., height and DRC) are not the only metrics commonly used to describe seedling sizes. Notably, aboveground biomass has been identified as a strong predictor of conifer seedling growth (Norgren, 1996), and has been estimated using images captured from a stationary platform above conifer seedlings (Ter-Mikaelian and Parker, 2000). Measuring seedling biomass often requires destructive sampling (i.e., drying and weighing of seedlings), therefore, it would be useful to test the ability to estimate biomass from UAS imagery. We recommend that this should be tested using similar methods to those presented here, specifically, using a vegetation mask and DEM to estimate seedling volume.

Our method presented a workflow for accurate detection of seedling mortality using UAS. Furthermore, we contend that this methodology can be applied not only on common gardens but also in regeneration surveys, which would be another natural extension of this research.

### 3. Assessing Lean and Positional Error of Individual Mature Douglas-Firs (*P. menziesii*) with Active and Passive Sensors

## Abstract:

There is a growing demand for point cloud data that can produce reliable single tree measurements. The most common platforms for obtaining such data are: UAS with passive sensors (UAS), UAS with aerial lidar scanners (ALS), and mobile lidar scanners (MLS). Our objectives were to compare these platforms' capabilities to locate treetops and stems, and to estimate tree lean. The platforms were used to produce overlapping point clouds of a mature Douglas-Fir stand, then 273 trees were manually identified from the combined data. Control trees were used to test tree detection accuracy of four algorithms and the number of stems detectable using each platform. Tree lean was calculated in two ways: using the stem location near the canopy and using the treetop. The treetops were detected more accurately from ALS and UAS clouds than from MLS, but the MLS outperformed ALS and UAS in stem detection. The platform influenced treetop detection accuracy, whereas the algorithms did not. The height estimates from the ALS and MLS were correlated ( $R^2=0.96$ ), but the MLS height estimates were unreliable, especially as distance from the scanner increased. The lean estimates using the stem locations or treetop locations produced analogous distributions but were weakly correlated overall.

### 3.1. Introduction

Digital three-dimensional reconstructions of forests with point clouds have been used to measure individual trees for more than twenty years, (Hyypä, 1999; Hyypä et al., 2001), (Brandtberg, 1999; Ziegler et al., 2000). Point clouds describing trees can be created in two fundamentally different ways: by using active sensor technology, i.e., light detection and ranging (lidar), or by using digital reconstructions of passive sensor imagery through algorithms, namely structure from motion (SfM) (Tomasi and Kanade, 1992; M.J. Westoby et al., 2012). Because lidar is inherently a direct ranging technology, it has the capability of producing point clouds with high local spatial accuracy (Sofonia et al., 2019). However, lidar data collections are limited by cost and complexity of implementation. These limitations are more evident when comparing lidar products to the products of SfM reconstructions of passive sensor imagery, namely digital elevation models (DEMs), and canopy height models (CHMs). Compared to manned aircraft, sensors installed on unmanned vehicles can achieve greater spatial resolution due to their ability to acquire data at lower altitudes. As the technology has become more sophisticated, unmanned vehicles have also become more portable and less expensive. The term unmanned aircraft system (UAS) describes the combination of a unmanned aerial vehicle and a ground control system which allow for systematic coverage of large areas and georeferencing of data (Lisein et al., 2013). In general, flight missions with UAS can be conducted more regularly than with manned aircraft due to fewer logistical, financial, and weather constraints. This has led to a broad range of new UAS-enabled scientific inquiry, including for forestry (Gambella et al., 2016).

The use of UAS based SfM photogrammetry, subsequently referred to as UAS, to create point cloud data of forested scenes dates back to 2011, though the resolution was too poor to extract single tree measurements at the time (Tao et al., 2011). Around the same time, the first lidar-enabled UAS were tested in a forestry context (Jaakkola et al., 2010). Ensuing studies demonstrated the value of UAS based lidar sensors, subsequently referred as ALS, compared to manned aircraft for single tree inferences due to increased point density (Lin et al., 2010) and developed UAS hardware and software deliberately to

facilitate forest inventory (L. Wallace et al., 2012). Currently, ALS configurations can produce point clouds that can be used to measure forest structure both independently and alongside UAS data (Wallace et al., 2016). Studies that have compared tree height estimates using both UAS and ALS, revealed that SfM values are smaller than lidar values (Swinfield et al., 2019; Wallace et al., 2016). This underestimation is likely related in part to smoothing of the canopy surface due to the SfM reconstruction process (Lisein et al., 2013).

Mobile terrestrial lidar scanners (MLS, mobile lidar) share many fundamental components with UAS-lidar, such as GNSS receivers, inertial measurement units (IMUs), and a lidar sensor that creates point cloud data. The process used to georeference lidar pulses is also fundamentally similar. The main difference is simple and important: the lidar system for MLS is located on a vehicle that moves along the ground rather than through the air. Typically, UAS-based point clouds are constructed from a top-down vantage point, where the MLS point clouds present a profile view of the tree stems. There is one notable exception in the work by Chisholm et al. (2013), who developed UAS for below-canopy use. In forest research, MLS have been developed using sensors that are handheld (Bauwens et al., 2016), as well as those mounted on an all-terrain vehicles (Tang et al., 2015), and passenger vehicles (Holopainen et al., 2013). Holopainen et al. (2013) combined MLS and aerial data and observed that both platforms are subject to obscuration of portions of the tree. In ground-based scans, understory vegetation and lower branches shield treetops, and in aerial scans, the crowns shield tree stems.

Tree level measurements from point clouds require identification of individual trees within the point cloud. Algorithms that delineate trees inside the point clouds are collectively known as individual tree detection and extraction (ITDE) algorithms (Kaartinen et al., 2012a). Many ITDE algorithms involve creating a CHM raster from the cloud, then using a moving-window operation to locate the local maxima (Dalponte and Coomes, 2016; Meyer and Beucher, 1990a; Silva et al., 2016). The spatial resolution of the CHM and the size of the moving window, or local maxima filter, are required inputs for segmentation based on rasters (i.e., gridded data). Coniferous tree crowns typically demonstrate excurrent branch growth and have one characteristic top, making them more suitable in general for this

sort of procedure than deciduous tree crowns, whose tops can be difficult to locate (Miller, 2015; Zaforemska et al., 2019). Other IDTE algorithms work by segmenting trees directly from the point cloud data and do not require CHM rasters as inputs (Hamraz et al., 2017; Li et al., 2012).

Tree leaning, which is defined as the departure of a tree stem from a vertically upright position, is a major source of error when estimating the heights of individual trees from airborne lidar data (Gatziolis et al., 2010a). Trees that lean have also been reported to be more likely to be a source of error for ITDE algorithms (Zaforemska et al., 2019). Leaning trees are prone to positional errors, as the main stem would likely not be located directly under the top of the tree. Accurate tree position from ALS data is needed if accurate location of the stem is required when below canopy data is not available (Strimbu et al., 2019). Therefore, objectives of this study are twofold: first, to compare the ability of the UAS, ALS, and MLS platforms to position tree stem from the treetops estimated from point clouds, and second, to estimate the tree lean from the ALS acquired data. To carry out these tasks we tested several different ITDE algorithms and point cloud densities to assess the impact of the algorithm on positioning error.

## 3.2. Methods

### 3.2.1. Field Site

The study was conducted on a small (~4 ha) stand within Oregon State University's McDonald-Dunn Research Forest, located roughly 6 miles north of Corvallis, Oregon, USA. The stand has been managed as a Douglas fir (*Pseudotsuga menziesii*) shelterwood that was planted in 1953 and thinned in 1986. We selected this location for its suitability to attain the objectives of the study. First, it is located on a road that follows a ridge, which allows for good GNSS satellite visibility, relative to other locations within the forest. Furthermore, the thinning produced a relatively open understory, which combined with a minute surface relief along the road, ensured that the MLS scans would penetrate well into the stand and register points along the entire tree stems. Finally, there was a clearing along the road that met the requirements for a UAS takeoff and landing zone. The data from all platforms were acquired in February

and March of 2018 within a 25-day period in the winter, so tree growth was assumed to be negligible during this time.

### 3.2.2. Platforms

The hardware comprising the three remote sensing platforms used in the study are listed in Table 1. At around \$6000, the UAS costs the least by a large margin. However, there were some necessary modifications to prepare the platform for our study. The factory gimbal was removed from the airframe and retrofitted with a 3D-printed mounting bracket for the multispectral sensor. The 3DR solo comes stock with both a GNSS receiver (UBLOX Neo m7n, Thalwil, SWI) and autopilot (Pixhawk 2) to calculate its orientation and position in flight.

Table 3-1: Characteristics of the three UAS platforms used to create overlapping point cloud reconstructions of a small Douglas-Fir shelterwood stand in the MacDonald Forest near Corvallis, Oregon.

<b>Platform</b>	<b>Vehicle</b>	<b>Sensor</b>	<b>Cost</b>	<b>Position</b>
UAS	3DR Solo Quadcopter	Micasense Rededge Multispectral	\$6,500	Airborne
ALS	DJI S1000 Octocopter	Velodyne Puck Lidar	\$30,000	Airborne
MLS	Toyota Tacoma	Velodyne HDL-64E Lidar	\$400,000	Ground

The ALS platform costs roughly five times as much as the UAS platform in terms of hardware alone, but this does not account for in excess of 100 hours of assembly, fabrication, programming, testing, and other engineering tasks that were required to ready the platform for use. Unlike the 3DR solo, the DJI S1000 requires assembly. The ALS is substantially larger (1 m vs. 0.3 m diameter) and heavier (10 kg vs 1.6 kg) than the UAS, making it more cumbersome to transport. Also, where the UAS platform required only one additional part to mount the sensor to the airframe, the ALS required many custom printed parts to mount the sensor, GNSS receivers, and the GNSS-aided inertial measurement unit (IMU) (OxTS XNAV200, Oxfordshire, UK).

The MLS, which was by far the most expensive platform, was originally purchased by the Oregon Department of Transportation (ODOT) for asset inventory, bridge/overhead structure clearance, and other uses, then granted to Oregon State University in exchange for research in 2015. We followed in-house standard operating procedures for operation of the MLS, and no modifications were necessary to prepare the platform for use. The MLS contains a GNSS-aided INS (Topcon IP-S2 HD, Tokyo, JAP) as well as a distance measurement indicator. Because tree form varies near roads (Bowering et al., 2006a), and the MLS in this study was on a pickup truck, we expected this edge effect to be present in our data.

### 3.2.3. Data Collection and Processing

The data acquisition procedures for the platforms were very different. In the case of the UAS, the multispectral sensor is sensitive to lighting conditions, which are affected by weather and time of day. As a result, the platform had to be deployed near solar noon on a clear day. To account for changes in illumination during the flight, we used images of a calibration target from before and after the data collection for radiometric correction (i.e., conversion to reflectance). On 10 February 2018, the Tower Drone Control App (3DR, Berkeley, USA) was used to pilot the aircraft using a grid mission plan traveling 4 m/s at 80 meters above ground. The sensor was programmed to trigger once every 1.5 seconds, such that adjacent images would have 50% overlap and 50% side-lap. Due to the visual obstruction created by the trees, a visual observer was needed in addition to the UAS pilot to follow the aircraft during the mission. The entire data collection for the UAS took less than 2 hours, with only 14 minutes of flight time.

The MLS data were collected on 5 March 2018. The onboard computer requires 5-minute initialization and shutdown periods, during which the vehicle must be stationary. Once this was completed, the lidar scanner data were collected as the truck moved down the road at a low, constant speed (5 m/s). Although the platform can perform well at higher velocities in urban settings, forest roads are much less smooth and natural scenes are relatively much more geometrically complex, so we elected

to scan slowly in this case. Including the initialization and shutdown, the entire data collection for MLS took around 15 minutes.

The ALS data were the most challenging to obtain. We piloted the aircraft using a first-person viewing camera and a visual observer to make passes across the AOI on 9 February 2018. Overall, we found that conducting missions with this platform was more difficult than with either of the other platforms. Take-off and landing of the ALS require a skilled pilot, as the platform is larger and heavier than the UAS, making it more cumbersome in the air. The data collection for ALS took about 3 hours, during which we conducted 3 redundant flight missions, one of which was used for our analysis.

There were 244 images taken from the UAS, which had to be radiometrically corrected using the values from images of a calibration target, then reconstructed in 3D using structure from motion (SfM) (M.J. Westoby et al., 2012). We used Agisoft Photoscan Professional v.1.4.0, which implements SfM to create photogrammetric point clouds and orthophotos. The workflow we used followed the recommendations of Rossi et al. (2012) and Turner et al. (2013), including using the highest justifiable settings for the reconstruction. For photo alignment, we used the image unaltered (i.e., the “highest” accuracy setting), with 120k key points and 30k tie points. For building the dense point cloud, we also used the original images (i.e., the “ultra-high” quality setting) and we filtered the depth outliers by assuming that no meaningful small details are present (i.e., the “aggressive” depth filtering). The dense point cloud was used to create a mesh layer using the original images (i.e., “ultra-high” depth maps quality setting), and from the mesh we created both a digital elevation model (DEM) and a multiband orthophoto.

For post-processing the UAS-L scan, the GNSS and INS data were integrated to produce a trajectory estimate for the platform using OxTS’s NAVsuite software. Then, the lidar scan data, platform dimensions, and trajectory were used to produce a georeferenced point cloud using in-house MATLAB scripts (MATLAB, 2010)

### 3.2.4. Coregistration and Outlier Removal

To spatially align the point clouds with one another, a process known as coregistration, we used a two-step approach. First, we eliminated the outliers and visually aligned the UAS or MLS point clouds with the ALS point cloud. Second, we aligned the point clouds using the iterative closest point (ICP) algorithm (Besl and McKay, 1992). Initially, the clouds were too far apart to use an automatic coregistration procedure, so we first visually positioned both the UAS and MLS data to match the location of the ALS point cloud. The ALS cloud was chosen as the reference layer because it was the only platform that captured both the tree tops and the tree stems in detail, as the UAS imagery were taken from an overhead perspective, obscuring the stems, and the MLS laser scans were captured from the forest road, obscuring the tree tops (Figure 3-1). After coregistration, we established a rectangular area of interest (AOI) that extended 50 meters on both sides of the road for the length of the MLS scan (total area 2.7 ha) and buffered the entire plot by 10 meters on all sides.

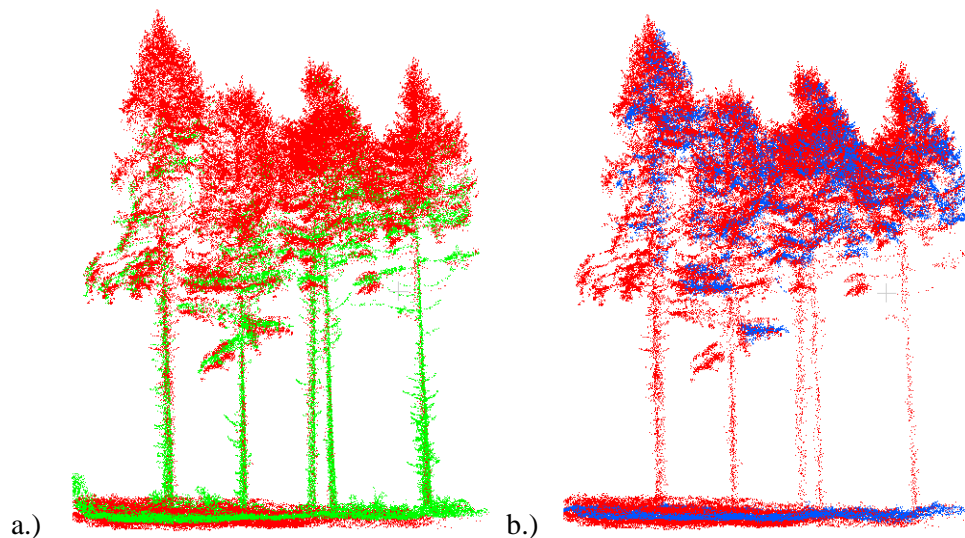


Figure 3-1: Alignment of point clouds following coregistration, where the ALS data (red) were used as the reference points to align both the MLS (a.) (green) and UAS (b.) (blue) data. The mean (standard deviation) cloud-to-cloud distances compared to the ALS data were 0.59 m (1.18m) and 0.64 m (1.04m) for UAS and MLS, respectively.

We eliminated all the points considered outliers by the 50-nearest neighbor algorithm (Cover and Hart, 1967), implemented in the point data abstraction library (PDAL) (PDAL Contributors, 2018).

Following the removal of outlier points, we used the iterative closest point (ICP) algorithm (Besl and McKay, 1992) to coregister the UAS and MLS point clouds to the ALS cloud similarly to Henning and Radtke (2006). The ICP coregistration resulted in mean cloud-to-cloud distances (standard deviations) of 0.59 m (1.18m) for UAS and 0.64 m (1.04m) for MLS, respectively. The coarse and fine coregistrations were performed using CloudCompare (Girardeau-Montaut, 2015). Point cloud summary statistics for all platforms following post processing are shown in Table 2.

To assess the impact of point cloud density on the tree lean and position, we decimated the UAS and ALS clouds from full resolution to lower resolutions, specifically 100 points/m<sup>2</sup> and 10 points/m<sup>2</sup>. The decimation consisted of randomly sampling points to achieve the desired overall resolution. We did not decimate the MLS cloud, because tree segmentation from the mobile ground scanner was unreliable, as discussed later in section 3.1.

Table 3-2: Point cloud summary statistics for each platform following our post processing procedures.

<b>Platform</b>	<b>Points (millions)</b>	<b>Density (pts/m<sup>2</sup>)</b>	<b>90%ile Elevation</b>	<b>95%ile Elevation</b>	<b>Max Elevation (m)</b>
ALS	24.62	465.73	39.95	41.55	49.74
MLS	81.23	1584.67	24.93	28.93	47.15
UAS	21.03	407.32	37.93	39.61	54.79

### 3.2.5. Individual Tree Detection and Extraction

To classify the ground points from the clouds, we initially tested two algorithms: the cloth simulation filter (Zhang et al., 2016) and the progressive morphological filter (Zhang et al., 2003). Both algorithms produced similar results, therefore we have chosen the cloth simulation filter for ground classification. We normalized the point clouds (i.e., removed the topography by subtracting the ground

elevation from the point elevation) using the digital terrain models (DTM) produced by each platform **(Error! Reference source not found.)**.

Seed points (i.e., input for the raster based ITDE algorithms) were identified from the normalized point clouds using a local maxima filter with a fixed 5 meter window size and a minimum tree height of 15 meters (Popescu and Wynne, 2004).

To create the control, we used all available data to produce a point vector layer displaying the the locations (easting, northing) of each tree, for which we used the visual centers of tree crowns from above as a proxy. In addition to the point clouds, we used the CHM layers (Figure 3-3) from all three platforms and the SfM orthomosaic raster which resulted from the reconstruction of UAS imagery. Some trees in the scene which were along the border of our study area were only partially present in one or more of the clouds, and therefore were omitted. We were able to identify 263 control trees in total. We also created a road vector by drawing a line down the visual center of the roadway, then computed the minimum distance to the road from all seed and reference points using QGIS (QGIS Development Team 2015).

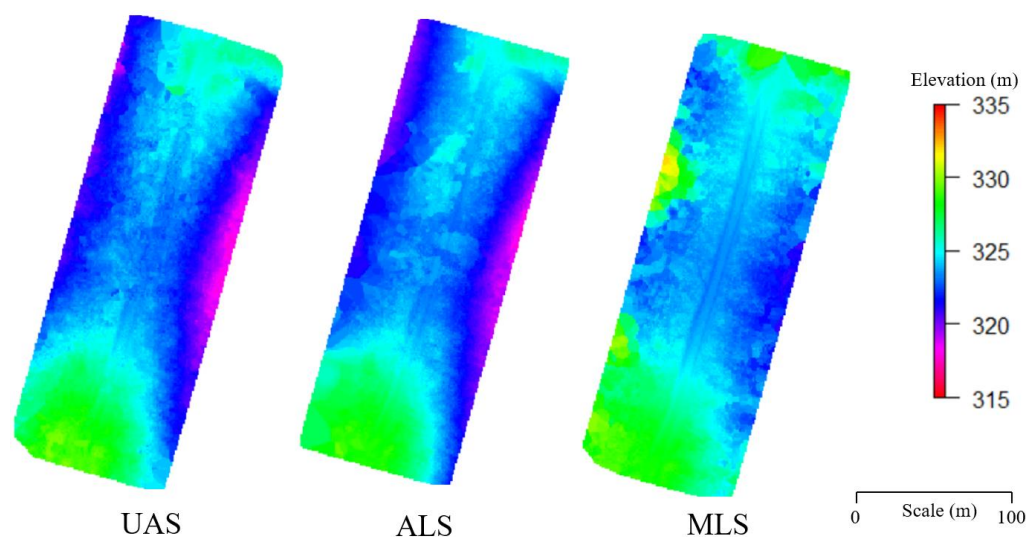


Figure 3-2: Digital terrain models from the UAS photogrammetric point cloud (UAS), the airborne lidar scanner (ALS), and the mobile lidar scanner (MLS).

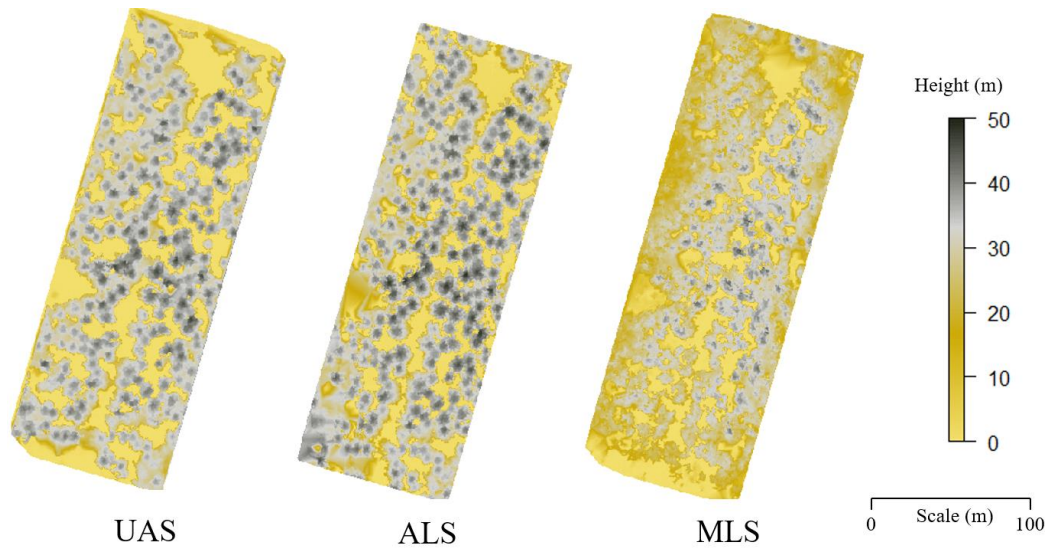


Figure 3-3: Canopy height models from the UAS photogrammetric point cloud (UAS), the airborne lidar scanner (ALS), and the mobile lidar scanner (MLS).

We tested four ITDE algorithms for each platform, covering both types of tree extraction algorithms according to Kaartinen et al. (2012), namely 2D and 3D. In the 2D category, we tested three algorithms, which require seed points and CHM as inputs. The first is a region growing algorithm that designates seed points as tree tops, then uses a decision tree method to grow individual crowns around the seed points ("D") (Dalponte and Coomes 2016). The second algorithm applies a variable radius crown buffer to delimit the tree crowns initially, then uses a centroidal Voronoi tessellation approach to isolate the tree polygons from one another ("S") (Silva et al. 2016). The third algorithm we tested was marker-controlled watershed, a specific implementation of the watershed algorithm ("W") (Meyer and Beucher 1990), which is a morphological transformation that treats inverted tree crowns as regional basins which are subjected to a simulated flooding scenario in order to derive crown boundaries. The fourth algorithm, unlike the other three, falls into the 3D category, meaning it worked directly on the point cloud. Specifically, it uses top-down region growing method ("L") (Li et al. 2012). The tree segmentation, including local maxima filtering and algorithm implementation, was carried out in R (R Core Team, 2017) using the 'lidR' package (Roussel and Auty, 2019). Once the tree segmentation

procedures were complete, the locations of the treetops (i.e., x, y, height above ground) were extracted for each segmented tree crown.

### 3.2.6. Stem Locations

To locate the base of the trees in the point clouds, we sliced the normalized clouds horizontally from 1 to 2 meters above ground. This was not possible for any trees using the UAS data due to the general absence of stem points in the 3D reconstruction. For the MLS data only, we created a second slice near the base of the crowns, from 18-19 meters above ground. We chose the location of the upper slice by finding the highest section where we could still detect the stems for the most trees by trial and error. The sliced clouds were rasterized from a nadir perspective at 5cm resolution, then manually located the centers of the stems by fitting circles over each, then placing point vectors in the center of the circles using QGIS (QGIS Development Team, 2015) (Figure 3-4).

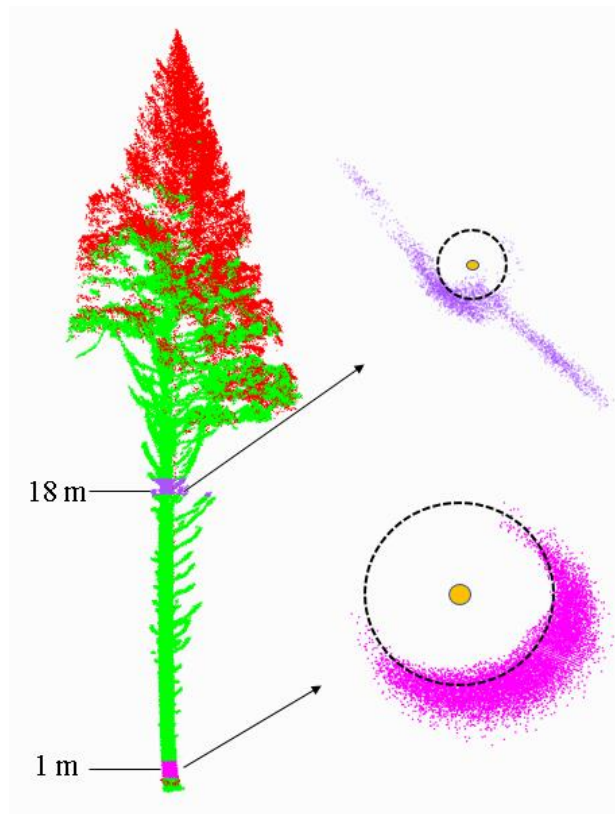


Figure 3-4: Horizontal slices of point clouds from 1 to 2 meters (pink) and 18-19 meters (purple) above ground (purple) were created by subsampling the raw point cloud data parallel to the ground (left) and used to visually locate the stem center points (yellow) from above (right) for MLS (green) and ALS (red) platforms.

### 3.2.7. Detection Accuracy and Positional Error

To test the accuracy of the ITDE algorithms with respect to the control, we created circular buffers (3 m radius) which were slightly smaller than half the minimum distance between any two control points (6.12 m) and computed the accuracy (control trees detected), omission error (control trees missed), commission error (false positive tree detections), bias ( $\mu$ ), and root mean squared error (RMSE) for each combination of platform and algorithm (12 in total).

We performed an identical procedure to evaluate stem detection. In this case, we looked for stem center locations from the MLS and ALS clouds within 3 meters of our control points and computed the detection accuracy, omission and commission,  $\mu$ , and RMSE.

Finally, we used 3 meter buffers around the MLS stems to assess the positional error of the treetop locations. The buffer size was chosen to ensure the presence of only one treetop per stem (conincidentally it was the same as in the other comparisons). Because all of the stems that were located from the ALS data ( $n=210$ ) fell within 1.5 meters of a stem located in the MLS data ( $\mu = 0.61$  m , RMSE = 0.68 m), and because more stems overall were detectable from the MLS ( $n=273$ ), the MLS stems were used as reference.

### 3.2.8. Height and Lean Assessment

We compared the height estimates of all of the trees where detection overlapped in all three point clouds ( $n = 153$ ) by constructing scatterplots for the three pairwise combinations of platforms. To display the comparisons, we constructed scatterplots using the package ‘ggplot2’ in R (Wickham, 2016). We performed linear regressions over each, and incorporated the tree distance from the road in these plots for visualization purposes.

Given the flexibility of the tree and the phototropic character of terrestrial vegetation, tree lean is most relevant from an operational perspective if it occurs on the lower portion of the stem as opposed to in the crown. Therefore, we have computed the lean as the horizontal distance (euclidian distance)

between the centers of the stem at 18 m and at 1 m as measured from the MLS ( $D_{\text{stem}}$ ). However, tree lean has been also formally been described using the horizontal displacement between the stems and tree tops, so we performed a second lean calculation using the distance between the stem locations at 1 meter measured from the MLS and the location of the treetop measured from each of the aerial platforms ( $D_{\text{top}}$ ) (Figure 3-5).

For both the stem centers at 18 m and for the treetop points we calculated the lean angle ( $\theta$ , °) as follows:

$$(1) \quad \theta = \left(\frac{180^\circ}{\pi}\right) \tan^{-1}\left(\frac{D}{h}\right)$$

where  $D$  is the lean distance ( $D_{\text{stem}}$  or  $D_{\text{top}}$ ), and  $h$  is equal to the height where the distance was measured minus one. Then we used the coordinates of the base of the stem ( $x_{\text{base}}$ ,  $y_{\text{base}}$ ) and of the upper positions ( $x_{\text{top}}$ ,  $y_{\text{top}}$ ) to calculate the azimuth (directionality) of the lean, measured in degrees clockwise from north, as follows, computed using the `atan2()` function:

$$(2) \quad azimuth = \left(\frac{180^\circ}{\pi}\right) \tan^{-1}\left(\frac{y_{\text{top}} - y_{\text{base}}}{x_{\text{top}} - x_{\text{base}}}\right).$$

To visually compare the results of the lean estimates, we created two maps: one to show the lean,  $\theta$ , and azimuth,  $\alpha$ , for each tree based on the  $D_{\text{stem}}$  and another to based on  $D_{\text{top}}$  estimated from the ALS. We also created histograms to show the distributions of the  $\theta$  based on  $D_{\text{stem}}$  and on  $D_{\text{top}}$ . Using these histograms and the work of Thies et al. (2004), who purported that trees with less than 1.8 cm lean per meter of stem are non-leaning, we considered that the stem is leaning if  $D_{\text{stem}} > 0.34$  m, which corresponds to  $\theta > 1.15^\circ$ . We used this threshold to rate each tree as leaning or non-leaning, then created another pair of histograms to show the distributions of lean azimuth for trees that were leaning (i.e., had  $\theta > 1.15^\circ$ ). All histograms were created using the R package “ggplot2” (Wickham, 2016).

Tree height, as well as tree lean ( $\theta$ ,  $\alpha$ ) were calculated using the locations of the treetops from the decimated ALS and UAS data (100 and 10 pts/m<sup>2</sup>) in addition to the full resolution clouds. We

ranked the observations based on the mean values across platforms and resolutions from smallest to largest, then used this variable to order the data in scatterplots.

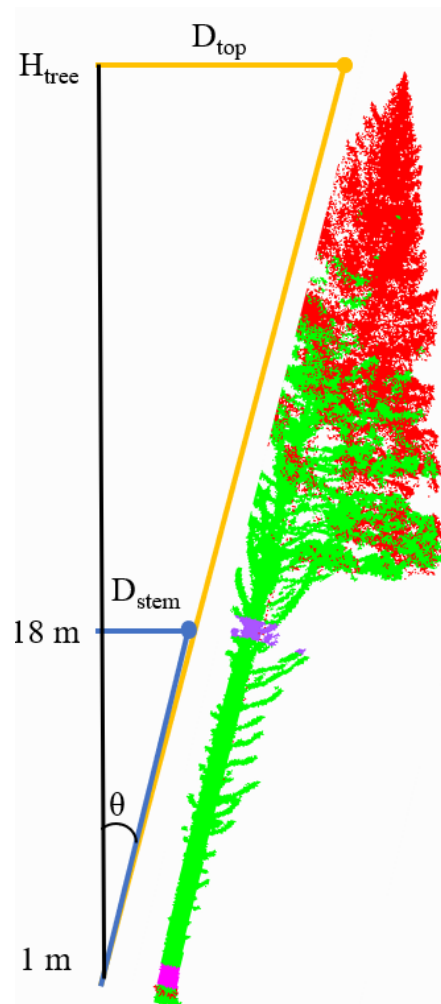


Figure 3-5: Schematic showing how we used the location of each tree stem at 1m measured from the MLS platform (green) to estimate the tree lean angle ( $\theta$ ) using either the horizontal distance to the stem center at 18m ( $D_{\text{stem}}$ ) or the horizontal distance to the treetop ( $D_{\text{top}}$ ) and the estimated tree height ( $H_{\text{tree}}$ ). The tree has been trimmed and shifted slightly to the right in the image for clarity, and the lean angle is exxagerated.

### 3.3. Results

#### 3.3.1. Detection Accuracy and Positional Error

Comparisons between the locations of the manually identified tree centers and the treetop points revealed that overall both aerial platforms, ALS and UAS, were more accurate in terms of detecting the

trees (91-97% for ALS and 87-94% for UAS) than the ground-based MLS (72-77%) ( Table 3 ). In addition to decreased accuracy, tree segmentation of the MLS cloud resulted in substantially greater commission error (7-14%) than the other two platforms (2-7% for ALS and 1-7% for UAS). The overall  $\mu$  and RMSE were below one meter and comparable for all algorithms using the ALS ( $\mu = 0.65$ - $0.70$ m, RMSE =  $0.82$ - $0.91$ m) or UAS ( $\mu = 0.60$ - $0.66$ m, RMSE =  $0.72$ - $0.84$ m ), and almost double using the MLS ( $\mu = 1.41$ - $1.45$ m, RMSE =  $1.61$ - $1.64$ m). Therefore, the aerial platforms were less biased and more precise than the MLS in terms of locating the treetops.

Table 3-3: Tree detection accuracy using the visually detected tree centers (n=263) as the reference points and the local vertical maxima within crowns segmented using each combination of the three platforms and four segmentation algorithms that we tested.

Platform	Algorithm	Trees	Omission	Commission	$\mu$ (m)	RMSE
		Detected	Error	Error		(m)
ALS	D	93.54%	6.46%	6.84%	0.70	0.91
ALS	S	93.92%	6.08%	5.73%	0.68	0.88
ALS	W	96.58%	3.42%	5.22%	0.65	0.82
ALS	L	90.87%	9.13%	1.65%	0.68	0.87
MLS	D	72.24%	27.76%	12.04%	1.43	1.62
MLS	S	73.00%	27.00%	13.12%	1.43	1.61
MLS	W	72.24%	27.76%	13.24%	1.45	1.64
MLS	L	76.81%	23.19%	7.34%	1.41	1.62
UAS	D	88.59%	11.41%	6.05%	0.60	0.74
UAS	S	90.49%	9.51%	6.67%	0.63	0.78
UAS	W	93.54%	6.46%	2.38%	0.62	0.77
UAS	L	86.69%	13.31%	0.80%	0.66	0.84

Of the four ITDE algorithms we tested, the point cloud-based algorithm, L, produced the least accurate tree detection results for both aerial platforms, though this was true by a relatively small margin (91% versus 94-97% for MLS and 87% versus 89-94% for UAS). However, the case of the MLS point cloud, the L algorithm outperformed the raster-based algorithms (77% versus 72-73%) (Table 3). In terms of processing time, the L algorithm was by far the slowest for all the platforms, taking longer to complete than all the other algorithms we tested combined.

In terms of stem location accuracy, we found that the ALS was 75.3% accurate and the MLS was 96.2% accurate (n=263). When we compared the stems detected from the ALS data (210 stems) to those detected from the MLS data, we found that all of the ALS stems (100%) fell within 1.5 meters of an MLS stem (0% commission and omission error,  $\mu = 0.62$  m, RMSE = 0.68m). The stem locations from the MLS were also slightly less biased than the ALS, with overall  $\mu$  of 1.04 m (RMSE=1.26 m) as opposed to 1.16 m (RMSE = 1.13 m) (Table 4).

Table 3-4: Stem detection accuracy using the visually detected tree centers (n=263) as the reference points and the tree stem locations from the aerial platforms (ALS and MLS). No stems could be located from the UAS data.

<b>Platform</b>	<b>Stems Detected</b>	<b>Omission Error</b>	<b>Commission Error</b>	<b><math>\mu</math> (m)</b>	<b>RMSE (m)</b>
ALS	75.29%	24.71%	0.50%	1.16	1.13
MLS	96.20%	3.80%	0.39%	1.04	1.26

Our assessment of positional error showed that for 273 stems located from the MLS data, the treetops were accurately located most often using the ALS cloud (85-89%) followed by the UAS cloud (81-85%), then the MLS cloud (69-75%). The  $\mu$  and error between stem and treetop locations were least using the ALS data (1.01 m and 1.19 m, respectively), followed by the UAS (1.18-1.22 m and 1.36-1.40 m, respectively), and the MLS had the most (1.62-1.65 m and 1.77-1.83 m, respectively). Similar to the treetop detection analysis, we found that the MLS data resulted in more commission error (8-16%) than

either the ALS (3-8%) or the UAS (1-5%). Because the results for this comparison did not show much variation across the three raster-based algorithms, we chose to only display the results of the W algorithm and the L algorithm, leaving out both D and S in this portion of our results (Table 5).

Table 3-5: Tree positional accuracy results using the stem locations ( $n = 273$ ) from the MLS data as control points and the treetop coordinates within the segmented crowns using raster-based (W) and point cloud-based (L) ITDE algorithms. We found that the treetop points fell within 3 meters of the stem locations most often using the ALS data (85-89%), followed by the UAS data (81-85%), then the MLS data (69-75%). The biases ( $\mu$ ) and errors for the three platforms follow a similar pattern. Both aerial platforms had less commission error (3-8% for ALS and 1-5% for UAS) than the MLS layer (8-16%).

Platform	Algorithm	Accuracy	Omission Error	Commission Error	$\mu$ (m)	RMSE (m)
		[%]	[%]	[%]		
ALS	W	89.38	10.62	8.27	1.01	1.18
ALS	L	85.34	14.65	3.32	1.01	1.18
MLS	W	68.50	31.50	15.77	1.61	1.77
MLS	L	75.46	24.54	8.04	1.65	1.83
UAS	W	85.35	14.65	4.51	1.22	1.40
UAS	L	81.43	18.57	0.89	1.17	1.36

### 3.3.2. Height Estimation

Because it produced the best positional accuracy results for both aerial platforms, we used only the results of the W algorithm for comparing height estimates. The tree height estimates from the W tree segmentation overlapped for all three platforms for 157 of 273 manually identified trees (60%), which was the most of any of the algorithms. The height estimates for the two aerial platforms, UAS versus ALS, were the most strongly correlated ( $R^2=0.96$ ) (Figure 3-6a) and had the least error ( $\mu = 1.31\text{m}$ , RMSE 1.66m). In general, height estimates from the UAS were comparatively lower than those from the ALS. Tree height estimates from the MLS platform did not agree well with either the UAS ( $R^2=0.53$ ,  $\mu = 2.96\text{m}$ , RMSE=4.13m) (Figure 3-6b) or ALS ( $R^2=0.51$ ,  $\mu = 4.27\text{m}$ , RMSE=5.05m) (Figure 3-6c), and they tended to be underestimates compared to both other platforms' estimates. Distance from tree to road

did not significantly impact ( $\alpha = 0.05$ ) the differences in height estimates for UAS versus ALS (p-value 0.89) but did significantly impact the differences for MLS versus ALS (p-value 0.034) and for MLS versus UAS (p-value 0.047).

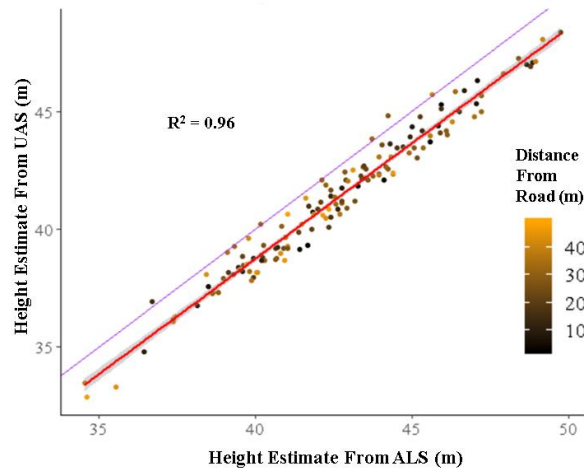


Figure 3-6a: Scatterplot and linear regression statistics for pairwise comparisons of tree height estimates between the three platforms we tested. Only trees which were detected by all three platforms ( $n=157$ ) were included in these models. Lines of best fit appear in red surrounded by shaded confidence interval (95%), while the line  $y=x$  appears in purple. Points are colored according to distance from the road, where blacker points are closer and orange points are farthest away.

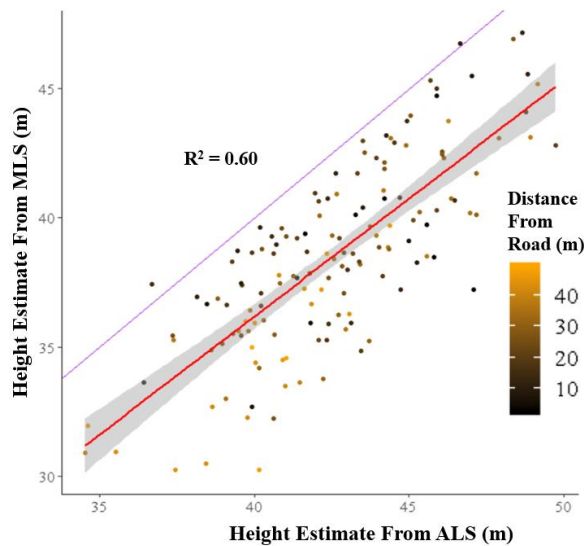


Figure 3.6b: Scatterplot and linear regression statistics for pairwise comparisons of tree height estimates between the three platforms we tested. Only trees which were detected by all three platforms ( $n=157$ ) were included in these models. Lines of best fit appear in red surrounded by shaded confidence interval (95%), while the line  $y=x$  appears in purple. Points are colored according to distance from the road, where blacker points are closer and orange points are farthest away.

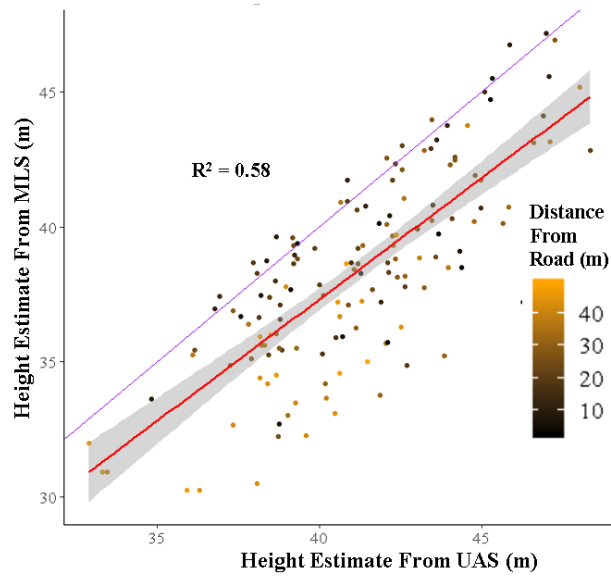


Figure 3.6c: Scatterplot and linear regression statistics for pairwise comparisons of tree height estimates between the three platforms we tested. Only trees which were detected by all three platforms ( $n=157$ ) were included in these models. Lines of best fit appear in red surrounded by shaded confidence interval (95%), while the line  $y=x$  appears in purple. Points are colored according to distance from the road, where blacker points are closer and orange points are farthest away.

### 3.3.3. Lean Assessment

We were able to estimate the lean,  $\theta$ , and azimuth,  $\alpha$ , for 259 trees using the MLS stem locations at 18m, 245 trees using the ALS treetop locations and W algorithm, and 246 using the UAS treetop locations. Lean maps for all platforms are shown in Figure 3-7. Visually, the lean estimates seem from the aerial platforms seem to bear more resemblance to one another than to those from the MLS. This is true of both the directionality ( $\alpha$ ), and angle ( $\theta$ ), however with  $\theta$  we see that the UAS estimates are the tend to be the largest, followed by the ALS, and then the MLS (stem-based) estimates.

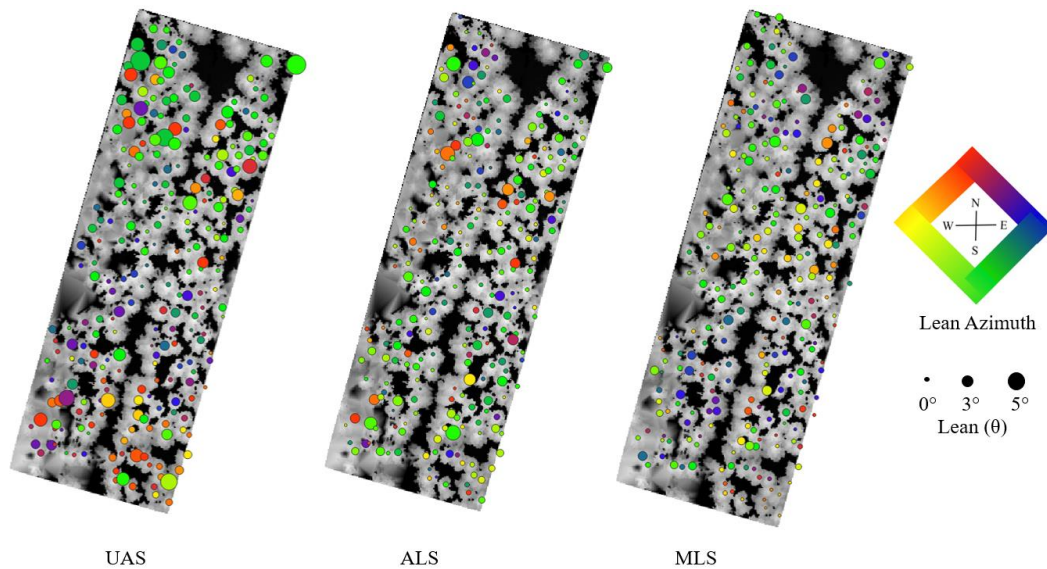


Figure 3-7: Tree lean estimates created using the locations of the stems at the base (1-2 m) as reference points and the horizontal distance to the stem location near the top (18-19m) (n=259) (right) compared to the horizontal distance to the treetop location from the ALS data (n=245) (center) and UAS data (n=246) (left). The points are scaled according to the magnitude of the tree lean and colored according to the azimuth. A greyscale canopy height model (CHM) from the ALS dataset is used as the background.

The distributions of the tree lean angle,  $\theta$ , are shown in Figure 3-8. The mean estimates for  $\theta$  were  $1.36^\circ$ ,  $1.55^\circ$ , and  $2.07^\circ$  for MLS, ALS, and UAS, respectively. The Pearson's correlation coefficients ( $r$ ) (Benesty et al., 2009) for the lean estimates from the platforms were 0.54 for ALS versus UAS, 0.31 for ALS versus MLS, and 0.24 for UAS versus MLS. Once again, these results indicate that the lean estimates tend to be greater from the airborne platforms than from the ground-based MLS, and the difference is larger for the UAS compared to the ALS. Also, the estimates from the aerial platforms show more similarity to one another than to the MLS estimates, though the overall correlations are weak.

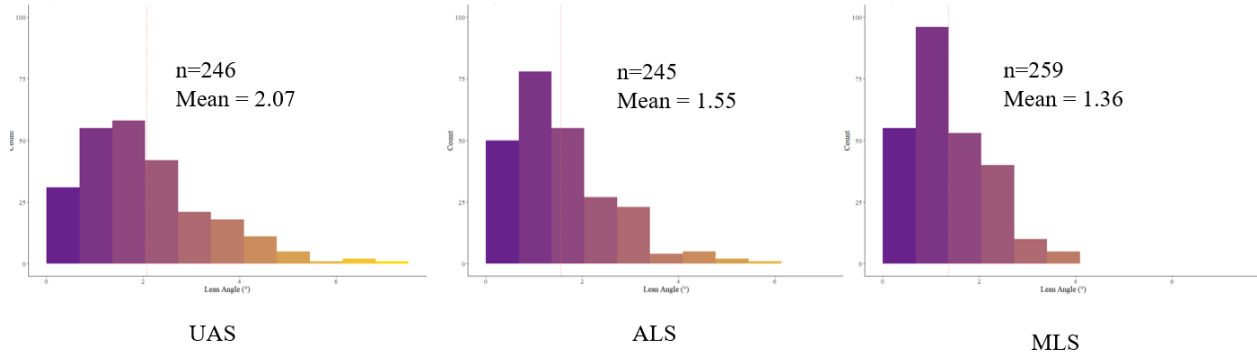


Figure 3-8: Distributions for tree lean angle ( $\theta$ ) estimated using stem location at 18m from the MLS ( $n=259$ ) (right), treetop locations from ALS ( $n=245$ ) (center), and treetop locations from UAS ( $n=246$ ) (left). Red dotted lines indicate the mean  $\theta$  for each platform ( $1.36^\circ$ ,  $1.55^\circ$ , and  $2.07^\circ$  for MLS, ALS, and UAS, respectively).

As for the lean azimuth estimates, we created histograms showing only the trees that were assumed to be leaning based on estimated  $\theta > 1.15^\circ$  (Figure 3-9). For MLS 152 trees met this criterion, which was the least, followed by ALS with 156 trees, then UAS with 191. The mean azimuth estimates across the platforms were similar, having only  $9^\circ$  of variation between them ( $177^\circ$ ,  $184^\circ$ , and  $175^\circ$  clockwise of N for MLS, ALS, and UAS, respectively). Despite this similarity, the overall correlations between the lean azimuth estimates were also relatively weak, having  $r = 0.38$  for ALS vs. UAS,  $r = 0.40$  for MLS vs. UAS, and  $r = 0.33$  for MLS vs. ALS.

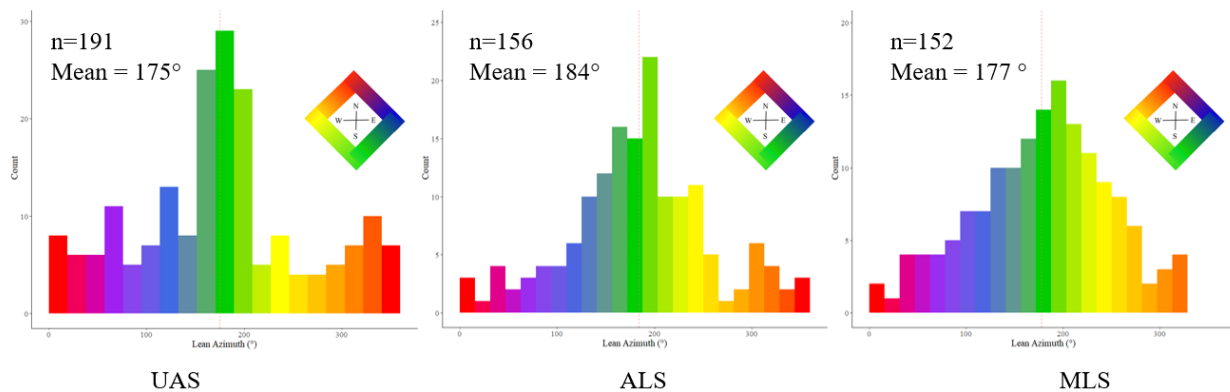


Figure 3-9: Distributions for tree lean azimuth for trees with lean angle  $\theta > 1.15^\circ$  estimated using stem locations at 18m from the MLS ( $n=259$ ) (right), treetop locations from ALS ( $n=245$ ) (center), and treetop locations from UAS ( $n=246$ ) (left). Red dotted lines indicate the mean  $\theta$  for each platform ( $177^\circ$ ,  $184^\circ$ , and  $175^\circ$  for MLS, ALS, and UAS, respectively).

### 3.3.4. Decimation Assessment

After the clouds were decimated, 8 out of 245 (3.3%) of trees were omitted from the ALS data and 15 out of 246 (4.8%) were omitted due to the treetop locations having fallen at least 8 meters from the stem, leaving 237 and 231 from the ALS and UAS, respectively. We show the height estimates for the remaining trees using the full resolution, 100 points/m<sup>2</sup>, and 10 points/m<sup>2</sup> data (Figure 3-10). It appears that the decimation has a limited effect on the reliability of the height estimates, though most of the differences are for trees shorter than 40 meters. The tendency for the UAS to consistently underestimate the tree heights with respect to the ALS is also apparent.

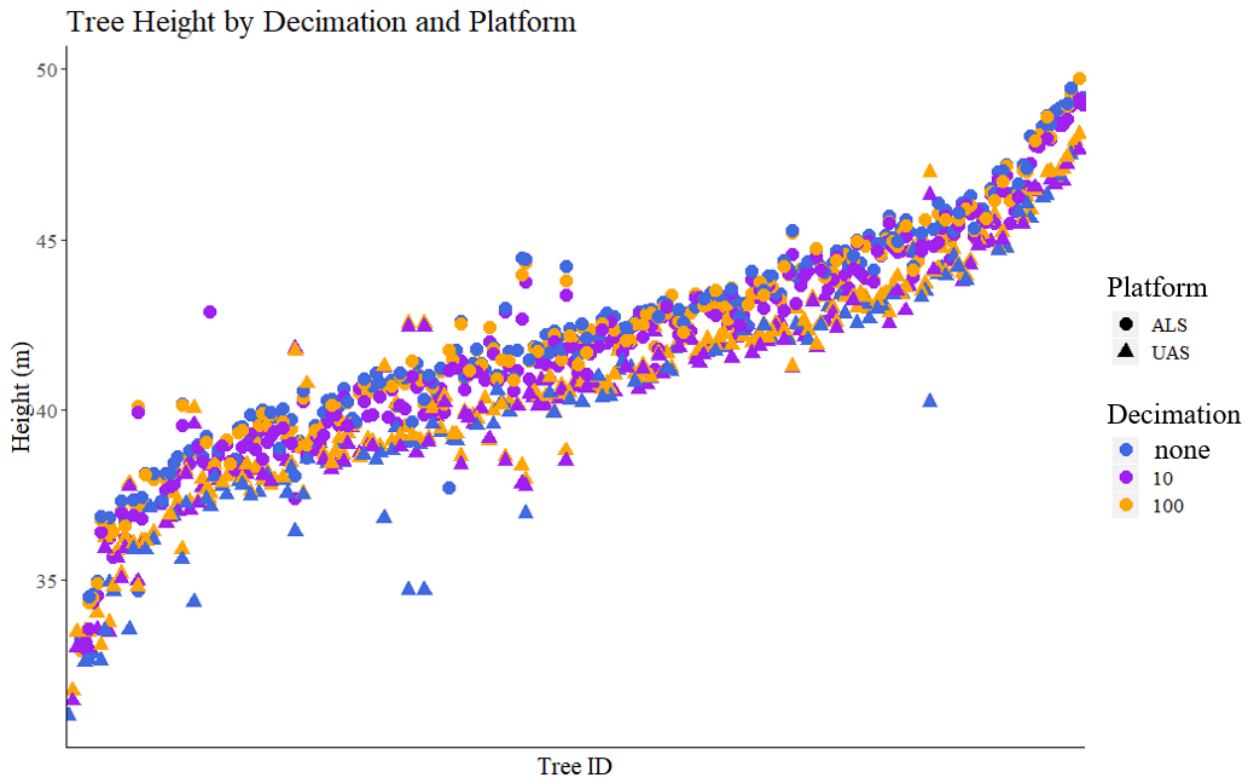


Figure 3-10: Tree height estimates from UAS and ALS platforms using undecimated point clouds (blue), 10 pts/m<sup>2</sup> (purple), and 100 pts/m<sup>2</sup> (orange). Observations are sorted by mean height estimate from least to greatest.

We conducted a similar comparison for tree lean,  $\theta$ , showing the lean estimates for ALS and UAS by decimation level in Figure 3-11. There are seemingly more errors with trees that have more lean (greater  $\theta$ ), with those errors usually resulting in overestimates following the decimation. The levels of

decimation that we tested were not markedly different from one another (i.e., the error did not increase from 100 to 10 points/m<sup>2</sup>).

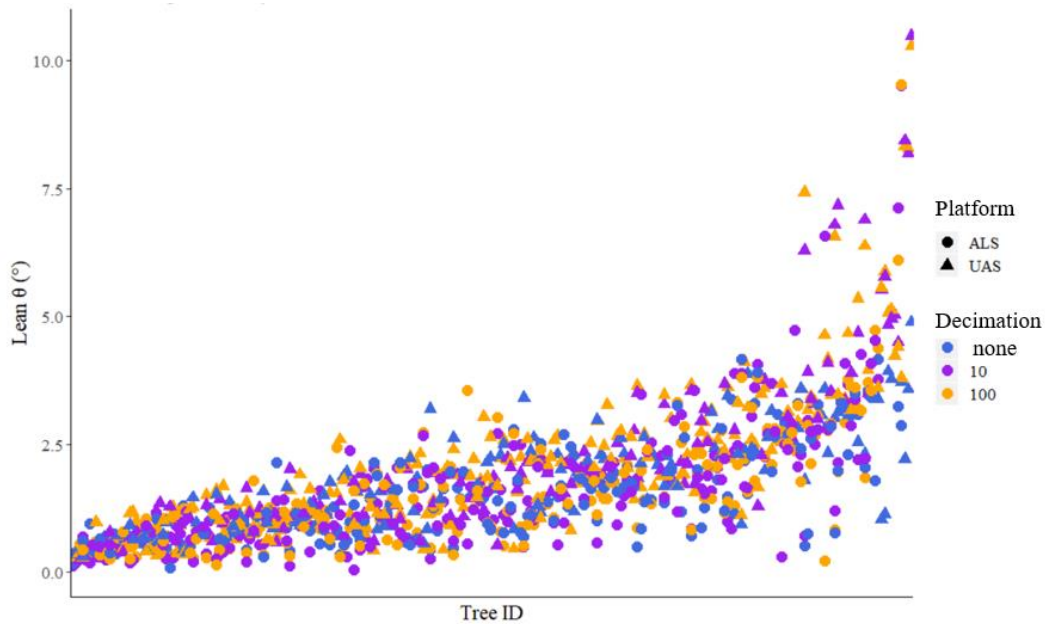


Figure 3-11: Scatterplot showing lean magnitude (m) calculated as the horizontal displacement between the tree stem at 1m height measured from the from the MLS and the treetop locations for the same trees from the ALS (circles) and MLS (triangles) clouds at full resolution (blue), 10 pts/m<sup>2</sup> (purple), and 100 pts/m<sup>2</sup>(orange). Observations are sorted by mean distance from least to greatest.

Due to the initial estimates being less correlated than the height or  $\theta$  estimates, we plotted the azimuth estimates across decimations separately for ALS and UAS (Figure 3-12). The shapes of the plots are similar, except for portions around 175° and 200° where some values appear to be missing from the UAS data. The same pattern is evident in the histograms in Figure 3-9. The azimuth estimates from both platforms appear to be sensitive to reductions in point cloud density. In particular, there are more points from the undecimated ALS data that fall away from the trendline than with the height or  $\theta$  plots, which suggests that some sensitivity to detecting the azimuth may be lost due to decimation. The same pattern appears in the UAS data but is less obvious in this case.

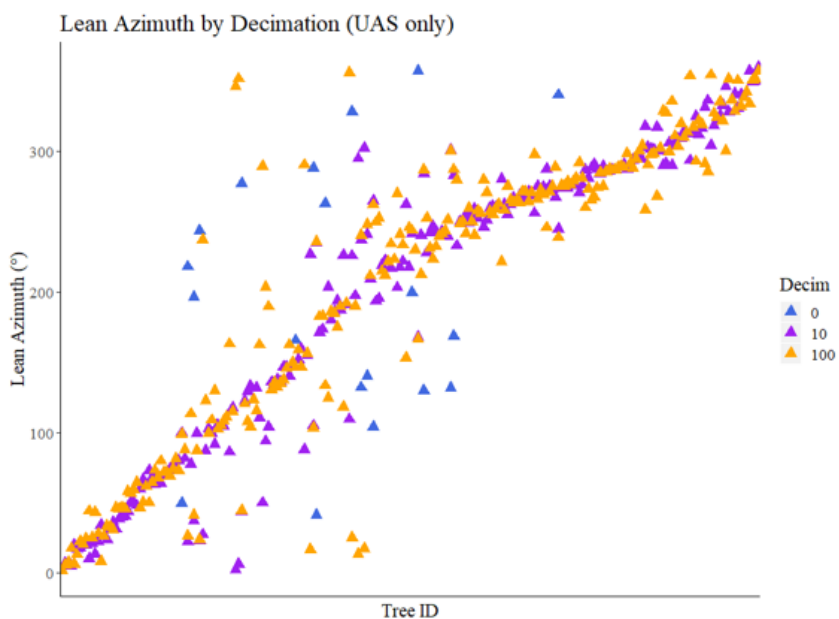


Figure 3-12a: Scatterplots showing lean azimuth in degrees clockwise of north for tree lean estimates by using UAS to detect treetops and measuring the horizontal distance from the stem center location at 1m height measured from the MLS. Observations are sorted by the mean azimuth angle from smallest to largest.

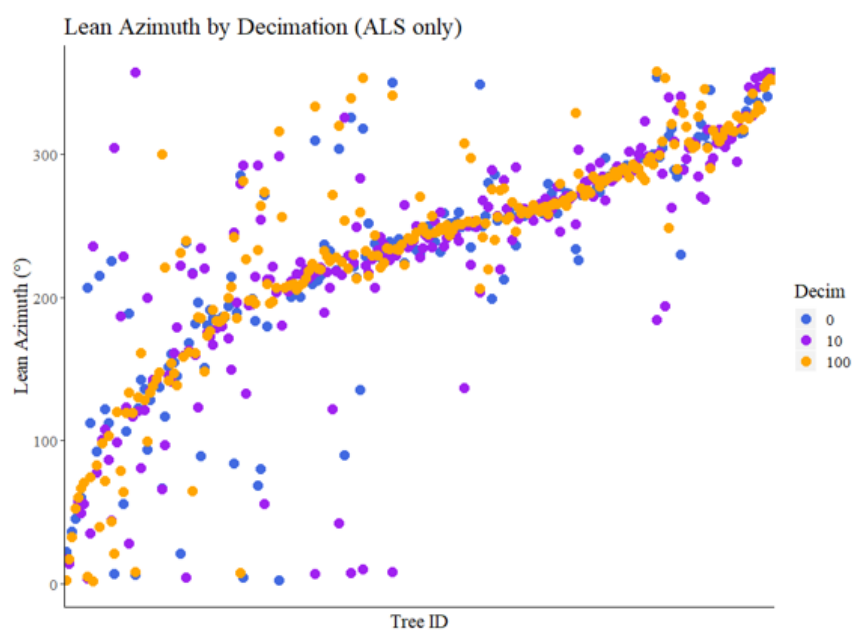


Figure 3.12b Scatterplots showing lean azimuth in degrees for tree lean estimates by using ALS.

## 3.4. Discussion

### 3.4.1. Stem and Tree Detection

For detecting treetops, the ALS and UAS platforms performed more accurately and produced less biased estimates than the MLS. The ALS performed slightly better than the UAS, but in general the two aerial datasets resembled one another more than the MLS data resembled either of them. This was true with regards to the DTM, CHM, and the treetop detection analysis. This is unsurprising considering the perspective of the sensors during data collection, but it is nonetheless an important consideration, particularly when forests are imaged from below the canopy. Based on this, we conclude that an aerial platform is needed to reliably locate the treetops. Also, there is some evidence to suggest that, based the large difference in cost and logistical demands, the photogrammetric platform (UAS) may be more suitable for widespread use than the ALS despite a small reduction in performance.

For detecting tree stems, the MLS platform had the highest accuracy, having detected 96% of the stems compared to the control. The ALS clouds performed moderately well, having detected 75% of control stems, while no stems were detectable from the UAS cloud. Again, this is related to the perspective of the ground-based MLS with respect to the tree stems, and it highlights the importance of reducing obstructions between the sensor and the trees. Despite the overall performance of the MLS being very good for detecting tree stems in this experiment, we noticed several limitations of the platform that should be considered. First, the functional range of the sensor is limited by the quality of the lidar scanner, specifically the power of the laser emitter and the sensitivity of the detector. The particular platform we used employed high-quality hardware and we found that stem detection was limited to about 75 meters from the road. The stand we scanned was managed such that it has a clear understory and a single crown-layer, which made it suitable for this analysis. However, obstructions like understory vegetation or suppressed trees would negatively impact stem detection from the MLS.

While we tested both an active and a passive sensor in the air, we did not test any passive sensors on the ground. Based on previous studies, it is possible to measure tree stem characteristics in this way (Forsman et al., 2016), as well as by using a UAV mounted camera tilted at an angle to image open stands (Fritz et al., 2013).

The segmentation algorithms we tested ranked differently in performance depending on the orientation of the sensor that was used. The raster-based methods worked best for the aerial datasets and achieved the best accuracy overall, while the point-cloud based method worked best for the MLS data. Many of the tops of the trees in the MLS point cloud are visibly missing from the data, making the crowns appear more jagged and asymmetrical than reality. These resulting crown shapes also seem less characteristic of a typical conifer crown, which helps explain why the raster-based algorithms do a poorer job of segmenting them. Specifically, if the approximate locations of the treetops are unreliable, in this case because the crowns are incomplete, the raster-based methods will have low-quality inputs in the form of erroneous seed point locations. On the other hand, the L algorithm was intended for use in mixed and complex coniferous forest (Li et al., 2012), which explains why it performed better than the raster-based methods with regards to segmenting trees from the MLS data. Because implementing the L algorithm takes much longer to process the data than the raster-based algorithms, there is a trade-off between efficiency and performance in this case.

### 3.4.2. Height Estimation

The height estimates for the aerial platforms strongly agreed in terms of correlation, but the UAS estimates were consistently lower than the ALS estimates. This is likely due to the generalization of stem and foliage features around the margins of the tree canopy that result from the structure from motion reconstruction process.

Andersen et al. (2006) point out that although the dominant source of error for tree height estimates is due to treetop location uncertainty, there can also be errors in the terrain location (i.e., the DTM).

According to Leckie et al. (2003), up to 0.5 m of height estimate error can be attributed to DTM error

when using airborne lidar data to estimate tree heights, and Reutebuch et al. (2003) showed that the overall DTM error was around 0.18 m when using higher resolution point cloud data for a thinned stand. . In our case, we saw that the error between the DEM layers for the two aerial platforms (ALS minus UAS) was relatively low ( $\mu = 0.21$  m,  $\sigma = 0.54$  m) compared to the error between the ALS minus MLS ( $\mu = 1.30$  m,  $\sigma = 1.67$  m) or the UAS minus MLS ( $\mu = 1.13$  m,  $\sigma = 1.73$  m). Due to the orientation of the sensor in the pickup truck bed, the number of ground returns from the MLS diminishes greatly moving away from the roadway. The low position of the sensor (2.5 m AGL) results in extremely acute incidence angles for ground returns. Moving from 25 to 50 m away from the sensor and assuming flat ground, the laser incidence angle diminishes from  $5.7^\circ$  to  $2.9^\circ$ . According to the differences between the DEMs and the aerial platforms (Figure 3-13), we can infer that this is the approximate range where the MLS ground return data become unreliable. Nonuniform terrain, understory vegetation, and other natural obstructions could shorten this range.

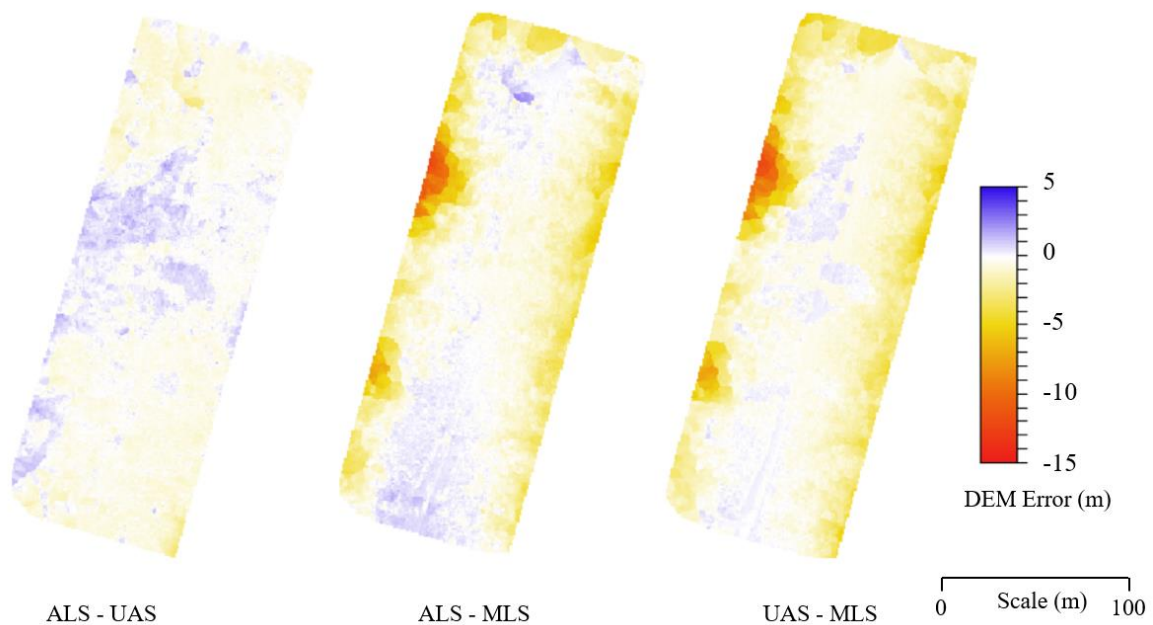


Figure 3-13: Differences in elevation for the digital elevation model (DEM) layers created using point clouds from the three platforms we tested.

While this disagreement between the DEM values from the platforms partially explains the poor performance of the MLS platform for estimating tree heights, our findings agree with Andersen et al. (2006) and Holopainen et al. (2013) in that the more fundamental problem is obscuration of the treetops by the lower canopy. Specifically, we saw that although the DEM and CHM data for MLS were similar in that the data quality decreased moving away from the road, the magnitude of the largest differences between the MLS data and aerial platforms were several times larger for the CHM compared to the DEM (Figure 3-14).

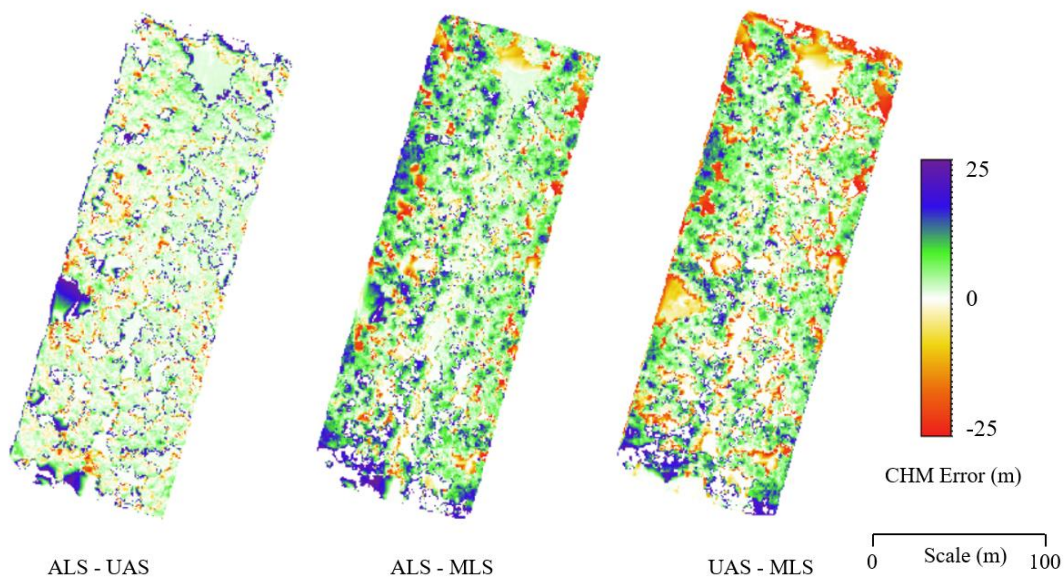


Figure 3-14: Differences in height for canopy height model (CHM) layers created using point clouds from the three platforms we tested.

### 3.4.3. Lean Assessment

The purpose of comparing the three platforms' ability to detect the tree stem and treetop locations in this study was to determine which were suitable for identifying leaning trees. Discrepancies in the locations of GNSS located tree stems and the locations of treetops according to ITDE algorithms have been attributed to tree lean (Jakubowski et al., 2013), and such trees could be better accounted for in such analyses if they were identified in advance. The MLS data provided very detailed reconstructions of stems, both at the base and at the top. We found that manually fitting circles to rasterized slices of the

stems was suitable for locating the stem centers from the MLS data, though the method is tedious and could possibly be automated (Herrero-Huerta et al., 2018). However, because the sensor is positioned in the bed of the truck and mounted at a 45° angle toward the rear, perspective of the sensor with respect to the tree shifts as the MLS approaches the tree. This results in the orientation of the crescent-shaped stem sections rotating around the stem as the tree is scanned from top to bottom while the MLS approaches (Figure 3-4 inset).

Additionally, the quality of the data produced by the MLS platform is highly constrained by the distance from the road. This is less of an issue with stems compared to ground returns or treetop locations as discussed previously due to the orthogonal position of the stems with respect to the sensor and the lack of obstructions in between. However, if there are insufficient ground returns to provide an accurate DEM, stem heights above ground would be uncertain, highlighting the value of combining MLS and aerial reconstructions. Based on our results, we suggest that either active or passive sensors (i.e., platforms and techniques used for our ALS and UAS, respectively) can be used to provide valuable aerial data for this purpose. Considering these limitations, we find that the MLS provides an effective method for estimating tree stem lean. Future studies might use similar data to look at the departure of stems in greater detail. For example, creating more slices (i.e., at regular intervals) along the stem would allow for differentiation between leaning trees that have straight stems and stems that have sweep.

Using the treetop locations from the ALS and UAS point clouds did not provide reliable estimates of tree lean angle or direction when compared to the stem lean estimates from the MLS. Of trees that were classified as leaning or not leaning based on a 1.15° threshold the MLS data, 61% were correctly classified using ALS treetops, and only 52% with the UAS. Based on our findings, we suggest that for tall conifers the Euclidian distance between the base of the stem and the top of the crown may not be a good predictor of stem lean angle or azimuth. The estimates we produced with the ALS, and more so, the UAS, tended to be larger in terms of  $\theta$  than the stem estimates, which can be explained in part by

asymmetry in the upper portion of the crowns that can result in the treetop being moved away from the base of the stem regardless of tree lean.

However, the treetop locations from both aerial platforms produced using the ITDE algorithms and the aerial platforms were effective in our positional error assessment. Both platforms had above 80% overall accuracy with RMSE  $< 1.4$  meters. This suggests that for large trees, perhaps treetop locations from aerial surveys can be used to locate tree stems from MLS scans, and vice versa.

#### 3.4.4. Decimation Assessment

All the raw point clouds we tested were high resolution, which is generally beneficial but results in large computational demands and prolonged processing time. We tested two decimation scenarios in order to simulate lower resolution datasets that, in theory, might result from the data collection itself (i.e., the hardware or the speed of the vehicle) or from post-processing in order to increase throughput.

For height estimation, the decimations we tested did not have a strong effect on the estimates from the aerial platforms. Though 10 points per meter data would not be considered low resolution compared to manned aerial lidar scans, this represents at least a 40x reduction in average point density compared to our raw clouds, which translates to a major reduction in storage requirements and processing time. Based on this, there is some evidence both ALS- and UAS-type platforms can be used to produce much lower resolution clouds than the ones in this study in order to estimate tree height using unmanned aircraft (i.e., with active or passive sensors).

The decimations did change the lean angle and azimuth estimates that resulted from the UAS and ALS data. For lean angle, we saw that most of the error occurred with trees that leaned the most. Also, we saw that lowering density resulted in a reduction in the lean angle estimate. The reduction in  $\theta$  from decimation is unsurprising because the treetop locations tend to move down in terms of height with increasing decimation. In fact, they never move upward, which results in the Euclidian distances

generally getting smaller as well, which results in smaller  $\theta$ . In terms of estimating azimuth, the decimations seemed to result in reduced sensitivity, especially in the ALS data.

At least within the context of how we compared the lean estimates, it seems that the effects of the decimation procedures are, in practice, less important than the general lack of agreement between the aerial and ground-based estimates. The lean classification accuracy values that we reported above for ALS and MLS do not worsen following decimation, though they only marginally improve and were poor initially. For ALS, the original accuracy was 61%, at 100points/m<sup>2</sup> it was 64%, and at 10 points/m<sup>2</sup> it was 57% (Figure 3-15). For the MLS, the original accuracy was 52%, at 100points/m<sup>2</sup> it was 52%, and at 10 points/m<sup>2</sup> it was 53% (Figure 3-16).

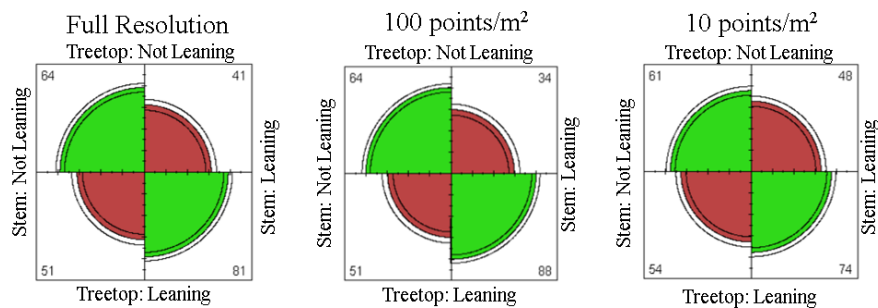


Figure 3-15: Confusion matrices comparing classification of trees into “leaning” and “not leaning” classes according to the lean angle based on the horizontal distance between the stem center at 1m measured from the MLS and the stem center at 18m (x-axis) versus the lean angle based on the horizontal distance between the stem center and the treetop measured from the ALS at full resolution (left), 100pts/m<sup>2</sup> (center), and 10pts/m<sup>2</sup> (right) (y-axis).

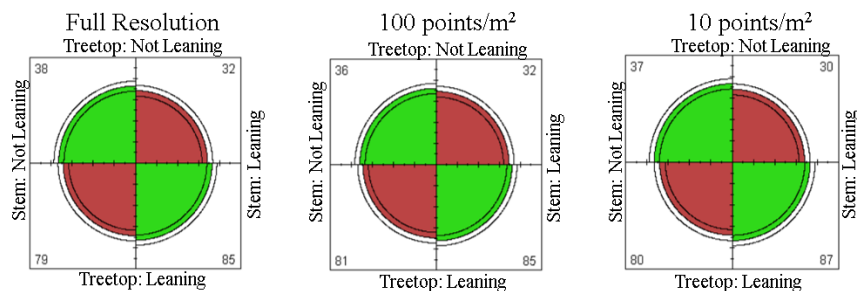


Figure 3-16: Confusion matrices comparing classification of trees into “leaning” and “not leaning” classes according to the lean angle based on the horizontal distance between the stem center at 1m measured from the MLS and the stem center at 18m (x-axis) versus the lean angle based on the horizontal distance between the stem center and the treetop measured from the UAS at full resolution (left), 100pts/m<sup>2</sup> (center), and 10pts/m<sup>2</sup> (right) (y-axis).

### 3.5. Conclusions

Regarding the creation of point cloud data for making single tree measurements, we found that there are tradeoffs between the performance, cost, and ease of operations across the platforms we tested. The most expensive platform, MLS, produced the highest resolution data and was the easiest to use. However, the file sizes associated with dense point clouds results in more computational demands and expertise required for post-processing. Because we did not perform any decimation on the MLS data, it is unclear whether lower resolution data (i.e., from a less expensive ground-based platform) could be used in a similar way.

In comparison, the UAS platform produced the lowest quality point clouds, but it was also the least expensive by a large margin. The process of using SfM to reconstruct images in 3D results in a loss of some of the fine scale texture of tree crowns, but based on our results, retains the general position and size of the individual trees when compared to the ALS scans. Furthermore, the ALS and UAS performed comparably well at detecting treetop locations compared to the MLS, though the ALS was slightly better. Thus, we provide some further evidence of the value of consumer-grade UAV platforms for single tree mensuration in mature forests. We did not test any passive sensor platform from the ground, though including such a platform (i.e., a motor vehicle with a multispectral camera mounted horizontally) would be interesting for comparisons in future studies.

For detecting tree stems, the MLS platform did the best, having detected 96% of the stems compared to our visual control. The ALS performed moderately well, having detected 75% of stems. One of the limiting factors for stem detection using this particular ALS platforms was the lack of programmed flight missions, which are fundamentally important for systematically covering large areas and can be performed with similar hardware and more up-to-date software. In the case of the UAS, no stems were detectable from the point cloud, which is not surprising, given the vantage point of the platforms and the inability of the multispectral imagery to penetrate the forest canopy.

The ITDE algorithms we tested all performed relatively well if parameters were optimized, including the three raster-based approaches and one cloud-based approach. However, the cloud-based L algorithm did perform slightly worse than the raster-based algorithms when applied to the aerial datasets, and since it was also the most time-consuming procedure, we found that it was less suitable than the other methods within the context of our study.

We also found that the treetop locations detected from the ALS and UAS were within the vicinity of the stems for more than 85% of cases. This suggests that the treetops could be used to infer the locations of stems that are located from the MLS platform, and again that the UAS is adequate for this analysis despite its lower cost and general convenience. Overall, the MLS is the least suitable platform for detecting treetops. The ground-based perspective of the platform, not the quality of the sensor, is the main driver for this.

The height estimates from the ALS and UAS platforms were strongly correlated, though the UAS seems to systematically underestimate the values. However, the MLS was not effective for estimating tree heights. The error from these estimates propagates moving away from the sensor, which travels along the road. The unreliability of the MLS for height estimates can be attributed to a combination of treetop location error, which is the primary source and is evident in the CHM data, as well as DEM error.

The MLS platform produced very robust reconstructions of tree stems, which we used to estimate tree lean by measuring the horizontal departure between the stem position at the base and near the top. For trees that were closer to the road (< 20 m), the cross-sections that resulted from slicing the MLS cloud parallel to the ground allowed us to easily fit circles to the stems visually. The same slicing procedure we used to estimate the overall lean of these trees could be performed at more locations (i.e., at regular intervals) along the stems, which would facilitate more inference about lean properties. This has been demonstrated with single trees using a stationary platform (Thies et al. 2004), and here we show it could likely be expanded using a mobile platform.

We also estimated lean using the horizontal distances between the base of the stem measured by the MLS and the treetop location detected from the aerial platforms. The lean estimates across the aerial platforms were similar to one another, but when we compared the estimates of tree lean ( $\theta$ ,  $\alpha$ ) using only the stems with the estimates using the treetops, we found that the treetop lean estimates tended to be greater in terms of  $\theta$  and generally were in disagreement with the stem lean estimates.

Decimating the aerial point clouds from over 400 points/m<sup>2</sup> to 10 points/m<sup>2</sup> did not greatly change the height estimates from the aerial platforms, which suggests both ALS- and UAS-type platforms can be used to produce much lower resolution and which can be used to estimate tree height using unmanned aircraft (i.e., with active or passive sensors). However, decimation did have an impact on the agreement between the lean estimates for ALS and UAS, though it seems that point cloud density may be less of a limiting factor for producing reliable lean estimates when compared to the lack of agreement between the aerial and ground-based estimates.

#### 4. Quantifying Lean for Stem Models of Mature Douglas Firs

## Abstract

Tree lean is used to conduct hazard tree assessments and can influence wood quality, so it is commonly included in forest inventories. Douglas Fir (DF) (*P. menziesii*) is the predominant commercial species in the United States Pacific Northwest. Our study compared two strategies to estimate DF tree lean from MLS. The first was a more conservative estimate, total lean, which used the horizontal distance between center near DBH and the stem location near the base of the crown, and the second was a more precise estimate that used the mean of 7 intermediate angles spaced out along the boles. In the process of locating the stem centers, circular vectors were fit to the trees which allowed for extraction of diameter measurements from the MLS data along the stems. A total of 4 existing stem taper and 3 stem volume equations were tested using MLS data using the DBH and total heights as predictors (i.e., as presented in the literature), then the DBH estimates were replaced with the diameter at 5 meters above ground ( $D_5$ ) and tested again. Because there is evidence that the minimum lean angle that results in detectable changes in tree physiology is around  $2^\circ$  for some species, and because this has not been investigated for DF specifically, a simple procedure is proposed to add lean estimates and associated variable coefficients as predictors to existing models predicting stem geometry. The distance from the scanner to each tree was also measured and tested as a predictor in the models. Results show evidence that fitting models using only leaning trees tends to result in increased bias and error compared to modeling only vertical trees, hence, it seems that lean should be considered when modeling stems of mature DF. When DBH was replaced with diameters at 8 heights spaced along the bole, we found that leaning trees showed a dramatic improvement in the models when the input height was from 7 or 10 m above ground, while the vertical trees had consistently favorable results using heights between 5 and 15m.

## 4.1. Introduction

The deviation of mature conifer stems from a vertical position, known as tree lean, is of interest to the forestry community as it plays an important role in forest operations and wood processing. For forest operations and in urban forest settings, lean is an important component of hazard tree risk assessment (Mortimer and Kane, 2004). From a commercial standpoint, lean can influence wood quality because lean has been shown to increase the proportion of reaction wood (Wilson and Archer, 1977). As such, visual assessments of tree lean, estimated using the apparent displacement of the observed tree top and base, are typically included in forest inventories (Gatziolis et al., 2010b) as well as for research such as allometry (Kramer et al., 2018).

Advancements in forest mensuration, particularly the advent of light detection and ranging (lidar) scanning, have pointed the importance of tree lean as a source of error for single tree measurements. Tree heights from the 3D reconstructions produced by lidar, known as point clouds, tend to either underestimate or overestimate trees leaning, depending on the location, uphill or downhill, respectively (Gatziolis et al., 2010b). Tree segmentation algorithms, which separate trees from one another within point clouds, are integral to producing single-tree estimates from lidar. Being automatic, some algorithms have shown to be negatively impacted by lean (Strîmbu and Strîmbu, 2015). Also, as noted in the previous chapter, trees that lean are more prone to positional errors when located from above due to the stem being placed away from the tree top (Garms et al., in review).

Estimating the locations (i.e., coordinates) of conifer stems from high quality aerial lidar scanner (ALS) data is possible, but has been shown to produce several meters of error (Edson and Wing, 2011). However, mapping entire tree stems from aerial lidar scanner (ALS) data is extremely challenging because the scans provide too few stem returns to reliably infer stem geometry (Gatziolis et al., 2010b). Ground-based stationary lidar scanners, known as terrestrial laser scanners (TLS), capture point cloud data from a more favorable perspective than ALS, which results in stem reconstructions that are suitable for measuring diameters, but require multiple scans and subsequent coregistration of data for sampling

large numbers of trees (Henning and Radtke, 2006). In fact, Thies et al. (2004) used TLS data to model the shape (i.e., the taper, sweep, lean magnitude, and lean direction) of tree stems over 15 years ago, though the study included only two trees.

By combining lidar with ground-based vehicles and positioning systems consisting of inertial measurement units (IMU) with global navigation satellite systems (GNSS), nonstationary analogues to TLS have been developed, namely mobile lidar scanners (MLS). In the past decade, MLS have been utilized in a number forestry research efforts, including stem mapping (Holopainen et al., 2013; Pierzchała et al., 2018; Tang et al., 2015), tree crown segmentation (Tao et al., 2011; Zhang et al., 2015), and forest inventory (Čerňava et al., 2017; Fan et al., 2018). Many of the previous implementations of MLS used hand-held or backpack mounted platforms, which require a technician to walk through the stand and are constrained by coverage efficiency (i.e., time required to scan a given area). Other studies have demonstrated the use of motorized passenger vehicle (i.e., “street legal”) MLS in urban forestry applications, which is a logical initial implementation given the prevalence of open-grown trees and lack of understory vegetation in urban settings. In Chapter 2, I showed that street legal MLS can be used in conjunction with ALS make single tree estimates of mature Douglas Fir. The study by Garms et al. (2020) and others (Čerňava et al., 2017; Strahler et al., 2008) have shown that MLS has limitations, which should be taken into consideration for below canopy mapping, including obstructions (i.e., branches or understory vegetation), and terrain ruggedness. Another limitation of MLS, common across all lidar platforms, is the distance between the scanner and the object of interest. Given the promises shown by previous studies that utilized MLS to analyze stems and the prevalence of access roads in operational forests, it seems that MLS data would be suitable for quantifying tree lean in the context of forest management. If so, it is possible that lean estimation using MLS would be more accurate and more objective than visual surveys, which are the status quo, while also being more efficient than TLS, which is the most accurate method that has been presented.

There is limited consensus regarding the magnitude of lean angle (i.e., the departure from vertical) required for a tree to be considered leaning. For loblolly pine (*Pinus taeda* L.) and longleaf pine (*Pinus palustris*), Pillow and Luxford (1937) considered trees having between  $0.5^\circ$  and  $2.5^\circ$  of lean as slightly leaning, trees with between  $2.5^\circ$  and  $5.5^\circ$  as moderately leaning, and trees with  $< 5.5^\circ$  as pronounced leaning. The notion that trees with  $0.5$ - $2.5$  degrees are in fact leaning is supported by the evidence that trees in this category had differences in rate of diameter growth and formation of reaction wood compared to straight trees (i.e., trees with lean  $< 0.5^\circ$ ). For Oregon white oak (*Quercus garryana*), Lei et al. (1996) used  $2^\circ$  as the minimum cutoff for slightly leaning trees. When using TLS to reconstruct a single European beech (*Fagus sylvatica* L.), Thies et al., (2004) considered that a  $1.03^\circ$  lean angle is non-leaning. Rather than reporting the lean as degrees (or radians) from vertical, Thies et al. (2004) described the lean as the average linear rate of departure from verticality (i.e.,  $1.8 \text{ cm/m}^{-1}$ ). Thies et al (2004) approach is intuitive because it reflects the way that lean is traditionally estimated: by assessing the horizontal distance between the base of the tree and its top. For comparison,  $1^\circ$  of lean is equivalent to  $1.75 \text{ cm/m}^{-1}$  of horizontal departure, so the  $2^\circ$  lean threshold used by Lei et al. (1996) translates to 70 cm of departure between the top and bottom of a 20 m stem. Based on this example, it is plausible that  $2^\circ$  ( $3.5 \text{ cm/m}^{-1}$ ) is adequate for a tree to present as slight lean upon visual inspection, and also potentially insufficient for precise manual measurements. The value of  $2^\circ$  is supported by the literature as the approximate point where lean begins to effect tree physiology such as growth and wood properties. The  $2^\circ$  threshold is also aligned with common practices, as being slightly greater than the minimum amount of lean that could be reliably detected visually.

Douglas fir (*Pseudotsuga menziesii*) (henceforth DF) is the predominant commercial softwood tree species in western North America (Bose et al., 2018). To appraise the value of living trees, many stem taper equations (i.e., equations to predict the diameter of the bole at different heights) have been produced (Wensel and Olson, 1995a). Another option for estimating the value of standing timber is to model the volume of the whole stems directly, thus, several cubic tree volume equations also exist for

DF (Wensel and Olson, 1995b). In general, both the stem taper and volume equations are typically nonlinear models, often with variable exponents, that rely on the total tree height and diameter as predictors. For diameter, the most common measurement is diameter at breast height (DBH), but there is evidence that models using some height higher on the bole instead of DBH, such as the midpoint between the tree top and breast height, perform better (Cao and Wang, 2015). It has also been shown that using a second diameter measurement in addition to DBH can improve the fit of the models (Cao, 2009). Point cloud data produced by MLS cover entire tree stems, which allows estimation of diameter higher on living tree boles without separate instruments or additional labor costs to be made *in-situ*, common to traditional forest measurements.

Because MLS is suited to digitally reconstruct tree stems due to the perspective, orientation, and trajectory of the platform, it can be used to detect subtle morphological characteristics of trees, such as slightly leaning stems. Most previous studies and field measurements describe lean as an aggregate value, (i.e., total lean), assuming that leaning stems are straight. However, trees can exhibit curvature along the stem, known as sweep and crook (Cunningham, 2012). In practice, stem curvature is recorded as a binary variable, such as present/absent, but the ground based laser scans can provide a numerical value to the bend (Thies et al., 2004). Nevertheless, a tree with sweep or crook is formally leaning, as the stem is not vertical, as its center deviates horizontally from the base. Irrespective of the reason for lack of stem verticality, lean, sweep or crook introduces stress in the wood, with significant impacts on wood quality. Therefore, the objective of this study is to assess the impact of the stem verticality, henceforth labeled as lean, on estimation of two of the most important forest inventory attributes, namely diameter and volume, using lidar point clouds. We have decided to label the lack of verticality as lean, as DF rarely exhibits sweep or crook.

## 4.2. Methods

### 4.2.1. Study Site

The study was conducted within Oregon State University's McDonald Research Forest, roughly 5 km north of Corvallis, Oregon, USA. The study area comprised a small (~4 ha) managed DF shelterwood stand that was planted in 1953 and thinned in 1986 (**Error! Reference source not found.**). The location was selected because, in multiple respects, it was suitable for MLS scans. First, the stand was crossed by a forest road through the middle, which was necessary for access. Also, the road being located along a ridge feature helped accurate location of the point cloud, as the GNSS was always visible. The terrain was generally flat, with a small amount surface relief. Finally, the thinning treatment resulted in a relatively open understory, with limited obstructing vegetation and debris, which allowed the laser pulses to penetrate the stands and register return points along the entirety of tree stems.

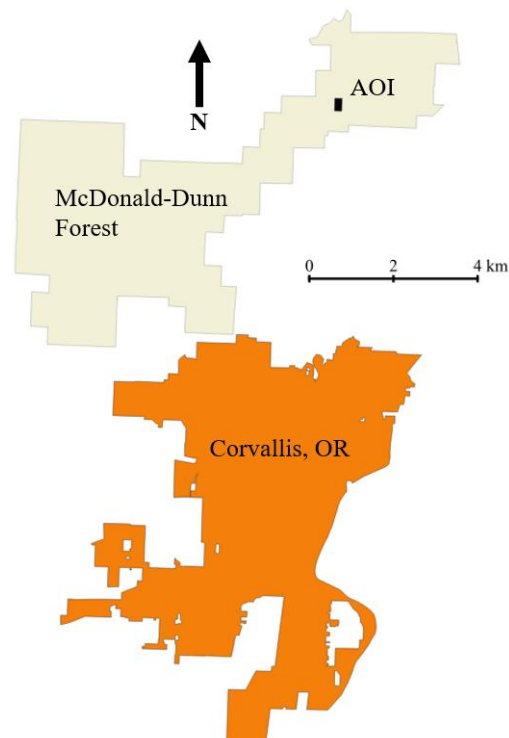


Figure 4-1 Location of the area of interest (AOI) within Oregon State University's McDonald-Dunn Research Forest

### 4.2.2. Data Collection

The MLS scans for this study were conducted on 5 March 2018. The MLS platform consisted of a Toyota Tacoma pickup truck, Velodyne HDL-64E lidar unit, a Topcon IP-S2 HD GNSS-aided inertial navigation system, and a distance measurement indicator. The lidar unit can record more 2 million points per second, has 64 channels, a vertical field of view of  $26.9^\circ$  and a range of 120 m. The entire system was purchased by the Oregon Department of Transportation (ODoT) and granted to Oregon State University in 2015. The platform was intended for asset inventory, bridge clearance assessment, and other uses by ODoT, so the sensor was mounted at a  $45^\circ$  angle tilted toward the rear of the vehicle (Figure 4-2).

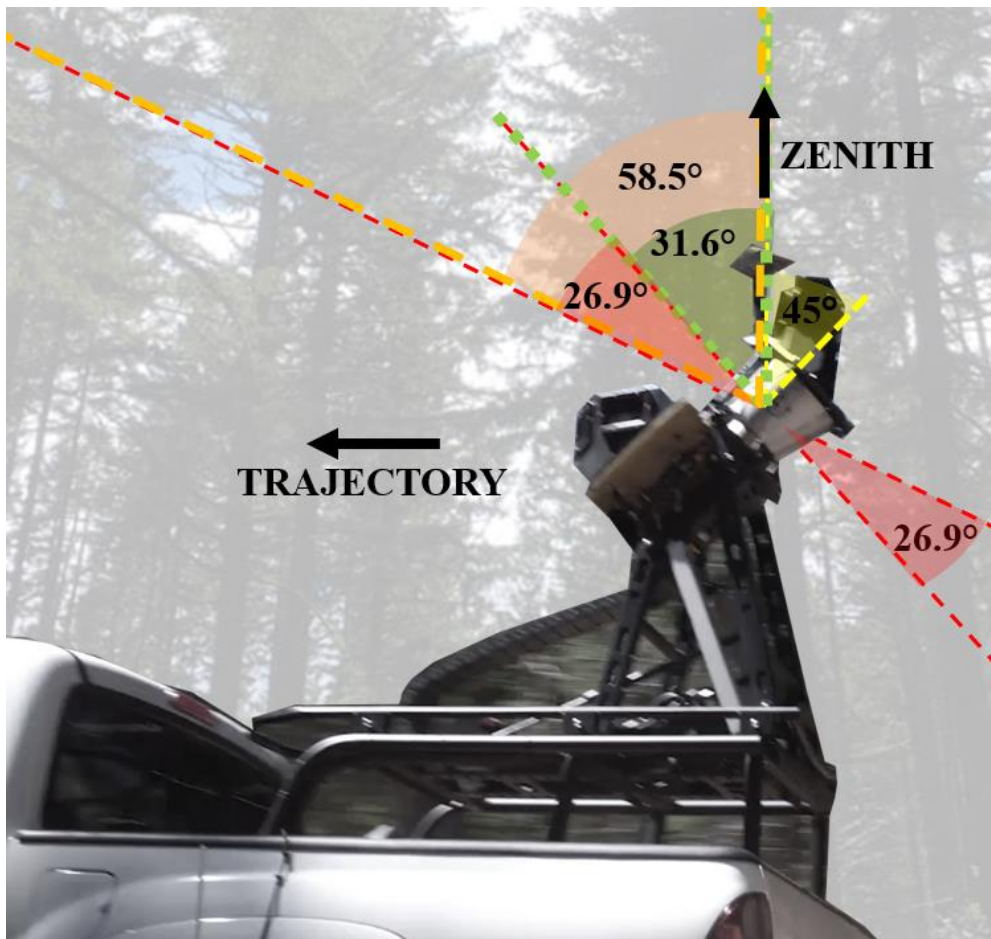


Figure 4-2: Orientation and scan angle of MLS from this study. The sensor has a vertical field of view of  $27^\circ$  and is tilted at  $45^\circ$  backwards. The beam angle ranges from  $31.5^\circ$  to  $58.5^\circ$  from vertical as it scans above and in front of the truck.

Tree heights were measured on 9 February 2018 using an unmanned aerial system (UAS) equipped with a lidar sensor, or an unmanned aerial lidar scanner (UALS). For validation of the height estimates, we also measured the heights using digital reconstructions built from multispectral images taken from a UAS. This process is known as 3D structure from motion photogrammetry (SfM) (M.J. Westoby et al., 2012). The hardware, data collection and data extraction processes for both the UALS and SfM height estimates were also described in the previous chapter (Garms et al., in review).

The tree heights were estimated using a DJI S1000 unmanned aerial system equipped with a Velodyne Puck LITE sensor and the OxTS XNAV200 GNSS-aided inertial measurement unit. The Velodyne Puck operates in 16 channels, has a 100 m range and generates 300,000 points/second. The unit flew on 9 February 2018, in the same dormant season with the acquisition of the MLS data. To estimate the height, each tree was visually identified, to reduce the omission and commission error. To decrease even further the tree identification errors, the process was carried out by two different persons, and was supplemented by the marker-controlled watershed tree segmentation algorithm (Meyer and Beucher, 1990b). The final trees were decided after the analysis of the differences, namely trees that were missed or added, among the three sources.

On 31 March and 3 April 2020, I measured the DBH of 90 trees using a diameter tape. Trees were sampled across a range of sizes and distances from the road and were spatially distributed across the study area. The trees were expected to have grown the elapsed time, but by small increment in proportion to the large, mature stems (mean DBH=73.01). The purpose of including these data was to consider the general accuracy of the diameter values garnered from the MLS point cloud data.

### 4.2.3. Preprocessing

Ground points, detected from the MLS point cloud with the cloth simulation filter (Zhang et al., 2016) implemented using the R package “lidR”(Roussel, 2017), were used to create a digital terrain model (DTM). The MLS point cloud was normalized by subtracting the DTM value from the elevation of each point. The normalized point clouds were sampled into 1m tall slices, parallel to the ground,

starting at 1m, 3m, 5m, 7m, 10m, 12m, 15m, and 18m. Each of the eight slices was compressed into a 2-dimensional raster image (orthographic view) with 1cm resolution. The raster slices were georeferenced to NAD83(2011) with coordinates in the UTM zone 10N projection (EPSG:26910).

Circles representing the cross section of the stem were visually fit to match the inner edge of the crescent-shaped stem impressions of each raster slice by selecting 3 points per slice. For each circle, the diameter and centroid coordinates (easting, northing) were calculated. To compute the distance from the tree to the sensor, I have used the slice at 1 m elevation. All spatial processing of the slices was executed in QGIS version 3.6 (QGIS Development Team, 2015).

Using the Cartesian coordinates of the stem centroids at 1m (i.e.,  $x_1, y_1$ ) and 18m (i.e.,  $x_{18}, y_{18}$ ), I calculated the total lean as the angle between the horizontal misalignment of the two centroids (Eq. 1)

$$\theta_{net} = \tan^{-1}\left(\frac{\sqrt{(x_{18} - x_1)^2 + (y_{18} - y_1)^2}}{H_{18} - H_1}\right)$$

where  $H_1 = 1\text{m}$  and  $H_{18} = 18\text{m}$ . For modeling purposes, angles were measured in radians, whereas for reporting purposes they were converted to degrees.

To provide a lean estimate while considering its variation along the stem, I calculated the sectional lean ( $\theta_i$ ) ( $i=1, 2, \dots, 7$ ) for each pair of adjacent slices starting with the 1 m ( $\theta_1$ ) and ending with 18 m ( $\theta_7$ ). I calculated the lean in this case as average lean of each section, remembering that there are 7 slices:

$$\bar{\theta} = \sum \theta_i / 7$$

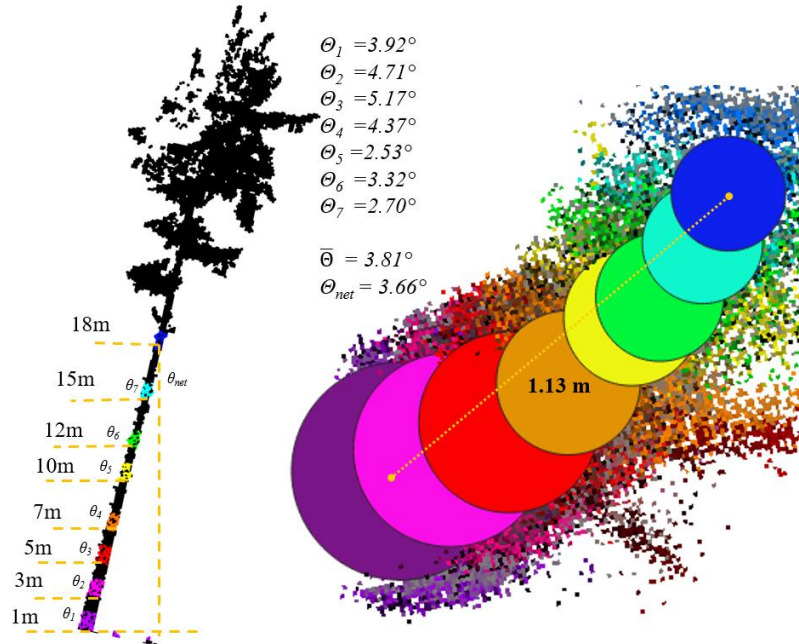


Figure 4-3 Graphic representation of the relationship between the two ways that tree lean was measured in this study. Circular vectors were fit to rasterized slices of point clouds at locations along the stems. The total lean of the tree, ( $\theta_{net}$ ) was calculated using the horizontal displacement of the stem centroid from 1 to 18 meters, while the average lean ( $\bar{\theta}$ ) was calculated as the mean of 7 sectional lean estimates ( $\theta_1$  to  $\theta_7$ ) between consecutive centroids. The values in the figure are real values from one of the sampled trees, but the lean angle of the tree is exaggerated for display.

To compare the DBH field measurements with digital the DBH estimates and the two lean estimates I have used simple linear regression (Eq.3):

$$\begin{aligned}
 DBH_{2020} &= b_0 + b_1 \times DBH_{MLS2018} \\
 \bar{\theta} &= b_0 + b_1 \times \theta_{net}
 \end{aligned}
 \tag{3}$$

where  $DBH_{2020}$  and  $DBH_{MLS2018}$  are the DBH measured in 2020 or estimated from the slice starting at 1 m

$b_0$  and  $b_1$  are parameters of the simple linear regression

All regression visualizations were constructed using the package ‘ggplot2’ in R (Wickham, 2016).

To estimate the actual volume of the trees, I have summed the volume of each section and the volume of the top of the tree. For the sections between 1m and 18m, the volume (V) was computed assuming that the stem is a frustum of a cone:

$$V = \frac{\pi h}{3} (R_1^2 + R_1 * R_2 + R_2^2) \quad 4$$

where  $R_1$  and  $R_2$  are the radius of the bottom and top slices defining the stem section

Stem sections below 1 m, (i.e., stumps) were accounted for by calculating the volume of a 1 m tall cylinder with a diameter equal to the estimated diameter at 1m. For the top part of the tree, namely above 18 m, the volume was calculated assuming two different geometries (i.e., cone and paraboloid), and using as the base diameter the diameter at 18 m and as height the difference between the total height and 18 m.

Trees were classified as leaning or non-leaning using a threshold of  $2^\circ$  according to the estimated total lean ( $\theta_{net}$ ), which is a conservative estimate compared to average lean (Figure 4-4).

#### 4.2.4. Stem Modeling

The estimated diameters along the stems, their associated heights, and the total tree heights measured from the UALS were used to calibrate existing stem taper and volume equations that have previously been applied to DF (**Error! Reference source not found.**). The chosen equations were limited to use at most four parameters, considering that for each tree only eight diameters were measured. For predicting stem taper, the response variable for all the equations is  $d_h$ , the stem diameter at height  $h$  ( $0 < h < H$ ). The equations also share the same predictor variables, for taper the DBH, the total height of the tree ( $H$ ), and the height of  $d_h$  ( $h$ ), whereas for volume the DBH and total height. However, the models differ in terms of form, which defines their performance. For predicting total tree volume ( $V$ ), I have tested three models: one developed by Poudel et al. (Poudel et al., 2018), henceforth PT, one derived from the tariff tree volume equations of Brackett (Brackett, 1977) for DF in the western Oregon and Washington (BR1), and one that is a simplified non-linear version of Brackett's equation (BR2). For the BR1 models, the Brackett (1977) equation was used as written, (i.e., with fixed values for coefficients), except the intercept term was converted to a variable parameter with the original value as the starting

point. To create the BR2 equation, all of the coefficients were converted to variable parameters, then I removed them according to nonsignificant t-values ( $\Pr(<|t|) \leq 0.01$ ) until only significant parameters remained.

Table 4-1: Stem diameter taper and total tree volume equations used in this study. The residuals are represented by  $e$ .

Citation	Abbreviation	Equation	Shorthand
(Amidon, 1984)	AMI	$d_h = a_1 D \left( \frac{H-h}{H-1.37} \right) + a_2 \frac{(H^2-h^2)(H-1.37)}{H^2} + e$	$f_{AMI}(D, H, h)$
(Biging, 1984)	BIG	$d_h = D[a_1 + a_2 \ln(1 - \lambda \left(\frac{h}{H}\right)^m)] + e$ where $\lambda = 1 - \exp\left(\frac{-a_1}{a_2}\right)$ and $m = \frac{1}{3}$	$f_{BIG}(D, H, h)$
(Kozak et al., 1969)	KOZ	$d_h = \sqrt{D(a_1 \frac{(h-H)}{H} + a_2 \frac{(h^2-H^2)}{H^2})} + e$	$\sqrt{f_{KOZ}(D, H, h)}$
(Max and Burkhart, 1976) (simplified)	MAB	$d_h = D * (a_1(R-1) + a_2(R^2-1) + a_3(a_4-R)^2) + e$ where $R = \frac{h}{H}$	$f_{MAB}(D, H, h)$
Brackett (1977)	BR1	$V = 10^{\{a_1+0.05 \log(H) \log(D)+0.16(\log(D))^2+1.63(\log(H))+0.16(\log(H))^2+e\}}$	$10^{f_{BR1}(D,H)}$
(Brackett, 1977) (simplified)	BR2	$V = 10^{\{a_1+a_2 \log(H) \log(D)+a_3(\log(H))+e\}}$	$10^{f_{BR2}(D,H)}$
(Poudel et al., 2018)	POU	$V = \exp(a_1 + a_2 \ln(D) + a_3 \ln(H) + e)$	$\exp(f_{POU}(D, H))$

To test impact of the lean model fit, I separated the trees into two classes: vertical (i.e.,  $\Theta_{net} < 2^\circ$ ) and leaning (i.e.,  $\Theta_{net} \geq 2^\circ$ ). Because point clouds offer the opportunity to use different stem diameters instead of DBH, I have investigated how changing the location of the fixed height diameter variable ( $Dx$ , where  $x$  is the base height of the slice) would affect the models. Lean angle in radians was initially included as a predictor in the models without any transformations, but the results were not encouraging, so, many nonlinear transformations of lean were tested via trial-and-error to improve the

existing equations. As a result, the transformation  $\Theta_{net}^{-0.5}$  lead to significant improvements of the models **(Error! Reference source not found.)**.

Considering that the trees were not described with point clouds surrounding them, but with circular sector larger than  $180^\circ$ , a situation avoided in the terrestrial laser scans, I considered that the position of the scanner in respect with the tree could play a role in estimation. A possible variable that describes the relationship between the tree and sensor is the minimum distance between the tree and sensor. A similar, trial-and-error based modeling procedure was conducted using the minimum distance between the scanner and the stem centroid of the slice starting at 1 m ( $T$ ) as a predictor. The transformation  $T \sim \ln^2(T)$  led to significant improvements of the models **(Error! Reference source not found.)**.

Models were adjusted by including both  $\Theta_{net}^{-0.5}$  and  $\ln^2(T)$  separately and together. However, the addition of the  $\ln^2(T)$  alone resulted in little or no improvement. As a result, I only present the results of the original models, those adjusted by expressing the lean ( $\Theta_{net}^{-0.5}$ ), and those adjusted by expressing both the lean and the distance between the tree and sensor ( $\ln^2(T)$ ).

For the equations predicting volume  $V$ , I have tested both representations of the upper part of the tree, namely conoid ( $V_c$ ) and paraboloid ( $V_p$ ). Similar to the stem taper models, I tested the volume models on leaning and non-leaning trees separately. To assess the impact of changing the DBH with another diameter along the stem on computing the volume, I have used the model of Poudel et al (Poudel et al., 2018), as being developed using trees close to the study area. In this case, the DBH was replaced with the diameter from each of the eight slices,  $D_x$ .

Table 4-2: Modified versions of existing nonlinear stem taper and volume equations modified to include lean and distance from scanner as predictors.

Response	Equation	Including Lean	Including Lean and Distance
Diameter	AMI	$d_h = f_{AMI}(D, H, h) + \frac{b_1}{\sqrt{(\Theta_{net})}} + e$	$d_h = f_{AMI}(D, H, h) + \frac{b_1}{\sqrt{(\Theta_{net})}} + \frac{b_2}{\ln(T)} + e$

Response	Equation	Including Lean	Including Lean and Distance
	BIG	$d_h = f_{BIG}(D, H, h) + \frac{b_1}{\sqrt{(\Theta_{net})}} + e$	$d_h = f_{BIG}(D, H, h) + \frac{b_1}{\sqrt{(\Theta_{net})}} + \frac{b_2}{\ln(T)} + e$
	KOZ	$d_h = \sqrt{f_{KOZ}(D, H, h) + \frac{b_1}{\sqrt{(\Theta_{net})}} + e}$	$d_h = \sqrt{f_{KOZ}(D, H, h) + \frac{b_1}{\sqrt{(\Theta_{net})}} + \frac{b_2}{\ln(T)} + e}$
	MAB	$d_h = f_{MAX}(D, H, h) + \frac{b_1}{\sqrt{(\Theta_{net})}} + e$	$d_h = f_{MAX}(D, H, h) + \frac{b_1}{\sqrt{(\Theta_{net})}} + \frac{b_2}{\ln(T)} + e$
Volume	BR1	$V = 10^{\{f_{BR1}(D,H) + \frac{b_1}{\sqrt{(\Theta_{net})}} + e\}}$	$V = 10^{\{f_{BR1}(D,H) + \frac{b_1}{\sqrt{(\Theta_{net})}} + \frac{b_2}{\ln(T)} + e\}}$
	BR2	$V = 10^{\{f_{BR2}(D,H) + \frac{b_1}{\sqrt{(\Theta_{net})}} + e\}}$	$V = 10^{\{f_{BR2}(D,H) + \frac{b_1}{\sqrt{(\Theta_{net})}} + \frac{b_2}{\ln(T)} + e\}}$
	POU	$V = \exp(f_{POU}(D, H) + \frac{b_1}{\sqrt{(\Theta_{net})}} + e)$	$V = \exp(f_{POU}(D, H) + \frac{b_1}{\sqrt{(\Theta_{net})}} + \frac{b_2}{\ln(T)} + e)$

To ensure correctness of the models, I have tested the normality of the residuals with the Shapiro-Wilk test, the heteroscedasticity with the Breush-Pagan test, and the autocorrelation of the residuals with the Durbin –Watson test. In the case when an assumption is violated, I have evaluated its impact by investigating the distribution of the residuals. If the residuals do not follow a normal distribution, but one that is unimodal with limited skewness, I considered that the departure is produced by the sample. Therefore, the results were valid. The violation of the heteroscedasticity assumptions indicates that the confidence intervals of the results are wider than they should be. However, because I did not develop a model, just used existing one, I considered the lack of variance homogeneity also an artifact due to the sample. If autocorrelation is present, I have developed a second order autoregressive equation that has the residuals distributed as white noise:

$$e_h = c_0 + c_1 \times e_{h-1} + c_2 \times e_{h-2} + \varepsilon_h$$

5

where  $e_h$  is the error of the model,

$c_0, c_1, c_2$  are coefficients to be estimated, and

$\varepsilon_h$  is white noise.

The nonlinear regression analysis was performed using the Gauss-Newton algorithm with a maximum of 100 iterations, and a minimum step size of  $2^{-10}$ . The regression modeling was executed with the ‘stats’ package in R. To compare the models I have computed the bias, RMSE, coefficient of determination ( $R^2$ ), Akaike Information Criterion (AIC) (Akaike, 1987), and Bayesian Information Criterion (BIC) (Schwarz, 1978). The main criterion for differentiating the models were bias, followed by AIC, BIC, RMSE, and  $R^2$

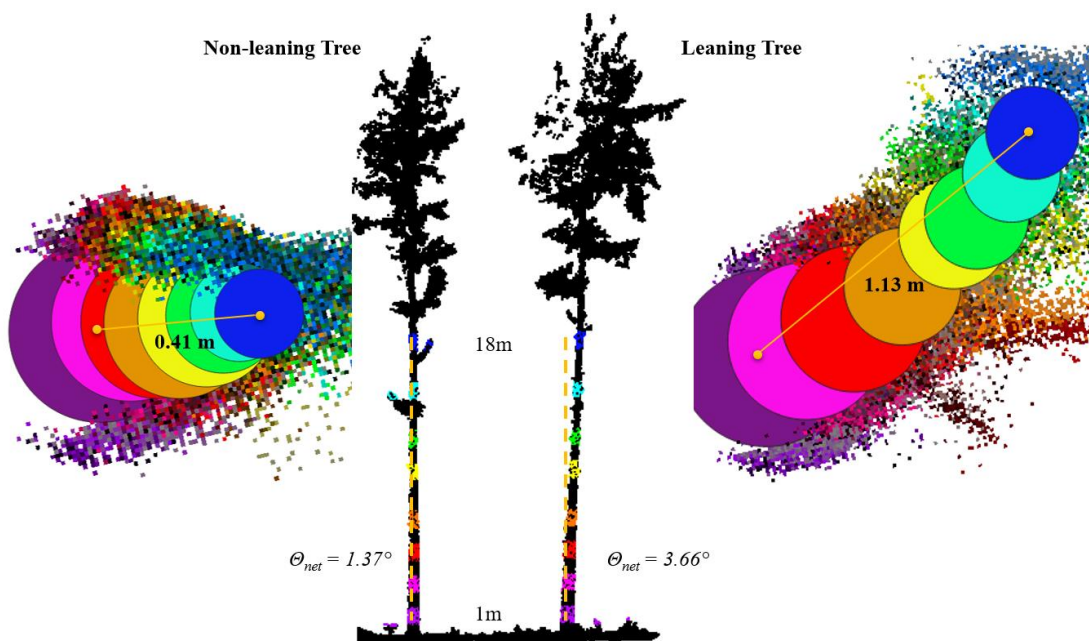


Figure 4-4: Example of two adjacent trees classified as leaning (right) or non-leaning (left) based on a  $2^\circ$  threshold. The rendered trees in the center of the image are shown from a profile perspective with the horizontal point cloud slices in color (1m (purple), 3m (pink), 5m (red), 7m (orange), 10m (yellow), 12m (green), 15m (cyan), and 18m (blue)). Corresponding colored circular vectors from the same non-leaning (left) and leaning (right) trees from a nadir view shown on the outside of the image

## 4.3. Results

### 4.3.1. Diameter and Lean Estimates

Though the MLS laser has a range of 120m, several factors cause the limit for stem modeling to be considerably less, including the angle of the scanner, trees obstructing one another, and understory vegetation. Empirically, 40 m was determined to be the approximate limit in this case, though I included one tree that was slightly farther away ( $T = 41.68\text{m}$ ). The stem centers of 273 trees located from the same MLS data in Chapter 2 were inspected, and of those, 191 could be fit circles at 1m, and 163 were fit in the raster slices at all 8 heights. Four trees were removed because they were understory maple (*Acer sp.*) trees, so 159 trees remained in the sample. Of those, 40 trees (25%) were leaning according to  $\theta_{net} > 2^\circ$ , while the remaining 119 (75%) were considered vertical. If  $\bar{\Theta}$  had been used for classification rather than  $\theta_{net}$ , 57 trees (35.8%) would be considered leaning. Considering that the allowable error for heights measured with on the ground instruments is 10% (Robertson, 2000), nearly an order of magnitude greater, there is evidence that the heights measured from the UALS, hereafter H, are reliable and appropriate for use in modeling. Summary statistics for total height (H),  $D_1$ , T,  $V_p$ ,  $V_c$ ,  $\theta_{net}$ , and  $\bar{\Theta}$  are given in Table 3 for the entire sample, as well as for leaning and non-leaning trees

The 90 DBH measured in 2020 were correlated with the diameters at one meter ( $D_1$ ) estimated from the 2018 MLS scan ( $R^2=0.93$ ) and the RMSE between the measurements was 4.0 cm (Figure 4-5). The average ground measured DBH was 73.01 cm (standard deviation= 14.23). For the same 90 trees, the average DBH estimate from the MLS was 63.77cm (standard deviation = 14.66). Therefore, the mean ground DBH was about 14% (9.24cm) larger than the mean MLS estimated diameter from 2 years prior, and RMSE was 6.27% (4 cm) of the average diameter from 2018

Table 4-3: Summary statistics for total height (H), diameter at 1 meter ( $D_1$ ), distance to tree (T), volume with paraboloid top ( $V_p$ ), volume with conoid top ( $V_c$ ), total lean ( $\theta_{net}$ ), and average lean ( $\bar{\theta}$ ) for the entire sample (n=159), as well as for trees that were considered as leaning (n=40) or non-leaning (n=119) according to the total lean angle,  $\theta_{net}$ , and a  $2^\circ$  cutoff.

Sample	n	Variable	Min	Max	Mean	Std. Dev.
All Trees	159	H	36.21	49.74	43.13	2.95
	159	$D_1$	0.29	1.04	0.59	0.14
	159	T	4.28	41.68	18.83	8.77
	159	$V_p$	0.81	11.05	3.57	1.84
	159	$V_c$	0.73	9.61	3.12	1.58
	159	$\theta_{net}$	0.07	3.66	1.51	0.81
	159	$\bar{\theta}$	0.50	3.85	1.82	0.77
Vertical	119	H	36.42	49.74	43.20	2.93
	119	$D_1$	0.29	1.04	0.60	0.14
	119	T	4.28	41.68	18.75	8.90
	119	$V_p$	0.81	11.05	3.64	1.93
	119	$V_c$	0.73	9.61	3.18	1.65
	119	$\theta_{net}$	0.07	1.98	1.13	0.48
	119	$\bar{\theta}$	0.50	2.44	1.46	0.45
Leaning	40	H	36.21	48.66	42.94	2.99
	40	$D_1$	0.33	0.91	0.59	0.13
	40	T	5.55	34.80	19.10	8.35
	40	$V_p$	1.07	7.41	3.35	1.53
	40	$V_c$	0.95	6.38	2.95	1.32
	40	$\theta_{net}$	2.03	3.66	2.64	0.47
	40	$\bar{\theta}$	2.20	3.85	2.89	0.49
Ground Truth	90	DBH	0.39	1.02	0.73	0.14
	90	T	4.28	33.05	15.24	6.89

Fitting the circles to the stem locations takes around 55 minutes per height, so one circle is executed on average in 21 seconds and the entire process lasted about 8 hours. The circle fitting activity was the most time-consuming step in the data extraction. The taper extracted from the circles (**Error! Reference source not found.**), revealed no instances when the diameter increases with height, which would have triggered an individual assessment of that measurement.

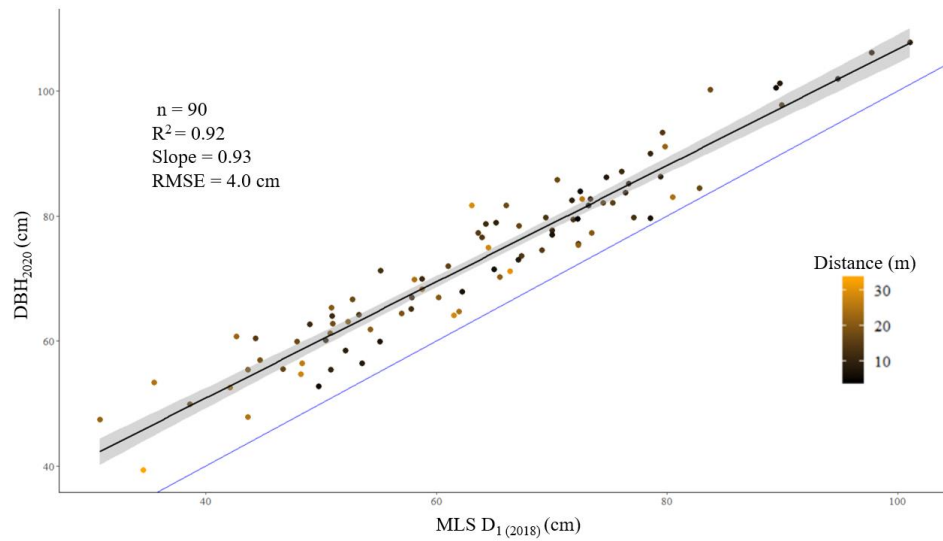


Figure 4-5: Comparison of D<sub>1</sub> estimates from MLS point cloud data collected in March 2018 versus manual DBH measurements from April 2020.

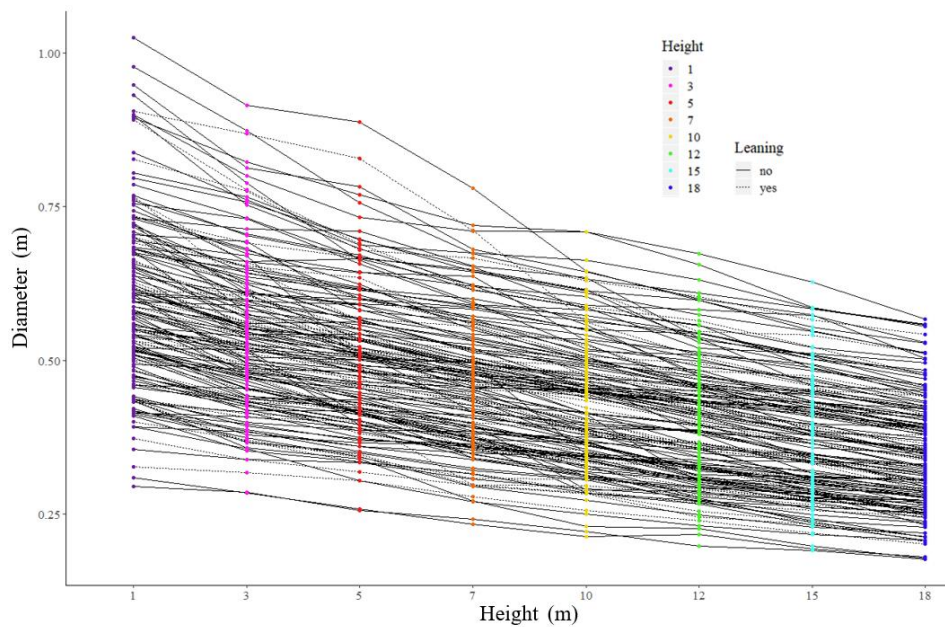


Figure 4-6: Stem diameter estimates from MLS point cloud data sliced at 8 locations between 1 and 18 meters above ground. Point colors correspond with heights of point cloud slices, while polylines represent individual trees and the line type represents whether trees were calculated as leaning or non-leaning.

The two methods we used to estimate tree lean, average lean ( $\bar{\theta}$ ) and total lean ( $\theta_{net}$ ), were correlated ( $R^2 = 0.93$ ), and had an RMSE of  $0.22^\circ$ . The values for  $\theta_{net}$  were consistently smaller than  $\bar{\theta}$ , ( $1.53^\circ$  and  $1.82^\circ$ , respectively), as well as the distribution of the points in the scatterplot (Figure 4-7). The slope of the linear regression line was 0.93.

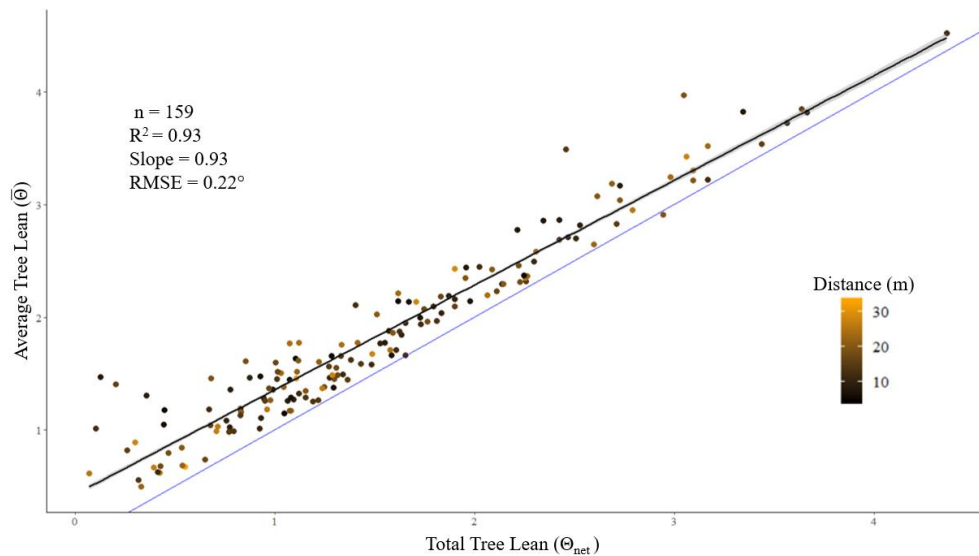


Figure 4-7: Scatterplot showing total tree lean ( $\theta_{net}$ ) versus average tree lean ( $\bar{\theta}$ ) for 159 mature Douglas firs.

### 4.3.2. Taper Modeling

The taper models used in the study were not tailored to the data. Therefore, it is expected that some of the modeling requirements are not met, particularly independence. All taper models, applied in the original form, had prediction bias  $< 0.3$  cm (**Error! Reference source not found.**), which is 0.07% relative to the mean DBH of 45.7 cm (std. deviation = 13.7 cm). When the original equations were fit using all trees, the BIG and MAB models had the least error (RMSE = 3.9 cm), followed by KOZ (RMSE = 4.1 cm), then AMI (RMSE = 4.2 cm). When only the vertical trees were modeled, the error and bias were similar, not only among the four equations, but also with the case when all the trees were considered. (RMSE and bias of  $0.042\text{m}$  and  $0.002\text{m}$  for AMI,  $0.039\text{m}$  and  $0.002\text{m}$  for BIG,  $0.041\text{m}$  and  $0.002\text{m}$  for KOZ, and  $0.039\text{m}$  and  $<0.0001$  for MAB, respectively). For leaning trees, three out of the four models presented a larger bias than for the case when all the trees were considered (i.e., bias of

0.003m vs. 0.002m for AMI, BIG, and KOZ). All the models exhibit lack of independence, as Durbin – Watson revealed (p-value <0.01 for height lags up to three). The autocorrelation model with two lag terms (Eq. 5) supplied a model that has uncorrelated errors (condition for independence of the residuals), which also eliminate the bias. Irrespective of the taper model, both lag terms were significant (p-value <0.01).

When the models were adjusted by including  $\Theta_{net}$  to model the leaning trees, all four equations exhibited an increase in  $R^2$  (i.e., 0.907 vs. 0.899 for AMI, 0.948 vs. 0.944 for BIG, 0.911 vs. 0.906 for KOZ, and 0.914 vs. 0.912 for MAB) and three manifested a reduction in bias (i.e., <0.001 vs. 0.003 for AMI, BIG, and KOZ) and RMSE (i.e., 0.039 vs 0.042 for AMI, 0.037 vs. 0.039 for BIG, and 0.038 vs. 0.041 for KOZ).

For all trees or vertical trees, adjusting the equations by adding  $\Theta_{net}$  and distance to tree (T) made little to no difference on the model fit, with the RMSE values remaining unchanged in the adjusted models compared to the originals. However, for leaning trees, the addition of lean reduced the error for AMI (-7.1%), BIG (-5.1%), and KOZ (-7.3%), though for MAB the error was unchanged. The inclusion of distance to the sensor resulted in slightly lower RMSE values for modeling the non-leaning trees with the AMI equation (-2.4%), and for modeling the leaning trees with BIG (-2.7%). However, the AMI and KOZ model exhibited convergence difficulties when the distance to the sensor was present.

Substitution of  $D_5$  for DBH generally improved the fit of all four diameter equations across models fit using all trees and vertical trees. However, when  $D_5$  was used to model leaning trees, the inclusion of lean in the models reduced the error of only two of the four of the equations: AMI (-2.8%) and KOZ (-2.9%), as the RMSE for BIG and MAB did not change. When T was included as a predictor for the models using  $D_5$ , the coefficient was significant and increased the fit of all four models, which was surprising because the same adjustment caused nonconvergence in the models when DBH was used.

Table 4-4 Results from non-linear models predicting stem taper. Probability values ( $P(>|t|)$ ) with † had a nonsignificant ( $\alpha = 0.01$ )parameter from the original model (i.e.,  $a_1, a_2, \dots$ ) though the model was significant overall. Cells with “—” failed to converge.

Equation	Sample	n	Adjustment	P(> t )		Bias (m)		RMSE (m)		AIC		BIC		R <sup>2</sup>	
				DBH	D5	DBH	D5	DBH	D5	DBH	D5	DBH	D5	DBH	D5
AMI	Vertical (< 2°)	119	-	<0.001	<0.001	0.002	0.001	0.042	0.032	-2930	-3372	-2916	-3358	0.911	0.947
		119	$\Theta_{net}$	0.324	0.031	0.002	<0.001	0.042	0.032	-2929	-3375	-2910	-3356	0.911	0.947
		119	$\Theta_{net} + T$	0.015	0.001	0.002	<0.001	0.041	0.032	-2929	-3375	-2905	-3352	0.911	0.947
	Leaning (> 2°)	40	-	<0.001	<0.001	0.003	0.001	0.042	0.036	-976	-1059	-965	-1048	0.899	0.923
		40	$\Theta_{net}$	<0.001	<0.001	<0.001	<0.001	0.039	0.035	-1010	-1076	-995	-1061	0.907	0.926
		40	$\Theta_{net} + T$	--	0.005	--	<0.001	--	0.035	--	-1076	--	-1058	--	0.927
	All	159	-	<0.001	<0.001	0.002	0.001	0.042	0.033	-3909	-4425	-3894	-4410	0.908	0.941
		159	$\Theta_{net}$	0.023	0.001	0.002	0.001	0.042	0.033	-3913	-4434	-3893	-4414	0.908	0.941
		159	$\Theta_{net} + T$	0.364	<0.001	0.002	<0.001	0.042	0.033	-3911	-4440	-3886	-4415	0.908	0.942
BIG	Vertical (< 2°)	119	-	<0.001	<0.001	0.002	<0.001	0.039	0.030	-3019	-3485	-3005	-3470	0.940	0.962
		119	$\Theta_{net}$	0.356	0.171	0.002	<0.001	0.039	0.030	-3018	-3484	-2999	-3466	0.940	0.962
		119	$\Theta_{net} + T$	<0.001	0.045	0.001	<0.001	0.039	0.030	-3036	-3484	-3012	-3463	0.941	0.962
	Leaning (> 2°)	40	-	<0.001	<0.001	0.003	0.001	0.039	0.033	-1016	-1104	-1005	-1093	0.944	0.946
		40	$\Theta_{net}$	<0.001	<0.001	<0.001	0.001	0.037	0.033	-1045	-1104	-1031	-1093	0.948	0.946
		40	$\Theta_{net} + T$	<0.001	0.323	<0.001	<0.001	0.036	0.032	-1055	-1114	-1037	-1096	0.950	0.950
	All Trees	159	-	<0.001	<0.001	0.002	<0.001	0.039	0.031	-4036	-4579	-4021	-4564	0.941	0.958
		159	$\Theta_{net}$	0.024	0.011	0.002	<0.001	0.039	0.031	-4039	-4584	-4019	-4564	0.940	0.958
		159	$\Theta_{net} + T$	<0.001	0.001	0.001	<0.001	0.039	0.031	-4053	-4592	-4028	-4567	0.941	0.958
KOZ	Vertical (< 2°)	119	-	<0.001	<0.001	0.002	0.001	0.041	0.032	-2952	-3379	-2938	-3364	0.914	0.947
		119	$\Theta_{net}$	0.225	0.089	0.002	<0.001	0.041	0.032	-2951	-3379	-2932	-361	0.914	0.947

		119	$\Theta_{net} + T$	<0.001	<0.001	0.002	<0.001	0.041	0.032	-2954	-3382	-2930	-3358	0.914	0.948
Leaning (> 2°)		40	-	<0.001	<0.001	0.003	0.001	0.041	0.035	-991	-1075	-980	-1064	0.906	0.927
		40	$\Theta_{net}$	<0.001	<0.001	<0.0001	<0.001	0.038	0.034	-1022	-1088	-1007	-1073	0.911	0.929
		40	$\Theta_{net} + T$	--	<0.001	--	<0.001	--	0.034	--	-1088	--	-1069	--	0.930
All Trees		159	-	<0.001	<0.001	0.002	<0.001	0.041	0.033	-3945	-4447	-3930	-4432	0.912	0.942
		159	$\Theta_{net}$	0.012	0.005	0.002	<0.001	0.041	0.033	-3949	-4453	-3929	-4433	0.911	0.944
		159	$\Theta_{net} + T$	0.010	<0.001	0.002	<0.001	0.041	0.032	-3949	-4461	-3924	-4436	0.911	0.943
MAB	Vertical (< 2°)	119	-	<0.001 <sup>†</sup>	<0.001 <sup>†</sup>	<0.0001	<0.001	0.039	0.030	-3017	-3469	-2993	-3446	0.919	0.953
		119	$\Theta_{net}$	0.024	0.424	<0.0001	<0.001	0.039	0.030	-3020	-3468	-2992	-3440	0.919	0.953
		119	$\Theta_{net} + T$	0.039	0.002	<0.0001	<0.001	0.039	0.030	-3019	-3469	-2986	-3435	0.919	0.953
	Leaning (> 2°)	40	-	0.020	0.922	<0.0001	<0.001	0.038	0.033	-1025	-1100	-1007	-1082	0.912	0.933
		40	$\Theta_{net}$	0.024	0.003	<0.0001	<0.001	0.038	0.033	-1028	-1107	-1006	-1085	0.914	0.935
		40	$\Theta_{net} + T$	--	<0.001	--	<0.001	--	0.033	--	-1108	--	-1083	--	0.936
	All Trees	159	-	<0.001 <sup>†</sup>	<0.001 <sup>†</sup>	<0.0001	<0.001	0.039	0.031	-4044	-4565	-4019	-4539	0.917	0.948
		159	$\Theta_{net}$	0.207	0.107	<0.0001	<0.001	0.039	0.031	-4044	-4565	-4014	-4535	0.917	0.948
		159	$\Theta_{net} + T$	0.990	<0.001	<0.0001	<0.001	0.039	0.031	-4042	-4570	-4006	-4535	0.917	0.948

### 4.3.3. Volume Modeling

Irrespective the type of trees considered in modeling (i.e., vertical, leaning, or all), the BR1 volume model showed over an order of magnitude more bias (0.174-0.289 m<sup>3</sup>) than the other two models ( $\leq 0.015$  m<sup>3</sup> for BR2 and POU) and had the highest error (RMSE=0.71m<sup>3</sup> vs. 0.492 m<sup>3</sup> and 0.494 m<sup>3</sup> for BRA2 and POU, respectively) (**Error! Reference source not found.**). Considering that the mean stem f or all trees was 3.57m<sup>3</sup>, the maximum relative bias was 0.4% for BR2 and POU, and 8.1% for BR1 when predicting  $V_p$  (**Error! Reference source not found.**). When the original models were fit using all trees, the BR2 and POU equations had the least error (RMSE=0.61m<sup>3</sup>, followed by BR1 with RMSE=0.83m<sup>3</sup>) and the strongest correlations ( $R^2 = 0.888$  for BR2 and POU, and 0.874 for BR1). The model using BR2 was slightly less biased than the model using POU for all trees (bias = 0.003 for BR2 and 0.007 for POU). As did the taper models, the volume models exhibited autocorrelation (Durbin-Watson test had p-values <0.01). Mirroring the results from taper, the autoregressive volume equations contains two significant terms.

Compared fitting the models using all the trees, all the equations produced models with less error (RMSE 0.775 vs. 0.828 for BR1, 0.558 vs 0.616 for BR2, and 0.566 vs 0.616 for POU), but with greater bias for BR2 (0.005 vs 0.004) and POU (0.008 vs. 0.007), and weaker correlations for all three equations ( $R^2$  of 0.840 vs. 0.874 for BR1, 0.866 vs. 0.888 for BR2, and 0.862 vs. 0.888 for POU) when fit to only the leaning trees. When  $\Theta_{net}$  was included as a predictor for  $V_p$  for modeling leaning trees, the bias was reduced for all three equations (bias 0.230 vs. 0.241 for BR1, 0.004 vs 0.005 for BR2, and 0.007 vs. 0.008 for POU). The errors were also reduced (RMSE 0.751 vs 0.775 for BR1, 0.548 vs. 0.558 for BR2, and 0.554 vs. 0.566 for POU), as were the AIC (731 vs. 749 for BR1, 533 vs. 543 for BR2, and 0.540 vs. 552 for POU) and BIC (743 vs. 757 for BR1, 552 vs. 558 for BR2, and 559 vs. 567 for POU), while the correlations were stronger ( $R^2$  0.848 vs. 0.840 for BR1, 0.871 vs. 0.866 for BR2, and 0.868 vs. 0.862 for POU).

When models were fit using only the vertical trees, including  $\Theta_{net}$  as a predictor also resulted in lower bias for all three equations (0.284 vs. 0.289 for BR1, 0.004 vs. 0.007 for BR2, and 0.007 vs 0.009 for POU), as well as lower AIC(2359 vs. 2384 for BR1, 1758 vs. 1789 for BR2, and 1787 vs. 1813 for POU), lower BIC (2373 vs 2394 for BR1, 1783 vs. 1809 for BR2, and 1811 vs. 1832 for POU), and stronger correlations(0.884 vs. 0.881 for BR1, 0.901 vs 0.898 for BR2, and 0.898 vs 0.895 for POU). In the case of the vertical trees the margins of the improvement (i.e., gains in model fit) that resulted by including  $\Theta_{net}$  as a predictor were smaller than for the leaning trees, but still present and consistent across the models.

When DBH was replaced with diameter at 5 meters ( $D_5$ ) in the models predicting  $V_p$ , the models improved for all 3 equations, but they improved by a larger proportion according to RMSE and bias for models fit using the vertical trees compared to the leaning trees. Distance to tree (T) was not a significant predictor when using DBH for any of the models, though for models using  $D_5$  including T resulted in improvements for only the leaning trees for two of the models (BR1 and POU), and for modeling all trees with two of the models (BR2 and POU).

The model results for equations predicting total stem volume with a conic top ( $V_c$ ) are shown in Table 6. Here, the patterns observed when modeling  $V_p$  are still present, though the models for  $V_c$  tended to be slightly less biased, have less error, and have stronger correlation coefficients than the models predicting  $V_p$ .

Table 4-5: Results from nonlinear models predicting total stem volume where the portion of the stem above 18 meters was approximated as a paraboloid.

Equation	Sample	n	Adjustment	P(> t )		Bias		RMSE		AIC		BIC		R <sup>2</sup>	
				DBH	D5	DBH	D5	DBH	D5	DBH	D5	DBH	D5	DBH	D5
BR1	Vertical ( $< 2^\circ$ )	119	-	<0.001	<0.001	0.289	0.200	0.845	0.564	2384	1614	2394	1624	0.881	0.952
		119	$\Theta_{net}$	<0.001	0.731	0.284	0.200	0.833	0.564	2359	1616	2373	1630	0.884	0.952
		119	$\Theta_{net} + T$	--	--	--	--	--	--	--	--	--	--	--	--
	Leaning ( $> 2^\circ$ )	40	-	<0.001	<0.001	0.241	0.205	0.775	0.693	749	677	757	685	0.840	0.868
		40	$\Theta_{net}$	<0.001	<0.001	0.230	0.185	0.751	0.638	731	626	743	638	0.848	0.887
		40	$\Theta_{net} + T$	--	<0.001	--	0.174	--	0.607	--	596	--	611	--	0.897
	All Trees	159	-	<0.001	<0.001	0.278	0.201	0.828	0.599	3133	2309	3144	2319	0.874	0.937
		159	$\Theta_{net}$	<0.001	0.440	0.273	0.201	0.820	0.599	3111	2310	3126	2326	0.875	0.937
		159	$\Theta_{net} + T$	--	--	--	--	--	--	--	--	--	--	--	--
BR2	Vertical ( $< 2^\circ$ )	119	-	<0.001	<0.001	0.004	0.010	0.617	0.399	1789	962	1809	982	0.898	0.957
		119	$\Theta_{net}$	<0.001	0.672	0.007	0.010	0.606	0.399	1758	964	1783	988	0.901	0.957
		119	$\Theta_{net} + T$	--	--	--	--	--	--	--	--	--	--	--	--
	Leaning ( $> 2^\circ$ )	40	-	<0.001	<0.001	-0.005	-0.015	0.558	0.524	543	502	558	517	0.866	0.883
		40	$\Theta_{net}$	<0.001	<0.001	-0.004	-0.012	0.548	0.501	533	476	552	495	0.871	0.893
		40	$\Theta_{net} + T$	--	--	--	--	--	--	--	--	--	--	--	--
	All Trees	159	-	<0.001	<0.001	0.003	0.003	0.616	0.462	2385	1653	2406	1673	0.888	0.937
		159	$\Theta_{net}$	<0.001	<0.001	0.004	0.003	0.617	0.459	1789	1640	1809	1666	0.898	0.938
		159	$\Theta_{net} + T$	--	<0.001	--	0.003	--	0.458	--	1637	--	1668	--	0.938
POU	Vertical ( $< 2^\circ$ )	119	-	<0.001	<0.001	-0.009	0.005	0.624	0.384	1813	890	1832	909	0.895	0.960
		119	$\Theta_{net}$	<0.001	0.629	-0.007	0.005	0.615	0.384	1787	892	1811	916	0.898	0.960
		119	$\Theta_{net} + T$	--	--	--	--	--	--	--	--	--	--	--	--
	Leaning ( $> 2^\circ$ )	40	-	<0.001 <sup>†</sup>	<0.001	-0.008	-0.015	0.566	0.513	552	489	567	504	0.862	0.888
		40	$\Theta_{net}$	<0.001 <sup>†</sup>	<0.001	-0.007	-0.011	0.554	0.483	540	452	559	471	0.868	0.900
		40	$\Theta_{net} + T$	--	<0.001	--	-0.009	--	0.468	--	434	--	457	--	0.906
	All Trees	159	-	<0.001	<0.001	-0.007	-0.001	0.616	0.440	2387	1528	2407	1548	0.888	0.943
		159	$\Theta_{net}$	0.005	0.002	-0.006	-0.001	0.614	0.438	2380	1520	2405	1545	0.888	0.943
		159	$\Theta_{net} + T$	--	<0.001	--	-0.001	--	0.438	--	1519	--	1550	--	0.943

Table 4-6: Results from nonlinear models predicting total stem volume, where the portion of the stem above 18 meters was approximated as a cone. Probability values ( $P(>|t|)$ ) with † had a nonsignificant ( $\alpha = 0.01$ ) parameter from the original model (i.e.,  $a_1, a_2, \dots$ )

Equation	Sample	n	Adjustment	P(> t )		Bias		RMSE		AIC		BIC		R <sup>2</sup>	
				DBH	D5	DBH	D5	DBH	D5	DBH	D5	DBH	D5	DBH	D5
BR1	Vertical (< 2°)	119	-	<0.001	<0.001	0.265	0.190	0.726	0.497	2097	1374	2106	1384	0.890	0.955
		119	$\Theta_{net}$	<0.001	0.529	0.262	0.190	0.717	0.497	2073	1376	2088	1390	0.893	0.955
		119	$\Theta_{net} + T$	--	--	--	--	--	--	--	--	--	--	--	--
	Leaning (> 2°)	40	-	<0.001	<0.001	0.215	0.182	0.656	0.579	642	563	650	570	0.857	0.886
		40	$\Theta_{net}$	<0.001	<0.001	0.206	0.166	0.637	0.535	626	514	637	525	0.864	0.902
		40	$\Theta_{net} + T$	--	<0.001	--	0.156	--	0.507	--	481	--	496	--	0.912
	All Trees	159	-	<0.001	<0.001	0.254	0.189	0.710	0.519	2741	1945	2751	1955	0.884	0.943
		159	$\Theta_{net}$	<0.001	0.511	0.250	0.189	0.703	0.519	2718	1947	2734	1962	0.886	0.943
		159	$\Theta_{net} + T$	--	--	--	--	--	--	--	--	--	--	--	--
BR2	Vertical (< 2°)	119	-	<0.001	<0.001	0.002	0.008	0.494	0.310	1365	480	1385	499	0.910	0.965
		119	$\Theta_{net}$	<0.001	0.328	0.005	0.008	0.485	0.310	1334	481	1358	505	0.913	0.965
		119	$\Theta_{net} + T$	--	--	--	--	--	--	--	--	--	--	--	--
	Leaning (> 2°)	40	-	<0.001	0.002	-0.004	-0.013	0.444	0.415	397	354	412	369	0.887	0.902
		40	$\Theta_{net}$	<0.001	<0.001	-0.003	-0.011	0.436	0.398	387	328	406	347	0.891	0.910
		40	$\Theta_{net} + T$	--	--	--	--	--	--	--	--	--	--	--	--
	All Trees	159	-	<0.001	<0.001	0.002	0.002	0.492	0.362	1813	1034	1834	1055	0.902	0.947
		159	$\Theta_{net}$	0.007	<0.001	0.003	0.002	0.490	0.360	1807	1018	1833	1044	0.903	0.948
		159	$\Theta_{net} + T$	--	--	--	--	--	--	--	--	--	--	--	--
POU	Vertical (< 2°)	119	-	<0.001	<0.001 <sup>†</sup>	-0.007	0.004	0.501	0.299	1394	408	1413	428	0.907	0.967
		119	$\Theta_{net}$	<0.001	0.3124 <sup>†</sup>	-0.005	0.004	0.493	0.298	1367	409	1391	433	0.910	0.967
		119	$\Theta_{net} + T$	--	--	--	--	--	--	--	--	--	--	--	--
	Leaning (> 2°)	40	-	<0.001	<0.001	-0.006	-0.013	0.451	0.407	406	340	421	356	0.884	0.906
		40	$\Theta_{net}$	<0.001	<0.001	-0.005	-0.010	0.441	0.383	394	305	413	323	0.888	0.916
		40	$\Theta_{net} + T$	--	<0.001	--	-0.008	--	0.368	--	281	--	304	--	0.922
	All Trees	159	-	<0.001	<0.001	-0.006	-0.001	0.494	0.345	1823	913	1844	933	0.902	0.952
		159	$\Theta_{net}$	0.003	<0.001	-0.005	-0.001	0.492	0.344	1815	902	1841	927	0.902	0.952
		159	$\Theta_{net} + T$	--	<0.001	--	-0.001	--	0.343	--	899	--	930	--	0.953

### 4.3.4. Replacement of DBH

Model outcomes for replacing the DBH from the lean-adjusted BR2 and POU equations with diameters from the 8 raster slices are given in Table 4-7.

Table 4-7 Nonlinear modeling results for two equations predicting total stem volume after substituting diameters at different heights ( $H_D$ ) as inputs. Probability values ( $P(>|t|)$ ) with † had a nonsignificant ( $\alpha = 0.01$ ) parameter from the original model (i.e.,  $a_1$  or  $a_2$  or  $a_3$ ), while those with †† had nonsignificant probability value for the covariate of  $\Theta_{net}$  (i.e.,  $b_1$ ), and

Equation	Sample	$H_D$ (m)	Bias	RMSE	AIC	BIC	$R^2$
BR2	Vertical ( $< 2^\circ$ )	1	0.005	0.485	1334	1358	0.913
		3	0.003	0.400	965	989	0.941
		5 <sup>††</sup>	0.008	0.310	481	505	0.965
		7 <sup>††</sup>	0.011	0.292	368	392	0.969
		10	0.007	0.304	442	466	0.966
		12	0.006	0.293	372	396	0.968
		15 <sup>††</sup>	0.012	0.317	526	550	0.963
		18 <sup>††</sup>	0.016	0.359	759	783	0.953
	Leaning ( $> 2^\circ$ )	1	-0.003	0.436	387	406	0.891
		3	-0.007	0.388	312	331	0.914
		5	-0.011	0.398	328	347	0.910
		7 <sup>††</sup>	0.007	0.257	49	68	0.962
		10	0.004	0.281	105	124	0.955
		12	-0.001	0.312	173	191	0.944
		15	-0.003	0.377	293	312	0.919
		18 <sup>†</sup>	-0.045	0.388	312	331	0.915
POU	Vertical ( $< 2^\circ$ )	1	-0.005	0.493	1367	1391	0.910
		3 <sup>†</sup>	-0.001	0.400	965	990	0.941
		5 <sup>†††</sup>	0.004	0.298	409	433	0.967
		7	0.009	0.279	283	308	0.971
		10	0.003	0.297	398	422	0.968
		12	0.001	0.288	344	369	0.969
		15 <sup>††</sup>	0.006	0.309	475	500	0.965
		18 <sup>†††</sup>	0.010	0.351	720	745	0.955
	Leaning ( $> 2^\circ$ )	1 <sup>†</sup>	-0.005	0.441	394	413	0.888
		3 <sup>†</sup>	-0.007	0.384	305	324	0.916
		5	-0.010	0.383	305	323	0.916
		7 <sup>††</sup>	0.006	0.236	-7	12	0.968
		10 <sup>††</sup>	0.002	0.269	77	96	0.959
		12 <sup>†</sup>	-0.003	0.312	173	192	0.944
		15 <sup>†</sup>	-0.004	0.377	294	313	0.918
		18	-0.003	0.382	302	321	0.916

The two models performed similarly to one another, but leaning trees were impacted differently than vertical trees. For both the leaning and vertical trees, the lowest  $R^2$ , highest RMSE and greatest bias were produced when using the D1, which was used as a proxy for DBH in this study. For vertical trees, the models improved when using D3 compared to D1, then improved further when using D5. The results of using D5, D7, D10, D12, and D15 were similarly favorable, then the fit worsened when using D18 compared to D15. However, for the leaning trees, using D3 also resulted in improvement compared to using D1, but D5 and D3 produced similar results. There was a sharp increase in model performance between using D5 and using D7, which produced the best results for leaning trees, followed by D10, then D12. Using D15 caused worsened fit compared to D12, but similar to D18, D3 and D5 (Figure 4-8).

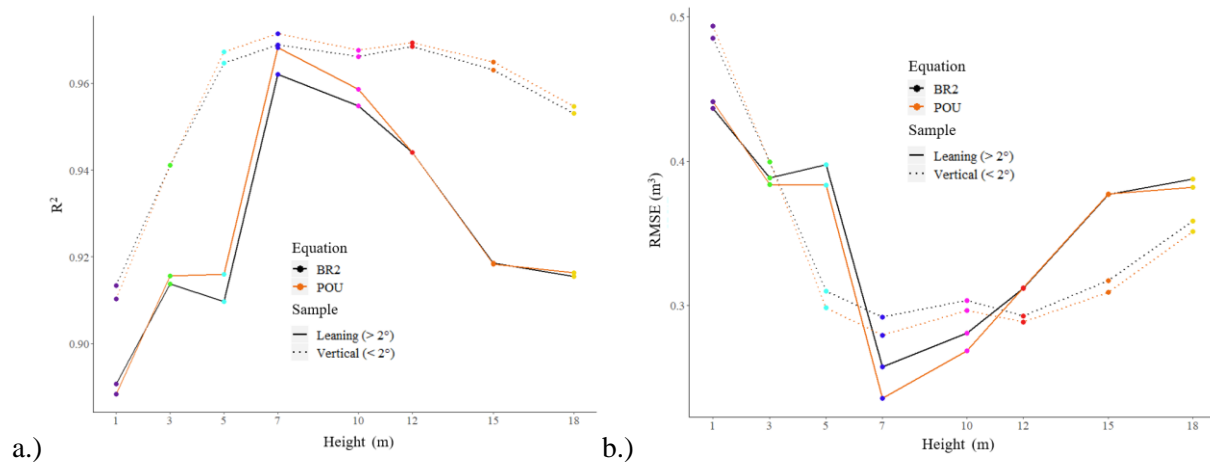


Figure 4-8: Correlation coefficients ( $R^2$ ) (a.) and RMSE (b.) for stem volume models of leaning and vertical trees after substituting diameters at different heights for DBH in the BR2 and POU equations.

## 4.4. Discussion

The quality of the data produced by MLS scans of forests is driven by many factors, including stand characteristics, weather conditions, and terrain ruggedness. However, because the term MLS has been used to describe a range of different sensor and vehicle combinations, there are some inconsistencies in the literature regarding the performance of MLS, which is unsurprising considering the that hardware

reliability is a well-known dependability metric (Eusgeld et al., 2008). In this study, the power and high data collection rate of the sensor resulted in detailed reconstructions of stems, particularly for the portion below the main crown, extending approximately 40 meters horizontally from the sensor. The orientation of the sensor is also a limiting factor, especially for generating returns high on trees. Having the sensor pitched at a 45° toward the rear resulted in the tops of stems being scanned when they were in front of the vehicle, then returns were generated moving down the stems as the vehicle approaches, resulting in the scans ‘rotating’ around tree stems from top to bottom as seen in figures 4-3 and 4-4. Also, if the average angle of the laser pulses is 45° pitched upwards toward the front of the vehicle and the scanner is located 2m above ground, then the laser pulse will travel 25 m to generate returns on tree stems at 20m above ground. As the angle of the pulse moves toward vertical or horizontal, this distance becomes less or greater, respectively. So, though the platform used in this study produced favorable results in many respects, there is some room for improvement. For example, rotating the sensor 90° in either direction so that the beam was pointed upward perpendicular to the road might result in more points on the upper parts of the trees farther away from the road. Also, having a sensor with a wider vertical field of view would be more suitable for scanning stems *in situ* using MLS. In the future, researchers should be mindful of the wide range of platforms that can be considered MLS, thus recognizing the importance of careful description of the hardware configurations used when implementing MLS for single tree measurements.

The ground truth diameter measurements were taken two years after the MLS scans, and the trees in this study were healthy, so it was not surprising that all the DBH measured in 2020 were larger than the D1 estimates from the MLS in 2018. Though I could not separate the error of the estimates from the growth of the trees in terms of comparing the diameters, it was encouraging that there was strong correlation across the two sets of diameters. This is encouraging for future studies that may want to combine manual measurements with MLS scan data because it shows that the point clouds can be used to revisit a site after years have elapsed and easily locate sample trees. Future studies like this one should measure initial ground truth DBH at the same time as the initial MLS scan, and could also add a second

MLS scan to correspond with the DBH measurement after some period has elapsed. Hence, researchers may expand slightly on this study and assess the errors of radial growth estimates from MLS scan data and also track changes in tree lean over time. Tree form is known to vary near roads, including increased basal area in lodgepole pine (*P. contorta*) as noted by (Bowering et al., 2006b), so MLS which are intended to traverse the road while acquiring data would be valuable tools to investigate this in detail. Furthermore, managers of both commercial and public lands commonly use pickup trucks to access the forest, so hypothetically the same vehicles could simultaneously and systematically acquire MLS scan data without disrupting other operations.

The method measuring tree stems by visually fitting circles had strengths and limitations as well. The obvious limitation of the method is timeliness, as it was by far the most time-consuming part of this procedure. Scaling up the method would linearly increase the time cost, which is not ideal. There two ways this part of the procedure could potentially automated. The first involves automatically segmenting the stems and measuring their dimensions directly from the point cloud (Liang et al., 2013), and the second involves using an algorithm such as Hough transform (Atherton and Kerbyson, 1999) to automate the location of stems as presented here, from raster slices. Preliminary analysis suggests that the latter may be accomplished via the open-source computer vision software suite “OpenCV” (Bradski and Kaehler, 2008).

The most important result from this work is showing that leaning trees should be modeled differently than vertical ones. Here a threshold of  $2^\circ$  was chosen based on the previous literature, including the previous study using the same data (Garms et al., in review), which clearly points a significant benefit for accounting for the lean when modeling the stems. However, the lean was also significant as a predictor when modeling vertical trees using their height and DBH, though nonsignificant using heights and  $D_5$ . Perhaps trees leaning less than  $2^\circ$  also have different stem geometry than vertical ones, or, it is possible that this could be an artifact present in the data. However, for mature DF leaning  $2^\circ$

or more, this work highlights the importance of considering the magnitude of tree lean when modeling the merchantable portions of the stems.

The method of approximating stem lean is also important, as it will determine the proportions of leaning and vertical trees. Though no specific threshold was given, (Spies and Franklin, 1991) 12% boles are typically leaning in mature Douglas Fir stands. Using  $\Theta_{net}$  to measure lean, we found that 25% of trees were leaning, while if  $\bar{\Theta}$  had been used, the proportion of leaning trees would have been considerably higher (36%). Here, I demonstrated that a conservative metric of lean, which involves simply measuring the horizontal departure between the top and bottom of the stem, can be used to improve the fit of stem models. Because this method of estimating lean is also the same method that is commonly used in practice, the findings of this study can be implemented currently. However, there are benefits to more precise descriptions of stem lean, such as the incremental section angles estimated between the base and top of the stem and the average of those measurements,  $\bar{\Theta}$ . The values for  $\bar{\Theta}$  were consistently larger than the corresponding  $\Theta_{net}$  values for one simple reason: the horizontal path of the leaning stem is curved. Though it was not addressed here, similar data could be used to investigate the curvature of leaning stems more specifically, such as whether the curves are continuous or abrupt, which could be used in differentiation between trees that lean, sweep, and crook.

Nevertheless, DF trees have been documented to have some subtle physiological differences when leaning quite slightly, namely, that they tended to be elliptical with the longer axis parallel to the lean by Williamson (1975), who also noted that this was likely unimportant. Here, I show that slight lean changes the way that stems should be modeled, which brings new relevance to Williamson's contention about stem roundness. It could be that the way that stem geometries change according to lean is predictable in the sense that it can also be modeled, which would allow for leaning trees and vertical ones to be considered together with the same volume approximation equation

## 4.5. Conclusions

The evidence presented here shows that MLS are powerful tools for modeling tree stems, but they are not created equally. In fact, the variability and relative novelty of the technology make MLS in forestry research a broad category of systems, which led to the recommendation of carefully considering the sensor, orientation, and trajectory when deploying MLS for scanning trees, and especially when using them to produce peer-reviewed research. In this study the Velodyne HDL-64E was positioned in the back of a pickup truck pitched at a 45° angle toward the rear of the vehicle. This resulted in an upward scan angle when scanning ahead of the truck, such that there were ample returns along the tree stems up to the base of the crown that they could be visually approximated with circles. The practical range of the MLS for this procedure was determined to be about 40m of the sensor, which is considerably less than the specified range of the sensor (120m), though it is possible that adjusting the orientation of the sensor tilt to be perpendicular to the road or using a sensor with a wider vertical field of view could improve the range of the system. Still, MLS based on passenger pickup trucks have the potential to efficiently capture tree stems in great detail, and because similar trucks are virtually ubiquitous in the forestry industry, the potential for modifying existing vehicles to have similar capabilities is very high.

The stem locations from the MLS were used to create and compare two methods for approximation of lean. The first method, which mirrors how lean is conventionally measured in the field, used the top and bottom locations of the stem to produce a conservative lean estimate,  $\Theta_{net}$ , while the second,  $\bar{\Theta}$ , used the average of 7 sectional angle estimates along the stem. The conservative estimate for lean proved to be significant for predicting the stem taper and volume when added to existing stem taper and volume equations to model leaning ( $>2^\circ$ ) trees, and to a lesser degree, trees that we considered vertical. The evidence presented suggests that the  $2^\circ$  is in this case an appropriate threshold for considering trees to be leaning, but there is also some evidence suggesting the threshold could be even less. Visual approximation of lean below  $2^\circ$  reliably is not feasible, however MLS scans allow for more precise estimates.

When lean is estimated using multiple locations on the stem as opposed to just the top and bottom, the nonlinearity (i.e., curve) of the lean path can also be considered. The results of this study demonstrate that more precise approximation of lean reveals that trees often lean in a curved path, which should be investigated further. As the patterns connecting tree lean and stem geometry are better understood, a more comprehensive approach to modeling leaning trees and vertical ones together may be developed. However, at present, the presence and magnitude of tree lean should be taken into consideration when nonlinear equations are used to model mature DF stems.

## 5. Conclusion

The individual studies that comprise this dissertation support the overarching goal, which was to examine how point cloud data can be used to augment tree level estimates for forest inventory. Two different stages in the life of a stand were examined, namely, prior to planting when the trees are in the seedling stage, and once the trees have reached maturity and are ready for harvest. In both scenarios, evidence is presented to broaden the range of known applications of cutting-edge tools for forest research: UAS and MLS.

By following the recommendations in Chapter 2, researchers can incorporate UAS seedling size and mortality assessment into future common garden studies. Because common gardens are currently used to address a wide range of suitability questions, the implications of this portion of my dissertation are potentially wide reaching as well. The US Forest Service's Genetic Resource center, which is located about 120 km southwest of Corvallis, has been using common gardens to select disease resistant individuals in breeding programs for over 50 years (Sniezko, 2006), and is a perfect example of an institution that could potentially benefit from this work.

In Chapter 3, the capabilities of three platforms that can produce point clouds of forests were discussed in depth. The least expensive platform, the UAS with multispectral sensor, can be currently be purchased for about \$2000, which is roughly half of the price of the platform I used when it was purchased in 2015.

Even though the UALS outperformed the UAS in some ways, specifically in the detection of tree stems and the fine scale textures of tree crowns, the UAS data was reliable in terms of locating tree crown positions and estimating their heights. Due to the trends in reduced price, increased ease of use, and more powerful postprocessing software, it is likely that UAS will become increasingly prevalent for aerial surveys of forests. Supplementing UAS data products such as point clouds and canopy height models (CHMs) with lidar measurements has several advantages. Having two remotely sensed estimates for a parameter such as height that are generally in agreement reduces the need for ground truth validation, which could result in lower costs. Also, UAS can provide spectral information which can be used to

detect diseases such as swiss needle cast (Burnett, 2017). Furthermore, small lightweight multispectral sensors like the one I used in Chapters 2 and 3 can be carried by the same aircraft as the lidar sensor and both can simultaneously record data, meaning two of the three platforms in Chapter 3 can be combined into one. The other platform, MLS, is a powerful tool for forestry in its own right, and it has different strengths and limitations than UAS or UALS, which led to the continuation of my work presented in Chapter 4.

The work presented in Chapter 4 gives new insights about the potential MLS to survey trees from below the canopy. By focusing on the merchantable portions of the stems from the MLS point clouds, I was able to produce two different lean estimates for mature Douglas Firs. One of the methods used only the locations of the stems at the base and near the crown, similarly to how lean is normally assessed in the field, and generally produced more conservative estimates than the other method, which used the average of seven section angles estimated along the boles of the trees. I found that including a conservative estimate of lean as predictors in existing stem taper and volume equations

Overall, this dissertation supports the usage of UAS, UALS and MLS for measuring individual trees in two different scenarios. For small seedlings, UAS can be used to supplement ground-based measurements, expand the capabilities of surveys, and detect mortality. For large trees, UAS can be used in conjunction with active sensor technology to produce detailed 3D digital reconstructions of entire stands. The data from these platforms can be gathered expeditiously compared to manual measurements, and the results have the potential to be more accurate as well. Using MLS to survey mature stems from the forest road allowed me to quantify stem lean in a novel way, then apply those lean estimates to existing stem taper and lean equations to improve them. It is my sincere hope that these contributions, both for the application of seedling measurements and for those regarding mature trees, may be of some use to my colleagues in the forestry research community.

## 6. Bibliography

- Agisoft, L.L.C., 2017. Agisoft photoscan professional edition. Agisoft LLC: St Petersburg.
- Akaike, H., 1987. Factor analysis and AIC, in: Selected Papers of Hirotugu Akaike. Springer, pp. 371–386.
- Aldred, A., Bonner, G., 1985. Application of airborne lasers to forest surveys, Petawawa National Forestry Institute, Canadian Forestry Service. Agriculture Canada, Chalk River ON.
- Amidon, E.L., 1984. A general taper functional form to predict bole volume for five mixed-conifer species in California. *Forest Science* 30, 166–171.
- Andersen, H.-E., Reutebuch, S.E., McGaughey, R.J., 2006. A rigorous assessment of tree height measurements obtained using airborne lidar and conventional field methods. *Canadian Journal of Remote Sensing* 32, 355–366.
- Atherton, T.J., Kerbyson, D.J., 1999. Size invariant circle detection. *Image and Vision computing* 17, 795–803.
- Banu, T.P., Borlea, G.F., Banu, C., 2016. The Use of Drones in Forestry. *Journal of Environmental Science and Engineering B* 5.
- Barnes, E.M., Clarke, T.R., Richards, S.E., Colaizzi, P.D., Haberland, J., Kostrzewski, M., Waller, P., Choi, C., Riley, E., Thompson, T., 2000. Coincident detection of crop water stress, nitrogen status and canopy density using ground based multispectral data, in: Proceedings of the Fifth International Conference on Precision Agriculture, Bloomington, MN, USA.
- Bauwens, S., Bartholomeus, H., Calders, K., Lejeune, P., 2016. Forest inventory with terrestrial LiDAR: A comparison of static and hand-held mobile laser scanning. *Forests* 7, 127.
- Benesty, J., Chen, J., Huang, Y., Cohen, I., 2009. Pearson correlation coefficient, in: Noise Reduction in Speech Processing. Springer, pp. 1–4.
- Besl, P.J., McKay, N.D., 1992. Method for registration of 3-D shapes, in: Sensor Fusion IV: Control Paradigms and Data Structures. International Society for Optics and Photonics, pp. 586–606.
- Biging, G.S., 1984. Taper equations for second-growth mixed conifers of Northern California. *Forest Science* 30, 1103–1117.
- Bloomberg, W.J., 1971. Diseases of Douglas-fir seedlings caused by *Fusarium oxysporum*. *Phytopathology* 61, 467–470.
- Board, A., 2008. LAS file format specification.
- Bose, A.K., Weiskittel, A., Kuehne, C., Wagner, R.G., Turnblom, E., Burkhart, H.E., 2018. Does commercial thinning improve stand-level growth of the three most commercially important softwood forest types in North America? *Forest Ecology and Management* 409, 683–693.
- Bowering, M., LeMay, V., Marshall, P., 2006a. Effects of forest roads on the growth of adjacent lodgepole pine trees. *Canadian Journal of Forest Research* 36, 919–929. <https://doi.org/10.1139/x05-300>
- Bowering, M., LeMay, V., Marshall, P., 2006b. Effects of forest roads on the growth of adjacent lodgepole pine trees. *Canadian journal of forest research* 36, 919–929.
- Brackett, M., 1977. Notes on tariff tree volume computation.
- Bradski, G., Kaehler, A., 2008. Learning OpenCV: Computer vision with the OpenCV library. O'Reilly Media, Inc.
- Brandtberg, T., 1999. Automatic individual tree-based analysis of high spatial resolution remotely sensed data.
- Breiman, L., 2001. Random forests. *Machine learning* 45, 5–32.
- Breiman, L., Friedman, J., Olshen, R.A., Stone, C.J., 1984. Classification and Regression Trees. Chapman & Hall/CRC, Boca Raton FL.
- Burnett, J., Burnett, J.D., 2017. Environmental Remote Sensing with Unmanned Aircraft Systems.
- Cao, Q.V., 2009. Calibrating a segmented taper equation with two diameter measurements. *Southern Journal of Applied Forestry* 33, 58–61.

- Cao, Q.V., Wang, J., 2015. Evaluation of methods for calibrating a tree taper equation. *Forest Science* 61, 213–219.
- Čerňava, J., Tuček, J., Koreň, M., Mokoš, M., 2017. Estimation of diameter at breast height from mobile laser scanning data collected under a heavy forest canopy. *Journal of Forest Science* 63, 433–441.
- Chisholm, R.A., Cui, J., Lum, S.K., Chen, B.M., 2013. UAV LiDAR for below-canopy forest surveys. *Journal of Unmanned Vehicle Systems* 1, 61–68.
- Collet, C., Lanter, O., Pardos, M., 2001. Effects of canopy opening on height and diameter growth in naturally regenerated beech seedlings. *Annals of Forest Science* 58, 127–134.
- Congedo, L., 2016. Semi-automatic classification plugin documentation. Release 4, 29.
- Conrad, O., Bechtel, B., Bock, M., Dietrich, H., Fischer, E., Gerlitz, L., Wehberg, J., Wichmann, V., Böhner, J., 2015. System for automated geoscientific analyses (SAGA) v. 2.1. 4. *Geoscientific Model Development Discussions* 8.
- Cover, T., Hart, P., 1967. Nearest neighbor pattern classification. *IEEE transactions on information theory* 13, 21–27.
- Cunningham, K., 2012. Forest Landowner's Guide to Field Grading Hardwood Trees (No. FSA5015-PD-- 8-- 12RV). University of Arkansas System.
- Dalponte, M., Coomes, D.A., 2016. Tree-centric mapping of forest carbon density from airborne laser scanning and hyperspectral data. *Methods in ecology and evolution* 7, 1236–1245.
- Dandois, J.P., Ellis, E.C., 2010. Remote sensing of vegetation structure using computer vision. *Remote sensing* 2, 1157–1176.
- Edson, C., Wing, M.G., 2011. Airborne light detection and ranging (LiDAR) for individual tree stem location, height, and biomass measurements. *Remote Sensing* 3, 2494–2528.
- Eusgeld, I., Fechner, B., Salfner, F., Walter, M., Limbourg, P., Zhang, L., 2008. Hardware reliability, in: *Dependability Metrics*. Springer, pp. 59–103.
- Fairweather, M.L., Geils, B.W., 2011. First Report of the White Pine Blister Rust Pathogen, *Cronartium ribicola*, in Arizona. *Plant Disease* 95, 494–494. <https://doi.org/10.1094/PDIS-10-10-0699>
- Fan, Y., Feng, Z., Mannan, A., Khan, T.U., Shen, C., Saeed, S., 2018. Estimating tree position, diameter at breast height, and tree height in real-time using a mobile phone with RGB-D SLAM. *Remote Sensing* 10, 1845.
- Feduck, C., McDermid, G., Castilla, G., 2018. Detection of Coniferous Seedlings in UAV Imagery. *Forests* 9, 432. <https://doi.org/10.3390/f9070432>
- Forsman, M., Börlin, N., Holmgren, J., 2016. Estimation of tree stem attributes using terrestrial photogrammetry with a camera rig. *Forests* 7, 61.
- Fritz, A., Kattenborn, T., Koch, B., 2013. UAV-based photogrammetric point clouds-tree stem mapping in open stands in comparison to terrestrial laser scanner point clouds. *ISPRS-International Archives of the Photogrammetry, Remote Sensing and Spatial Information Sciences* 141–146.
- Fromm, M., Schubert, M., Castilla, G., Linke, J., McDermid, G., 2019. Automated Detection of Conifer Seedlings in Drone Imagery Using Convolutional Neural Networks. *Remote Sensing* 11, 2585.
- Gambella, F., Sistu, L., Piccirilli, D., Corposanto, S., Caria, M., Arcangeletti, E., Proto, A.R., Chessa, G., Pazzona, A., 2016. Forest and UAV: A bibliometric review. *Contemp. Eng. Sci.* 9, 1359–1370.
- Garms, C., Simpson, C., Parrish, C., Wing, M., Strimbu, B., in review. Assessing Lean and Positional Error of Individual Mature Douglas-Firs with Active and Passive Sensors. *Canadian Journal of Forest Research*.
- Gatziolis, D., Fried, J.S., Monleon, V.S., 2010a. Challenges to estimating tree height via LiDAR in closed-canopy forests: A parable from Western Oregon. *Forest Science* 56, 139–155.
- Gatziolis, D., Fried, J.S., Monleon, V.S., 2010b. Challenges to estimating tree height via LiDAR in closed-canopy forests: A parable from Western Oregon. *Forest Science* 56, 139–155.
- Genuer, R., Poggi, J.-M., Tuleau-Malot, C., 2010. Variable selection using random forests. *Pattern Recognition Letters* 31, 2225–2236. <https://doi.org/10.1016/j.patrec.2010.03.014>

- Gil-Docampo, M.L., Ortiz-Sanz, J., Martínez-Rodríguez, S., Marcos-Robles, J.L., Arza-García, M., Sánchez-Sastre, L.F., 2020. Plant survival monitoring with UAVs and multispectral data in difficult access afforested areas. *Geocarto International* 35, 128–140.
- Girardeau-Montaut, D., 2015. Cloud compare—3d point cloud and mesh processing software. Open Source Project.
- Gitelson, A.A., 2005. Remote estimation of canopy chlorophyll content in crops. *Geophysical Research Letters* 32. <https://doi.org/10.1029/2005GL022688>
- Gitelson, A.A., Kaufman, Y.J., Merzlyak, M.N., 1996. Use of a green channel in remote sensing of global vegetation from EOS-MODIS. *Remote sensing of Environment* 58, 289–298.
- Goodbody, T.R., Coops, N.C., Hermosilla, T., Tompalski, P., Crawford, P., 2018. Assessing the status of forest regeneration using digital aerial photogrammetry and unmanned aerial systems. *International Journal of Remote Sensing* 39, 5246–5264.
- Goodrich, B.A., Waring, K.M., 2017. Pinus strobiformis seedling growth in southwestern US mixed conifer forests in managed and non-managed stands. *Forestry: An International Journal of Forest Research* 90, 393–403. <https://doi.org/10.1093/forestry/cpw057>
- Goodrich, B.A., Waring, K.M., Flores-Renteria, L., 2018. Pinus strobiformis gene conservation and genecology, in: In: Schoettle, Anna W.; Snieszko, Richard A.; Kliejunas, John T., Eds. *Proceedings of the IUFRO Joint Conference: Genetics of Five-Needle Pines, Rusts of Forest Trees, and Strobosphere; 2014 June 15-20; Fort Collins, CO. Proc. RMRS-P-76. Fort Collins, CO: US Department of Agriculture, Forest Service, Rocky Mountain Research Station. p. 21-29. pp. 21–29.*
- Green, P.C., Burkhart, H.E., 2020. Plantation Loblolly Pine Seedling Counts with Unmanned Aerial Vehicle Imagery: A Case Study. *Journal of Forestry*.
- Grenzdörffer, G.J., Engel, A., Teichert, B., 2008. The photogrammetric potential of low-cost UAVs in forestry and agriculture. *The International Archives of the Photogrammetry, Remote Sensing and Spatial Information Sciences* 31, 1207–1214.
- Guerra-Hernández, J., Cosenza, D.N., Rodríguez, L.C.E., Silva, M., Tomé, M., Díaz-Varela, R.A., González-Ferreiro, E., 2018. Comparison of ALS-and UAV (SfM)-derived high-density point clouds for individual tree detection in Eucalyptus plantations. *International Journal of Remote Sensing* 39, 5211–5235.
- Gutiérrez, Á.G., Schnabel, S., Lavado Contador, J.F., 2009. Using and comparing two nonparametric methods (CART and MARS) to model the potential distribution of gullies. *Ecological Modelling, Selected Papers on Spatially Explicit Landscape Modelling: Current practices and challenges* 220, 3630–3637. <https://doi.org/10.1016/j.ecolmodel.2009.06.020>
- Hamraz, H., Contreras, M.A., Zhang, J., 2017. Vertical stratification of forest canopy for segmentation of understory trees within small-footprint airborne LiDAR point clouds. *ISPRS Journal of Photogrammetry and Remote Sensing* 130, 385–392.
- Henning, J.G., Radtke, P.J., 2006. Detailed stem measurements of standing trees from ground-based scanning lidar. *Forest Science* 52, 67–80.
- Herrero-Huerta, M., Lindenbergh, R., Rodríguez-Gonzálvez, P., 2018. Automatic tree parameter extraction by a Mobile LiDAR System in an urban context. *PloS one* 13, e0196004.
- Hijmans, R.J., Van Etten, J., 2014. raster: Geographic data analysis and modeling. R package version 2.2-31. Google Scholar.
- Holopainen, M., Kankare, V., Vastaranta, M., Liang, X., Lin, Y., Vaaja, M., Yu, X., Hyypä, J., Hyypä, H., Kaartinen, H., 2013. Tree mapping using airborne, terrestrial and mobile laser scanning—A case study in a heterogeneous urban forest. *Urban forestry & urban greening* 12, 546–553.
- Hunt Jr, E.R., Doraiswamy, P.C., McMurtrey, J.E., Daughtry, C.S., Perry, E.M., Akhmedov, B., 2013. A visible band index for remote sensing leaf chlorophyll content at the canopy scale. *International Journal of Applied Earth Observation and Geoinformation* 21, 103–112.
- Hyypä, J., 1999. Detecting and estimating attributes for single trees using laser scanner. *Photogramm J Finland* 16, 27–42.

- Hyypä, J., Kelle, O., Lehtikainen, M., Inkinen, M., 2001. A segmentation-based method to retrieve stem volume estimates from 3-D tree height models produced by laser scanners. *IEEE Transactions on geoscience and remote sensing* 39, 969–975.
- Iglhaut, J., Cabo, C., Puliti, S., Piermattei, L., O'Connor, J., Rosette, J., 2019. Structure from motion photogrammetry in forestry: A review. *Current Forestry Reports* 5, 155–168.
- Jaakkola, A., Hyypä, J., Kukko, A., Yu, X., Kaartinen, H., Lehtomäki, M., Lin, Y., 2010. A low-cost multi-sensoral mobile mapping system and its feasibility for tree measurements. *ISPRS journal of Photogrammetry and Remote Sensing* 65, 514–522.
- Jakubowski, M., Li, W., Guo, Q., Kelly, M., 2013. Delineating individual trees from LiDAR data: A comparison of vector-and raster-based segmentation approaches. *Remote Sensing* 5, 4163–4186.
- Jia, X., Richards, J.A., 1994. Efficient maximum likelihood classification for imaging spectrometer data sets. *IEEE Transactions on Geoscience and Remote Sensing* 32, 274–281.
- Kaartinen, H., Hyypä, J., Yu, X., Vastaranta, M., Hyypä, H., Kukko, A., Holopainen, M., Heipke, C., Hirschmugl, M., Morsdorf, F., 2012a. An international comparison of individual tree detection and extraction using airborne laser scanning. *Remote Sensing* 4, 950–974.
- Kaartinen, H., Hyypä, J., Yu, X., Vastaranta, M., Hyypä, H., Kukko, A., Holopainen, M., Heipke, C., Hirschmugl, M., Morsdorf, F., Næsset, E., Pitkänen, J., Popescu, S., Solberg, S., Wolf, B.M., Wu, J.-C., 2012b. An International Comparison of Individual Tree Detection and Extraction Using Airborne Laser Scanning. *Remote Sensing* 4, 950.
- Koch, B., Kattenborn, T., Straub, C., Vauhkonen, J., 2014. Segmentation of forest to tree objects, in: *Forestry Applications of Airborne Laser Scanning*. Springer, pp. 89–112.
- Kozak, A., Munro, D.D., Smith, J.H.G., 1969. Taper functions and their application in forest inventory. *The Forestry Chronicle* 45, 278–283.
- Kramer, R.D., Sillett, S.C., Van Pelt, R., 2018. Quantifying aboveground components of *Picea sitchensis* for allometric comparisons among tall conifers in North American rainforests. *Forest ecology and management* 430, 59–77.
- Kursa, M.B., Rudnicki, W.R., 2010. Feature selection with the Boruta package. *J Stat Softw* 36, 1–13.
- Kursa, M.B., Rudnicki, W.R., Kursa, M.M.B., 2018. Package 'Boruta.'
- Leckie, D., Gougeon, F., Hill, D., Quinn, R., Armstrong, L., Shreenan, R., 2003. Combined high-density lidar and multispectral imagery for individual tree crown analysis. *Canadian Journal of Remote Sensing* 29, 633–649.
- Lei, H., Milota, M.R., Gartner, B.L., 1996. Between-and within-tree variation in the anatomy and specific gravity of wood in Oregon white oak (*Quercus garryana* Dougl.). *IAWA journal* 17, 445–461.
- Leondes, C.T., 1970. Theory and applications of Kalman filtering. *ADVISORY GROUP FOR AEROSPACE RESEARCH AND DEVELOPMENT NEUILLY-SUR-SEINE (FRANCE)*.
- Levinson, N., 1946. The Wiener (root mean square) error criterion in filter design and prediction. *Journal of Mathematics and Physics* 25, 261–278.
- Li, W., Guo, Q., Jakubowski, M.K., Kelly, M., 2012. A new method for segmenting individual trees from the lidar point cloud. *Photogrammetric Engineering & Remote Sensing* 78, 75–84.
- Liang, X., Kankare, V., Yu, X., Hyypä, J., Holopainen, M., 2013. Automated stem curve measurement using terrestrial laser scanning. *IEEE Transactions on Geoscience and Remote Sensing* 52, 1739–1748.
- Liaw, A., Wiener, M., 2002. Classification and Regression by randomForest 2, 5.
- Lin, Y., Hyypä, J., Jaakkola, A., 2010. Mini-UAV-borne LIDAR for fine-scale mapping. *IEEE Geoscience and Remote Sensing Letters* 8, 426–430.
- Lisein, J., Pierrot-Deseilligny, M., Bonnet, S., Lejeune, P., 2013. A photogrammetric workflow for the creation of a forest canopy height model from small unmanned aerial system imagery. *Forests* 4, 922–944.
- Maclean, G.A., Krabill, W.B., 1986. Gross-merchantable timber volume estimation using an airborne LIDAR system. *Canadian Journal of Remote Sensing* 12, 7–18.

- Maclean, G.A., Martin, G.L., 1984. Merchantable timber volume estimation using cross-sectional photogrammetric and densitometric methods. *Canadian Journal of Forest Research* 14, 803–810.
- Mao, P., Han, G., Wang, G., Yu, J., Shao, H., 2014. Effects of Age and Stand Density of Mother Trees on Early *Pinus thunbergii* Seedling Establishment in the Coastal Zone, China. *The Scientific World Journal* 2014, 1–9. <https://doi.org/10.1155/2014/468036>
- MATLAB, 2010. version 7.10.0 (R2010a). The MathWorks Inc., Natick, Massachusetts.
- Max, T.A., Burkhart, H.E., 1976. Segmented polynomial regression applied to taper equations. *Forest Science* 22, 283–289.
- Means, J.E., Acker, S.A., Fitt, B.J., Renslow, M., Emerson, L., Hendrix, C.J., 2000. Predicting forest stand characteristics with airborne scanning lidar. *Photogrammetric Engineering and Remote Sensing* 66, 1367–1372.
- Meyer, F., Beucher, S., 1990a. Morphological segmentation. *Journal of visual communication and image representation* 1, 21–46.
- Meyer, F., Beucher, S., 1990b. Morphological segmentation. *Journal of visual communication and image representation* 1, 21–46.
- Miles, J., 2014. R squared, adjusted R squared. Wiley StatsRef: Statistics Reference Online.
- Miller, J.M., 2015. Estimation of individual tree metrics using structure-from-motion photogrammetry.
- Moe, K.T., Owari, T., Furuya, N., Hiroshima, T., 2020. Comparing Individual Tree Height Information Derived from Field Surveys, LiDAR and UAV-DAP for High-Value Timber Species in Northern Japan. *Forests* 11, 223.
- Mortimer, M.J., Kane, B., 2004. Hazard tree liability in the United States: uncertain risks for owners and professionals. *Urban forestry & urban greening* 2, 159–165.
- Naesset, E., 1997a. Determination of mean tree height of forest stands using airborne laser scanner data. *ISPRS Journal of Photogrammetry and Remote Sensing* 52, 49–56.
- Naesset, E., 1997b. Estimating timber volume of forest stands using airborne laser scanner data. *Remote Sensing of Environment* 61, 246–253.
- Nelson, R., Krabill, W., MacLean, G., 1984. Determining forest canopy characteristics using airborne laser data. *Remote Sensing of Environment* 15, 201–212.
- Neter, J., Kutner, M.H., Nachtsheim, C.J., Wasserman, W., 1996. *Applied linear statistical models*. WCB McGraw-Hill, Boston.
- Nilsson, M., 1996. Estimation of tree heights and stand volume using an airborne lidar system. *Remote sensing of environment* 56, 1–7.
- Niuniu, X., Yuxun, L., 2010. Review of decision trees. Presented at the 3rd International Conference on Computer Science and Information Technology, IEEE, pp. 105–109. <https://doi.org/10.1109/ICCSIT.2010.5564437>
- Norgren, O., 1996. Growth analysis of Scots pine and lodgepole pine seedlings. *Forest Ecology and Management* 86, 15–26.
- Oleksyn, J., Modrzyński, J., Tjoelker, M.G., Reich, P.B., Karolewski, P., 1998. Growth and physiology of *Picea abies* populations from elevational transects: common garden evidence for altitudinal ecotypes and cold adaptation. *Functional Ecology* 12, 573–590.
- O'Neill, G.A., Aitken, S.N., Adams, W.T., 2000. Genetic selection for cold hardiness in coastal Douglas-fir seedlings and saplings. *Canadian Journal of Forest Research* 30, 1799–1807.
- Ozdemir, I., 2008. Estimating stem volume by tree crown area and tree shadow area extracted from pan-sharpened Quickbird imagery in open Crimean juniper forests. *International Journal of Remote Sensing* 29, 5643–5655.
- Panagiotidis, D., Abdollahnejad, A., Surový, P., Chiteculo, V., 2017. Determining tree height and crown diameter from high-resolution UAV imagery. *International Journal of Remote Sensing* 38, 2392–2410. <https://doi.org/10.1080/01431161.2016.1264028>
- PDAL Contributors, 2018. PDAL Point Data Abstraction Library. <https://doi.org/10.5281/zenodo.2556738>

- Pierzchała, M., Giguère, P., Astrup, R., 2018. Mapping forests using an unmanned ground vehicle with 3D LiDAR and graph-SLAM. *Computers and Electronics in Agriculture* 145, 217–225.
- Pillow, M.Y., Luxford, R.F., 1937. Structure, occurrence, and properties of compression wood.
- Planchon, O., Darboux, F., 2002. A fast, simple and versatile algorithm to fill the depressions of digital elevation models. *CATENA* 46, 159–176. [https://doi.org/10.1016/S0341-8162\(01\)00164-3](https://doi.org/10.1016/S0341-8162(01)00164-3)
- Popescu, S.C., Wynne, R.H., 2004. Seeing the trees in the forest. *Photogrammetric Engineering & Remote Sensing* 70, 589–604.
- Poudel, K.P., Temesgen, H., Gray, A.N., 2018. Estimating upper stem diameters and volume of Douglas-fir and Western hemlock trees in the Pacific northwest. *Forest Ecosystems* 5, 16.
- Puliti, S., Ørka, H., Gobakken, T., Næsset, E., 2015. Inventory of Small Forest Areas Using an Unmanned Aerial System. *Remote Sensing* 7, 9632–9654. <https://doi.org/10.3390/rs70809632>
- Puliti, S., Talbot, B., Astrup, R., 2018. Tree-Stump Detection, Segmentation, Classification, and Measurement Using Unmanned Aerial Vehicle (UAV) Imagery. *Forests* 9, 102. <https://doi.org/10.3390/f9030102>
- QGIS Development Team, 2015. QGIS geographic information system. Open Source Geospatial Foundation Project, Versão 2.
- Quiros, J., Martello, M., Khot, L., 2018. Field grown apple nursery tree plant counting based on small UAS imagery derived elevation maps.
- R Core Team, 2017. R: A language and environment for statistical computing. R Foundation for Statistical Computing, Vienna, Austria.
- Reutebuch, S.E., McGaughey, R.J., Andersen, H.-E., Carson, W.W., 2003. Accuracy of a high-resolution lidar terrain model under a conifer forest canopy. *Canadian journal of remote sensing* 29, 527–535.
- Robertson, F.D., 2000. *Timber Cruising Handbook*. USDA Forest Service, Washington DC.
- Rossi, A.J., Rhody, H., Salvaggio, C., Walvoord, D.J., 2012a. Abstracted workflow framework with a structure from motion application, in: *Image Processing Workshop (WNYIPW), 2012 Western New York*. IEEE, pp. 9–12.
- Rossi, A.J., Rhody, H., Salvaggio, C., Walvoord, D.J., 2012b. Abstracted workflow framework with a structure from motion application, in: *2012 Western New York Image Processing Workshop*. IEEE, pp. 9–12.
- Rouse Jr, J., Haas, R.H., Schell, J.A., Deering, D.W., 1974. Monitoring vegetation systems in the Great Plains with ERTS.
- Roussel, J.R., 2017. *Auty, D. lidR: Airborne LiDAR Data Manipulation and Visualization for Forestry Applications*. R package version 1.
- Roussel, J.-R., Auty, D., 2019. *lidR: Airborne LiDAR Data Manipulation and Visualization for Forestry Applications*.
- Ryan, M.G., Yoder, B.J., 1997. Hydraulic limits to tree height and tree growth. *Bioscience* 47, 235–242.
- Sáenz-Romero, C., Rehfeldt, G.E., Crookston, N.L., Duval, P., St-Amant, R., Beaulieu, J., Richardson, B.A., 2010. Spline models of contemporary, 2030, 2060 and 2090 climates for Mexico and their use in understanding climate-change impacts on the vegetation. *Climatic Change* 102, 595–623.
- Schoettle, A.W., Burns, K.S., Sniezko, R.A., 2018. The proactive strategy: Preparing the landscape for invasion by accelerating the evolution of resistance, in: In: Schoettle, Anna W.; Sniezko, Richard A.; Kliejunas, John T., Eds. *Proceedings of the IUFRO Joint Conference: Genetics of Five-Needle Pines, Rusts of Forest Trees, and Strobosphere; 2014 June 15-20; Fort Collins, CO*. Proc. RMRS-P-76. Fort Collins, CO: US Department of Agriculture, Forest Service, Rocky Mountain Research Station. p. 221-222. pp. 221–222.
- Schwarz, G., 1978. Estimating the dimension of a model. *The annals of statistics* 6, 461–464.
- Seager, R., Ting, M., Held, I., Kushnir, Y., Lu, J., Vecchi, G., Huang, H.-P., Harnik, N., Leetmaa, A., Lau, N.-C., 2007. Model projections of an imminent transition to a more arid climate in southwestern North America. *Science* 316, 1181–1184.

- Shaw, R.G., Etterson, J.R., 2012. Rapid climate change and the rate of adaptation: insight from experimental quantitative genetics. *New Phytologist* 195, 752–765.
- Shirk, A.J., Cushman, S.A., Waring, K.M., Wehenkel, C.A., Leal-Sáenz, A., Toney, C., Lopez-Sanchez, C.A., 2018. Southwestern white pine (*Pinus strobiformis*) species distribution models project a large range shift and contraction due to regional climatic changes. *Forest ecology and management* 411, 176–186.
- Silva, C.A., Hudak, A.T., Vierling, L.A., Loudermilk, E.L., O'Brien, J.J., Hiers, J.K., Jack, S.B., Gonzalez-Benecke, C., Lee, H., Falkowski, M.J., 2016. Imputation of individual Longleaf Pine (*Pinus palustris* Mill.) Tree attributes from field and LiDAR data. *Canadian journal of remote sensing* 42, 554–573.
- Snieszko, R.A., 2006. Resistance breeding against nonnative pathogens in forest trees—current successes in North America. *Canadian Journal of Plant Pathology* 28, S270–S279.
- Sofonia, J.J., Phinn, S., Roelfsema, C., Kendoul, F., Rist, Y., 2019. Modelling the effects of fundamental UAV flight parameters on LiDAR point clouds to facilitate objectives-based planning. *ISPRS journal of photogrammetry and remote sensing* 149, 105–118.
- Solodukhin, V., Zukov, A., Mazugin, I., 1977. Possibilities of laser aerial photography for forest profiling. *Lesnoe Khozyaisto (Forest Management)* 10, 53–58.
- Solodukhin, V.I., Zhukov, A.Y., Mazhugin, I.N., Narkevich, V.I., 1976. *Metody Izuchenija Vertikal'nyh Sechenij Drevostoev (Method of study of vertical sections of forest stands)*. Leningrad Scientific Research Institute of Forestry, Leningrad 55.
- South, D.B., Harris, S.W., Barnett, J.P., Hains, M.J., Gjerstad, D.H., 2005. Effect of container type and seedling size on survival and early height growth of *Pinus palustris* seedlings in Alabama, U.S.A. *Forest Ecology and Management* 204, 385–398. <https://doi.org/10.1016/j.foreco.2004.09.016>
- Strahler, A.H., Jupp, D.L., Woodcock, C.E., Schaaf, C.B., Yao, T., Zhao, F., Yang, X., Lovell, J., Culvenor, D., Newnham, G., 2008. Retrieval of forest structural parameters using a ground-based lidar instrument (Echidna®). *Canadian Journal of Remote Sensing* 34, S426–S440.
- Strimbu, B.M., Qi, C., Sessions, J., 2019. Accurate Geo-Referencing of Trees with No or Inaccurate Terrestrial Location Devices. *Remote Sensing* 11, 1877. <https://doi.org/10.3390/rs11161877>
- Strîmbu, V.F., Strîmbu, B.M., 2015. A graph-based segmentation algorithm for tree crown extraction using airborne LiDAR data. *ISPRS Journal of Photogrammetry and Remote Sensing* 104, 30–43.
- Swinfield, T., Lindsell, J.A., Williams, J.V., Harrison, R.D., Gemita, E., Schönlieb, C.B., Coomes, D.A., 2019. Accurate Measurement of Tropical Forest Canopy Heights and Aboveground Carbon Using Structure From Motion. *Remote Sensing* 11, 928.
- Tang, J., Chen, Y., Kukko, A., Kaartinen, H., Jaakkola, A., Khoramshahi, E., Hakala, T., Hyypä, J., Holopainen, M., Hyypä, H., 2015. SLAM-aided stem mapping for forest inventory with small-footprint mobile LiDAR. *Forests* 6, 4588–4606.
- Tang, L., Shao, G., 2015. Drone remote sensing for forestry research and practices. *Journal of Forestry Research* 26, 791–797. <https://doi.org/10.1007/s11676-015-0088-y>
- Tao, W., Lei, Y., Mooney, P., 2011. Dense point cloud extraction from UAV captured images in forest area, in: *Proceedings 2011 IEEE International Conference on Spatial Data Mining and Geographical Knowledge Services*. IEEE, pp. 389–392.
- Ter-Mikaelian, M.T., Parker, W.C., 2000. Estimating biomass of white spruce seedlings with vertical photo imagery. *New Forests* 20, 145–162.
- Thies \*, M., Pfeifer, N., Winterhalder, D., Gorte, B.G.H., 2004. Three-dimensional reconstruction of stems for assessment of taper, sweep and lean based on laser scanning of standing trees. *Scandinavian Journal of Forest Research* 19, 571–581. <https://doi.org/10.1080/02827580410019562>
- Thies, M., Pfeifer, N., Winterhalder, D., Gorte, B.G.H., 2004. Three-dimensional reconstruction of stems for assessment of taper, sweep and lean based on laser scanning of standing trees. *Scandinavian Journal of Forest Research* 19, 571–581. <https://doi.org/10.1080/02827580410019562>

- Tomasi, C., Kanade, T., 1992. Shape and motion from image streams under orthography: a factorization method. *International journal of computer vision* 9, 137–154.
- Torresan, C., Berton, A., Carotenuto, F., Di Gennaro, S.F., Gioli, B., Matese, A., Miglietta, F., Vagnoli, C., Zaldei, A., Wallace, L., 2017. Forestry applications of UAVs in Europe: a review. *International Journal of Remote Sensing* 38, 2427–2447. <https://doi.org/10.1080/01431161.2016.1252477>
- Tu, Y.-H., Phinn, S., Johansen, K., Robson, A., 2018. Assessing Radiometric Correction Approaches for Multi-Spectral UAS Imagery for Horticultural Applications. *Remote Sensing* 10, 1684. <https://doi.org/10.3390/rs10111684>
- Turner, D., Lucieer, A., Wallace, L., 2014. Direct georeferencing of ultrahigh-resolution UAV imagery. *IEEE Transactions on Geoscience and Remote Sensing* 52, 2738–2745.
- Turner, D., Lucieer, A., Wallace, L., 2013. Direct georeferencing of ultrahigh-resolution UAV imagery. *IEEE Transactions on Geoscience and Remote Sensing* 52, 2738–2745.
- Valladares, F., Sánchez-Gómez, D., 2006. Ecophysiological Traits Associated with Drought in Mediterranean Tree Seedlings: Individual Responses versus Interspecific Trends in Eleven Species. *Plant Biology* 8, 688–697. <https://doi.org/10.1055/s-2006-924107>
- Van de Peer, T., Mereu, S., Verheyen, K., Saura, J.M.C., Morillas, L., Roales, J., Cascio, M.L., Spano, D., Paquette, A., Muys, B., 2018. Tree seedling vitality improves with functional diversity in a Mediterranean common garden experiment. *Forest ecology and management* 409, 614–633.
- Verma, A.K., Bourke, M.C., 2019. A method based on structure-from-motion photogrammetry to generate sub-millimetre-resolution digital elevation models for investigating rock breakdown features. *Earth Surface Dynamics* 7, 45–66.
- Wallace, L., Lucieer, A., Malenovský, Z., Turner, D., Vopěnka, P., 2016. Assessment of forest structure using two UAV techniques: A comparison of airborne laser scanning and structure from motion (SfM) point clouds. *Forests* 7, 1–16. <https://doi.org/10.3390/f7030062>
- Wallace, L., Lucieer, A., Watson, C., Turner, D., 2012. Development of a UAV-LiDAR system with application to forest inventory. *Remote Sensing* 4, 1519–1543.
- Wallace, L.O., Lucieer, A., Watson, C.S., 2012. Assessing the feasibility of UAV-based LiDAR for high resolution forest change detection, in: *The 12th Congress of the International Society for Photogrammetry and Remote Sensing*. pp. 499–504.
- Wang, L., Gong, P., Biging, G.S., 2004. Individual tree-crown delineation and treetop detection in high-spatial-resolution aerial imagery. *Photogrammetric Engineering & Remote Sensing* 70, 351–357.
- Wei, T., Simko, V., 2015. corrplot: Visualization of a correlation matrix. 2013. URL <https://CRAN.R-project.org/package=corrplot>. R package version 0.77.
- Wensel, L., Olson, C., 1995a. Tree Taper Model Volume Equations: II. Tree Taper Models for Major Commercial California Conifers. *Hilgardia* 62, 1–16.
- Wensel, L., Olson, C., 1995b. Tree Taper Model Volume Equations: IV. Tree Volume Equations for Major California Conifers. *Hilgardia* 62, 1–73.
- Westoby, Matthew J., Brasington, J., Glasser, N.F., Hambrey, M.J., Reynolds, J.M., 2012. ‘Structure-from-Motion’ photogrammetry: A low-cost, effective tool for geoscience applications. *Geomorphology* 179, 300–314.
- Westoby, M.J., Brasington, J., Glasser, N.F., Hambrey, M.J., Reynolds, J.M., 2012. ‘Structure-from-Motion’ photogrammetry: A low-cost, effective tool for geoscience applications. *Geomorphology* 179, 300–314. <https://doi.org/10.1016/j.geomorph.2012.08.021>
- White, T.L., Adams, W.T., Neale, D.B., 2007. *Forest genetics*. Cabi.
- Whiteside, T.G., Bartolo, R.E., 2016. Robust and repeatable ruleset development for hierarchical object-based monitoring of revegetation using high spatial and temporal resolution UAS data, in: *GEOBIA 2016 : Solutions and Synergies*. Presented at the *GEOBIA 2016 : Solutions and Synergies*, University of Twente Faculty of Geo-Information and Earth Observation (ITC), University of Twente Faculty of Geo-Information and Earth Observation (ITC). <https://doi.org/10.3990/2.425>

- Wickham, H., 2016. *ggplot2: elegant graphics for data analysis*. Springer.
- Williams, A.P., Allen, C.D., Macalady, A.K., Griffin, D., Woodhouse, C.A., Meko, D.M., Swetnam, T.W., Rauscher, S.A., Seager, R., Grissino-Mayer, H.D., 2013. Temperature as a potent driver of regional forest drought stress and tree mortality. *Nature Climate Change* 3, 292.
- Williamson, R.L., 1975. Out-of-roundness in Douglas-fir stems. *Forest Science* 21, 365–370.
- Wilson, B.F., Archer, R.R., 1977. Reaction Wood: Induction and Mechanical Action. *Annu. Rev. Plant. Physiol.* 28, 23–43. <https://doi.org/10.1146/annurev.pp.28.060177.000323>
- Wing, M.G., Burnett, J., Johnson, S., Akay, A.E., Sessions, J., 2014. A Low-cost unmanned aerial system for remote sensing of forested landscapes. *International Journal of Remote Sensing Applications* 4, 113–120.
- Zaforemska, A., Xiao, W., Gaulton, R., 2019. Individual tree detection from UAV Lidar data in a mixed species woodland. *ISPRS Geospatial Week 2019*.
- Zhang, C., Zhou, Y., Qiu, F., 2015. Individual tree segmentation from LiDAR point clouds for urban forest inventory. *Remote Sensing* 7, 7892–7913.
- Zhang, K., Chen, S.-C., Whitman, D., Shyu, M.-L., Yan, J., Zhang, C., 2003. A progressive morphological filter for removing nonground measurements from airborne LIDAR data. *IEEE transactions on geoscience and remote sensing* 41, 872–882.
- Zhang, W., Qi, J., Wan, P., Wang, H., Xie, D., Wang, X., Yan, G., 2016. An easy-to-use airborne LiDAR data filtering method based on cloth simulation. *Remote Sensing* 8, 501.
- Ziegler, M., Konrad, H., Hofrichter, J., Wimmer, A., Ruppert, G.S., Schardt, M., Hyypäe, J.M., 2000. Assessment of forest attributes and single-tree segmentation by means of laser scanning, in: *Laser Radar Technology and Applications V*. International Society for Optics and Photonics, pp. 73–84.